GFZ
Helmholtz Centre
POTSDAM

GeoMod 2014

Modelling in Geosciences

Programme & Extended Abstracts

31 August - 5 September 2014

Editors:
Kirsten Elger
Øystein Thordén Haug
Malte Ritter

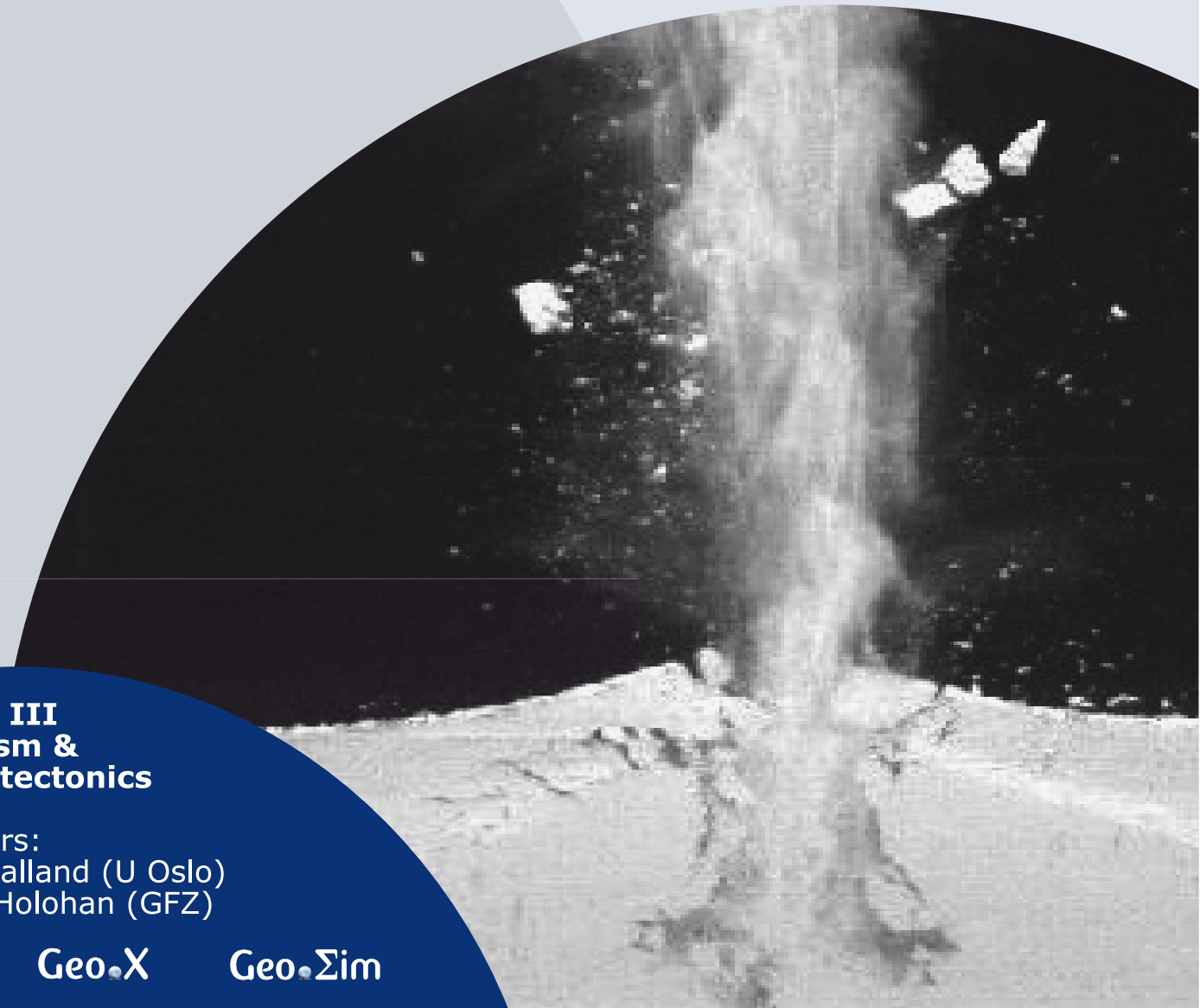

Session III
Volcanism & volcanotectonics

Conveners:
Olivier Galland (U Oslo)
Eoghan Holohan (GFZ)

DFG GeoX GeoSim

Recommended Citation

Elger, K; Haug, Ø. T.; Ritter, M. C. (Eds), (2014): Proceedings of GeoMod2014 – Modelling in Geosciences: Programme and Extended Abstracts 31 August–5 September 2014, GeoMod2014 – Modelling in Geosciences (Potsdam 2014), Potsdam: GFZ German Research Centre for Geosciences. DOI: http://doi.org/10.2312/GFZ.geomod.2014.001.

Disclaimer and Copyright

Imprint

Publisher
Helmholtz Centre Potsdam
GFZ German Research Centre for Geosciences
Telegrafenberg
14473 Potsdam
Published in Potsdam, Germany

Editors
Kirsten Elger
Øystein T. Haug
Malte C. Ritter

doi: 10.2312/GFZ.geomod.2014.001

About this book

This volume contains the extended abstracts of contributions presented during GeoMod 2014 at the Helmholtz Centre Potsdam GFZ German Research Centre for Geosciences (GFZ Potsdam), showing the state of the art of the tectonic modeling community.

GeoMod is a biennial conference dedicated to latest results of analogue and numerical modelling of lithospheric and mantle deformation. It started in 2002 in Milan as RealMod2002, then moved to Lucerne (GeoMod2004), Florence (2008), Lisbon (2010), and Lausanne (2012).

GeoMod2014 took place from 31 August to 3 September 2014 with 138 participants from 25 countries on all continents. The scientific programme of GeoMod2014 was organized in seven topical sessions listed below. The conference was followed by a 2-day short course on "Constitutive Laws: from Observation to Implementation in Models" (including lectures, lab visits, and practical exercises), as well as a 1-day hands-on tutorial on the ASPECT numerical modelling software.

GeoMod2014 focused on rheology and deformation at a wide range of temporal and spatial scales: from earthquakes to long-term deformation, from microstructures to orogens and subduction systems. For the first time, the discipline of volcanotectonics was included, while the (mantle) geodynamics community was more strongly represented than in previous editions. The bridge to field geology has traditionally been strong. At GeoMod 2014, fitting to the focus on rheology, the rock mechanics community was also represented. We thank our sponsors DFG, GFZ Potsdam and Geo.X, the conveners and all participants for contributing to a successful conference.

The GeoMod2014 Committee

The Scientific Committee
Onno Oncken
Georg Dresen
Stephan Sobolev
Matthias Rosenau
Karen Leever

The Organising Committee
Kirsten Elger
Franziska Alberg
Students support: Zahra Amirzada, Felix Eckelmann, Øystein Thordén Haug, Shaoyang Li, Malte Ritter, Tasca Santimano, Sarah Schröder, Johannes Wagner

Sessions, Conveners, and keynote speakers

(Seismo-)tectonics
Conveners: Boris Kaus (U Mainz), Onno Oncken (GFZ/FU Berlin),
Keynotes: Kelin Wang (Geological Survey Canada, Alberta), Bertrand Maillot (U Cergy-Pontoise)

Tectonics & Surface Processes
Conveners: Fabien Graveleau (U Lille), Niels Hovius (GFZ/U Potsdam),
Keynotes: Ritske Huismans (U Bergen), Stéphane Dominguez (U Montpellier II)

Volcanism and Volcanotectonics
Conveners: Olivier Galland (U Oslo), Eoghan Holohan (GFZ)
Keynotes: Rikke Pedersen (U Iceland), Olivier Roche (U BP Clermont-Ferrand)

Geodynamics
Conveners: Francesca Funiciello (U Roma Tre), Stephan Sobolev (GFZ),
Keynotes: Anne Davaille (U Paris-Sud), Bernhard Steinberger (GFZ)

Rheology
Conveners: Georg Dresen (GFZ/U Potsdam), Hiroki Sone (GFZ),
Keynotes: Yuri Fialko (U California), Laurent Montési (U Maryland)

Fluids and Deformation
Conveners: Stephen Miller (U Bonn), Marcos Moreno Switt (GFZ),
Keynotes: Boris Galvan (U Bonn), Takeshi Tsuji (U Kyushu)

Methods and Materials (poster-only session)
Conveners: Matthias Rosenau (GFZ), Marcel Frehner (ETH Zürich)

Short course on "Constitutive Laws: from Observation to Implementation in Models"
Lecturers: Onno Oncken (GFZ Potsdam), Matthias Rosenau (GFZ Potsdam), Fabio Corbi (GFZ Potsdam), Georg Dresen (GFZ Potsdam), Stephan Sobolev (GFZ Potsdam), Sascha Brune (U Sydney)

Hands-on tutorial on "ASPECT: a next-generation geodynamic modelling software"
(Advanced Solver for Problems in Earth's ConvecTion)
Lecturers: Anne Glerum (Utrecht University), Juliane Dannberg (GFZ Potsdam). Supervised by Wolfgang Bangerth (Texas A&M University, ASPECT main developer), Stephan Sobolev (GFZ Potsdam), Bernhard Steinberger (GFZ Potsdam).

Contents

I. (Seismo-)tectonics **1**

An investigation of seismicity and lithospheric features of the Zagros region, SW Iran, using coda wave attenuation
M. I. Ahmadzadeh, H. Rahimi, F. Sobouti **3**

Coseismic Coulomb stress changes on intra-continental normal and thrust faults: insights from three-dimensional finite-element modelling
M. Bagge, A. Hampel **7**

The role of pre-existing frictional weaknesses on the propagation of extensional fault
L. Bonini, R. Basili, P. Burrato, V. Kastelic, G. Toscani, S. Seno, G. Valensise **9**

Analogue models of subduction megathrust earthquakes: analyzing the viscoelastic rheological parameter space with an innovative monitoring technique
S. Brizzi, F. Corbi, F. Funiciello, M. Moroni **14**

Upscaling of micro- and meso-scale structures to local- and regional scales: implications for 3D implicit and explicit models of structurally complex deformation of multi-layered rocks
M. Egglseder, A. Cruden **17**

Influence of the seismogenic downdip width on supercycles at subduction thrusts
R. Herrendörfer, Y. van Dinther, T. Gerya, L. A. Dalguer **22**

Geomechanical modeling of fault geometry role on subduction earthquake cycle: Case study of Chilean margin
S. Li, M. Moreno, J. Bedford, M. Rosenau, D. Melnick, O. Oncken **26**

The long term evolution of fold-and-thrust belts: consistency of numerical approaches and physical experiments
B. Maillot **29**

Cross-scale model of seismic cycle: first results
I. A. Muldashev, S. V. Sobolev **33**

Numerical modelling of the instantaneous subduction dynamics of the Banda Arc region
C. Pranger, C. Thieulot, A. van den Berg, W. Spakman **36**

Towards 3D seismo-thermo-mechanical models of the subduction thrust
C. Pranger, Y. van Dinther, T. Gerya, F. Corbi, F. Funiciello **37**

Smart or Beautiful? Accretionary wedge evolution seen as a competition between minimum work and critical taper
T. Santimano, M. Rosenau, O. Oncken **39**

CHANDRAYAAN-1 data infers tectonic activity on the south pole of the moon
P. Singh, S. Mukherjee **43**

The concepts of complex network advance understanding of earthquake science
N. Suzuki **46**

Hypothesis of geodynamic processes in the lithosphere under catastrophic earthquake Tohoku-Oki
V. N. Tatarinov, A. I. Kagan, T. A. Tatarinova **49**

Seismo-thermo-mechanical modeling of subduction zone seismicity
Y. van Dinther, T. Gerya, L. A. Dalguer, P. M. Mai **52**

Thermal Expressions of Stick-slip and Creeping Subduction Megathrusts
K. Wang, X. Gao **56**

II. Tectonics and Surface Processes **60**

Neotectonic evolution of the El Salvador Fault Zone. Insights from 4D analogue experiments.
J. Alonso-Henar, G. Schreurs, J.J. Martínez-Díaz, J.A. Álvarez-Gómez **62**

Restraining and releasing bands along a sinistral strike-slip shear zone: A physical modeling approach
A. Blanco, F. C. Alves da Silva **67**

Numerical basin modelling of a salt rim syncline: insights into rim syncline evolution and salt diapirism
C. Brandes, J. Winsemann **71**

Modelling Syntectonic Sedimentation in a Extensional Faults System
A. Carmona, R. Clavera-Gispert, O. Gratacós, S. Hardy, J. A. M. de la Fuente **75**

Process-Based Forward Numerical Modelling SIMSAFADIM-CLASTIC: The Vilomara Composite Sequence case (Eocene, Ebro basin, NE Iberian Peninsula).
R. Clavera-Gispert, O. Gratacós, M. López-Blanco, R. Tolosana-Delgado **80**

The balance between uplift and fluvial erosion over a single seismic cycle – an example from Taiwan
K. Cook, F. Graveleau, J. Turowski, N. Hovius. J. Suppe **84**

Joint analog modeling of marine and terrestial geological processes: state of the art and new developments
S. Dominguez **85**

Fold growth rates in 3D buckle folds
M.Frehner **89**

Furrow-and-ridge morphology on rockglaciers explained by gravity-driven buckle folding: A case study from the Murtèl rockglacier (Switzerland)
M. Frehner, I. Gärtner-Roer, A. H. M. Ling **95**

Structural evolution and structural style of South Eastern Kohat deciphered through 3D geoseismic model using MOVE software, Shakardarra area, KP Pakistan
H. Ghani, H. Hussain, M. Zafar, I. Khan, A. Malik, M. Abid, E. Javed **101**

Lithospheric scale analogue models of the southern Gulf of California oblique rift
D. Gracia-Marroquín, R. Portillo-Pineda, M. Cerca, G. Corti **108**

The negative inversion of thrust faults and related basin geometries: insight from analogue modelling experiments
F. Graveleau, O. Averbuch, B. Vendeville, A. Quinion, M. Ouzgaït **112**

Experimental modelling of deformation-erosion-sedimentation interactions in compressional, extensional and strike-slip settings
F. Graveleau, V. Strak, S. Dominguez, J. Malavieille, M. Chatton, I. Manighetti, C. Petit **114**

Linking lithosphere deformation and sedimentary basin formation over multiple scales
R. S. Huismans **116**

3D Analogue Modelling of the Effect of Fan Sedimentation on Accretionary Wedge Dynamics – the Magdalena Fan case, South Caribbean Margin, Colombia
K. Leever, E. Johansen **117**

From continental rifting to seafloor spreading: Insight from 3D thermo-mechanical modeling
J. Liao, T. Gerya **121**

Dynamic Modelling of Accretionary Prisms and Stratigraphy of Forearc basins
U. Mannu, K. Ueda, S. D. Willett, T. Gerya, M. Strasser **131**

Evolution of topography of post-Devonian Scandinavia: Effects and rates of erosion
S. Medvedev, E. H. Hartz **136**

Numerical modeling of main inverted structures in the Western Barents Sea.
M. A. F. Miraj, C. Pascal, R. H. Gabrielsen, J. I. Faleide **140**

Exploratory analog modeling of the effects of a morpho-rheological obstacle across a wrench fault system: the example of the Gloria Fault – Tore Madeira Rise intersection in NE Atlantic
F. M. Rosas, J. Almeida, F. Barata, B. Carvalho, P. Terrinha, J. Duarte, C. Kullberg, R. Tomás **144**

DANSER: an open source surface evolution code beyond coupling with tectonic models
S. Schroeder, R. Gloaguen, J. Tympel, A. Babeyko, S. V. Sobolev **149**

Kinematic reconstruction of the hastings block, southern New England Orogen, Australia
J. Yan, P. Lennox, B. F. J. Kelly, R. Offler **153**

Stability of over-pressured cohesive and frictional materials based on Sequential Limit Analysis
X. Yuan, Y. M. Leroy, B. Maillot, Y. Guéguen **159**

4D Transfer Zone Modeling in Continental Rifts
F. Zwaan, G. Schreurs **164**

III. Volcanism and Volcanotectonics **170**

Solidification effects on sill formation: an experimental approach
L. Chanceaux, T. Menand **172**

The origin of circumferential fissures: insights from analog models
F. Corbi, E. Rivalta, V. Pinel, F. Maccaferri, V. Acocella **177**

Megatsunami generation from caldera subsidence
B. Kennedy, M. Gallagher, C. Gomez, T. Davies **178**

Toward a unified dynamic model for dikes and cone sheets in volcanic systems
O. Galland, S. Burchardt, E. Hallot, R. Mourgues, C. Bulois **181**

Morphology and dynamics of explosive vents through cohesive rock formations
O. Galland, G. Gisler, Ø. T. Haug **185**

Temporal changes in mantle wedge geometry and magma generation processes in the Central Andes: towards linking petrological data to thermomechanical models
R. Heistek, M. Brandmeier, H. Freymuth, G. Wörner **188**

Use of the Distinct Element Method in Volcano-tectonic Modeling
E. P. Holohan, H. Sudhaus, M. P. J. Schöpfer, T. R. Walter, J. J. Walsh **191**

Three-Dimensional Analysis of dike/fault interaction at Mono Basin (California) using the Finite Element Method
D. La Marra, M. Battaglia **196**

Modeling of Cooling History for the Jurassic Composite Granitic Plutons in the Central Nanling Region, South China: Implications for the Mineralization Process and Tectonic Evolution
H. Li, K. Watanabe, K. Yonezu **201**

The gravitational unloading due to rift depression: A mechanism for the formation of off-rift volcanoes in (continental) rift zones
F. Maccaferri, E. Rivalta, D. Keir, V. Acocella **206**

The formation of terrace-bounding faults on Olympus Mons volcano, Mars
S. Musiol, B. Cailleau, E. P. Holohan, T .R. Walter, D. A. Williams, A. Dumke, S. van Gasselt **211**

Surface deformation simulations of volcanic and tectonic processes in Iceland
R. Pedersen **214**

Overburden bulking in analogue models of depletion-induced collapse quantified with computed X-ray micro-tomography
S. Poppe, E. P. Holohan, , E. Pauwels, V. Cnudde, M. Kervyn **217**

Mechanisms of entrainment of a granular substrate by pyroclastic density currents: insights from laboratory experiments and models, and implications for flow dynamics.
O. Roche, Y. Niño **221**

Influence of crust type on the long-term deformation of a volcano: example from Mt. Etna (Italy)
S. Scudero, G. De Guidi, S. Imposa, M. Palano **226**

Analogue and numerical modeling of rifting events. Complementary tools to understand the rifting process.
D. Trippanera, D. Lamarra, V. Acocella, J. Ruch, E. Rivalta **231**

IV. Geodynamics **233**

Anomalous structure of the oceanic lithosphere in the North Atlantic and Arctic oceans: preliminary analysis based on bathymetry, gravity and crustal structure
O. Barantseva, I. M. Artemieva, H. Thybo, M. Herceg **235**

Constraining the rheology of the lithosphere through geodynamic inverse modelling
T. Baumann, B. Kaus, A. Popov **237**

A new model for the architecture of magma-poor rifted margins
S. Brune, C. Heine, M. Pérez-Gussinyé, S. V. Sobolev **239**

Oblique extensional structures from initial deformation to breakup: Insights from numerical 3D lithospheric-scale experiments
S. Brune **242**

Initial models of the influence of collision-phase inheritance on continental rifting
S. Buiter, J. Tetreault, R. Ghazian **246**

Modelling subsidence history of rift-type basins
M. Cacace, M. Scheck-Wenderoth **247**

Strain localization during compression of a laterally heterogeneous lithosphere
E. Calignano, D. Sokoutis, E. Willingshofer **249**

3-D numerical modeling of subduction evolution of the western Mediterranean region
M. V. Chertova, W. Spakman, A. P. van den Berg, T. Geenen, D. J. J. van Hinsbergen **254**

Surface manifestations of low-buoyancy mantle plumes: Insights from geodynamic modeling
J. Dannberg, S. V. Sobolev **259**

Plumes to plate tectonics: insights from laboratory experiments
A. Davaille **261**

Three dimensional laboratory models of subduction: plate interface, overriding plate deformation and energy dissipation
J. C. Duarte, Z. Chen, W. P. Schellart, A. R. Cruden **266**

Geometrical transitions of mantle plumes: an insight from numerical simulations
U. Dutta, S. Sarkar, N. Mandal **269**

Thermo-mechanically coupled subduction with a free surface using ASPECT
M. Fraters, A. Glerum, C. Thieulot, W. Spakman **272**

The Role of the Initial Condition in Numerical Models of the Present-day Mantle Flow Field
E. H. Fritzell, A. L. Aller, G. E. Shephard **275**

3-D computational modeling of the continental plate collision near South Island, New Zealand
L. Karatun, C. Thieulot, R. Pysklywec **276**

Featuring lithosphere rheology in models of glacial isostatic adjustment
V. Klemann, M. Tesauro, Z. Martinec, I. Sasgen **278**

The 3D density and temperature distribution in an intracratonic basin setting: The Barents Sea and Kara Sea region
P. Klitzke, J. I. Faleide, J. Sippel, M. Scheck-Wenderoth **281**

The effect of melting and crustal production on plate tectonics on terrestrial planets
D. L. Lourenço, P. J. Tackley **284**

3-D numerical modelling of subduction initiation at curved passive margins
F. O. Marques, F. R. Cabral, T. V. Gerya, G. Zhu, D. A. May **285**

Crustal deformation and magmatism at the transition between subduction and collisional domains: insight from 3D numerical modeling
A. Menant, P. Sternai, L. Jolivet, L. Guillou-Frottier, T. Gerya **289**

Segregation, Accumulation, and Entrainment of the Oceanic Crust in the Lowermost Mantle: Exploring the Range of Governing Parameters with Numerical Modelling
E. Mulyukova, B. Steinberger, M. Dabrowski, S. V. Sobolev **294**

Role of extensional strain-rate on lithosphere necking architecture during continental rifting
Y. Nestola, F. Storti, C. Cavozzi **298**

Toroidal, counter-toroidal, and poloidal flows of the Rivera and Cocos plates
F. Neumann, A Vazquez, G Tolson, J. Contreras **299**

Estimating Crustal Thickness of Iran Using Euler Deconvolution Method and EIGEN-GL04C Geopotential Model
S. Parang **300**

How do weak plate boundaries affect the dynamic topography and geoid?
A. G. Petrunin, M. K. Kaban, B. Steinberger, H. Schmeling **304**

The development of topographic plateaus in an India-Asia-like collision zone using 3D numerical simulations
A. E. Pusok, B. Kaus, A. Popov **308**

Towards quantification of the interplay between strain weakening and strain localisation using analogue models
M. C. Ritter, M. Rosenau, K. Leever, O. Oncken **310**

Modelling plate kinematics, slabs and LLSVP dynamics – an example from the Arctic and northern Panthalassa
G. E. Shephard, A. L. Bull, C. Gaina **313**

Strike-slip movements and Rotation of tectonic blocks in the Kaboodan area, south Khur, Central Iran
A. Sohrabi, A. Nadimi **318**

On the relation between plate tectonics, large-scale mantle flow and mantle plumes: Some recent results and many open questions
B. Steinberger, R. Gassmoeller, E. Mulyukova, J. Dannberg, S. V. Sobolev **320**

The role of crustal thickness and lithospheric rheology on rifted margins width and tectonic subsidence
A. E. Svartman Dias, L. L. Lavier, N. W. Hayman **324**

Influence of Melting on the Long-Term Thermo-Chemical Evolution of Earth's Deep Mantle
P. J. Tackley, D. Lourenço, I. Fomin, T. Nakagawa **329**

A two- and three-dimensional numerical modelling benchmark of slab detachment
C. Thieulot, A. Glerum, B. Hillebrand, S. Schmalholz, W. Spakman, T. Torsvik **331**

The effect of strong heterogeneities in the upper mantle rheology on the dynamic topography and geoid
A. O. Tutu **332**

The role of weak seeds in numerical modelling of continental extensional systems
I. van Zelst, C. Thieulot, S. J. H. Buiter, J. Naliboff, W. Spakman **334**

The up side down logic of orogenic collision: on the formation of low-topography mountain ranges
K. Vogt, L. Matenco, T. Geyra, S. Gloetingh **336**

Implementing fluid flow in SLIM-3D
M. Walter, J. Quinteros, S. V. Sobolev **340**

The mechanical erosion of refertilized continental lithosphere by plume driven mantle flow
H. Wang, J. van Hunen, D. G. Pearson **342**

Deformation of forearcs during ridge subduction
S. Zeumann, A. Hampel **347**

V. Rheology 350

Fold Geometry Toolbox 2: A New Tool to Estimate Mechanical Parameters and Shortening from Fold Geometry
M. Adamuszek, M. Dabrowski, D. W. Schmid **352**

Mechanical anisotropy development and localization in two-phase composite rocks.
M. Dabrowski **355**

Numerical models of ductile roots of mature strike-slip faults
Y. Fialko **358**

Present-day intra-plate deformation of the Eurasian plate
C. Garcia-Sancho, R. Gover, K. N. Warners-Ruckstuhl, M. Tesauro **363**

Localization of deformation in a polymineralic material
S. Jammes, L. L. Lavier, J. E. Reber **365**

Localization processes on Earth, Mars, and Venus
L. G. J. Montési, F. Gueydan **368**

Rheology of bubble- and crystal-bearing magma: new analogue experimental data and an effective-medium model
S. P. Mueller, J. M. Truby, E. W. Llewellin, H. M. Mader **372**

Modeling stress evolution around a rising salt diapir
M. A. Nikolinakou, P. B. Flemings, M. R. Hudec **376**

Numerical bifurcation analysis of spontaneous strain localization resulting in necking of a layer
M. Peters, T. Poulet, M. Veveakis, A. Karrech, M. Herwegh, K. Regenauer-Lieb **381**

Finite element model investigation of fault shear stress accumulation due to elastic loading and viscous relaxation.
H. Sone **385**

Lithospheric strength and elastic thickness variations in the North American continent
M. Tesauro, M. K. Kaban, S. Cloetingh, W. D. Mooney **387**

VI. Fluids and Deformation **391**

Effect of Fluid Circulation on Intermediate-Depths Subduction Dynamics: From Field Observations to Numerical Modelling
S. Angiboust, S. Wolf, E. Burov, P. Agard, P. Yamato **393**

Assessment of microbial contamination of groundwater near solid waste dumpsites in basement complex formation, using total plate count method
B. S. Badmus **395**

Physico-chemical properties of soil samples and environmental impact of dumpsite on groundwater quality in basement complex terrain, south western Nigeria
B. S. Badmus **396**

Towards a general simulation tool for complex fluid-rock lithospheric processes: merging pre-processing, processing and post-processing in state-of-the-art computational devices
B. Galvan, S. Hamidi, T. Heinze, M. Khatami, G. Jansen, S. Miller **397**

THC modelling of an Enhanced Geothermal System
S. Hamidi, T. Heinze, B. Galvan, S. Miller, **401**

Numerical Modelling of earthquake swarms in the Vogtland / West-Bohemia
T. Heinze, S. Hamidi, B. Galvan, S. Miller **404**

Modelling of fractured reservoirs: fluid-rock interactions within fault domains
A. Jacquey, M. Cacace, G. Blöcher, M. Scheck-Wenderoth **407**

Heat transport mechanisms at different scales – a 3D modelling workflow
M. Scheck-Wenderoth, M. Cacace, J. Sippel, Y. Petrovich Maystrenko, Y. Cherubini, V. Noack, B. Onno Kaiser, B. Lewerenz **412**

Digital rock physics: Insight into fluid flow and elastic deformation of porous media
T. Tsuji **417**

VII. Methods and Materials **422**

Seismological monitoring of labscale landslides: Method & bouncing ball benchmark
Z. Amirzada, Ø. T. Haug, A. Burtin, T. Eken, M. Rosenau **424**

Small-scale modelling of ice flow perturbations induced by sudden ice shelf breakup
G. Corti, A. Zeoli, I. Iandelli **428**

Carbopol® for experimental tectonics: a rheological benchmark study
E. Di Giuseppe, F. Corbi, F. Funiciello, A. Massmeyer, T.N. Santimano **430**

Initiation process of the frontal thrust revealed from detailed analogue experiments
T. Dotare, Y. Yamada, T. Hori, H. Sakaguchi **434**

The Use of Scaling Theory in Geological Laboratory Models
O. Galland, E. Holohan, G. Dumazer **439**

Testing tools for the generation of an unstructured tetrahedral grid on a realistic 3D underground model
I. Görz, F. Träger, B. Zehner, J. Pellerin **443**

Flanking structures – New insights from analogue models
C. J. S. Gomes, B. A. Rodrigues, I. Endo **448**

The Ribbon Tool
J. Großmann, J. F. Ellis, H. Broichhausen **452**

A new method to study the energy budget of rock fragmentation
Ø. T. Haug, M. Rosenau, Z. Amirzada, K. Leever, O. Oncken **457**

Fringes projection for 3D displacement analysis of experimental dry granular avalanches
C. Mares, B. Barrientos-García, M. Cerca, D. Sarocchi, L. A. R. Sedano **459**

A 3-D Lagrangian finite element algorithm with contour-based re-meshing for simulating large-strain hydrodynamic instabilities in visco-elastic fluids
M. von Tscharner, S. Schmalholz **464**

Some Remarks on wet gypsum as a viscous material for physical modeling
A. Yassaghi **467**

Scientific Programme **471**

Short Course Programme **475**

Session III.

Volcanism and Volcanotectonics

Session Description: Volcanism and Volcanotectonics

Conveners: Olivier Galland (U Oslo), Eoghan Holohan (GFZ)

Volcanic plumbing systems evolve through the interaction of numerous processes governing the ascent, emplacement, and eruption of magma. A full physical understanding of sub-volcanic and volcanic processes faces stimulating challenges. For instance (1) magma transport through the Earth's crust is not only governed by the mechanical behaviour of the magma or of the host rock, but also by the complex interplay between them. In addition, (2) magma eruption is governed by the complex rheology of the magma and multiphase flows involving gas, liquid and solid phases, with sometimes moving conduit walls. Advanced and quantitative experimental, numerical, and theoretical modelling techniques are thus crucial to unravel these challenging and exciting processes. The Volcanotectonic and Volcanic Processes Session of this GeoMod 2014 international meeting aims to bring together laboratory, numerical and theoretical modellers studying the complex processes governing the mechanics of magma/ host rock systems, and volcanic eruptions.

Solidification effects on sill formation: an experimental approach

L. Chanceaux [1], T. Menand[1,2,3]

[1] *Université Blaise Pascal, Laboratoire Magmas et Volcans, F-63000 Clermont-Ferrand, France 3*
[2] *CNRS, UMR 6524, LMV, Clermont-Ferrand, France 4*
[3] *IRD, R 163, LMV, Clermont-Ferrand, France*
e-mail: *l.chanceaux@opgc.univ-bpclermont.fr*
session: *Volcanism and Volcanotectonics*

The effects of solidification on the formation of sills are studied and quantified with scaled analogue laboratory experiments. Sills represent a major mechanism for constructing continental Earth's crust because these intrusions can amalgamate and form magma reservoirs and plutons. As a result, numerous field, laboratory and numerical studies have investigated the conditions that lead to sill emplacement. However, all previous studies have neglected the potential effect magma solidification could have on sill formation.

The experiments presented here (fig. 1) involved the injection of hot vegetable oil (a magma analogue) which solidified during its propagation as a dyke in a colder and layered solid of gelatine (a host rock analogue), and were correctly scaled geometrically, kinematically, dynamically, and thermally. The gelatine solid had two layers of different stiffness, to create a priori favourable conditions to form sills (Kavanagh et al, 2006). The injection temperature T_i and the injection flux Q were systematically varied between experiments.

To analyse the experiments, we follow the experimental analysis of Taisne and Tait (2011) and define two dimensionless parameters. One describes the thermal conditions of the experiments (dimensionless temperature θ) and the other describes their dynamical conditions (dimensionless flux ϕ). The dimensionless temperature θ is defined as:

$$\frac{(T_\mathrm{s} - T_\mathrm{g})}{(T_\mathrm{i} - T_\mathrm{g})} \tag{1}$$

where T_s is the solidification temperature of vegetable oil, $T_\mathrm{s} = 31°\mathrm{C}$ (Galland et al., 2006); T_g is the gelatine temperature during the injection, typically between 5 and 7°C; T_i is the injection temperature of the vegetable oil. The dimensionless flux ϕ is defined as the ratio between the heat advected by vegetable oil and the heat lost by conduction in the gelatine. During each experiment, a feeder dyke formed first, which, provided an adequate rigidity contrast at the interface, may subsequently form a sill. The dimensionless flux ϕ was thus defined for this feeder dyke (Taisne and Tait, 2011):

$$\frac{3Q\Delta\rho g}{(2E\kappa)} \tag{2}$$

where Q is the flux of injection; $\Delta\rho$ is the difference of density between the gelatine and the vegetable oil; E is the Young's modulus of the lower layer; κ is its thermal diffusivity (assumed to be identical to that of water); and g is the gravitational acceleration.

T_s and T_g were essentially the same for all experiments so θ varied only with T_i the injection temperature. Likewise, $\Delta\rho$, g, κ were all kept constant. Consequently, ϕ varied with the injection flux Q and the Young's modulus E_{low} of the lower layer. θ and ϕ were maintained constant during an experiment (T_i, E_{low} and Q constant),

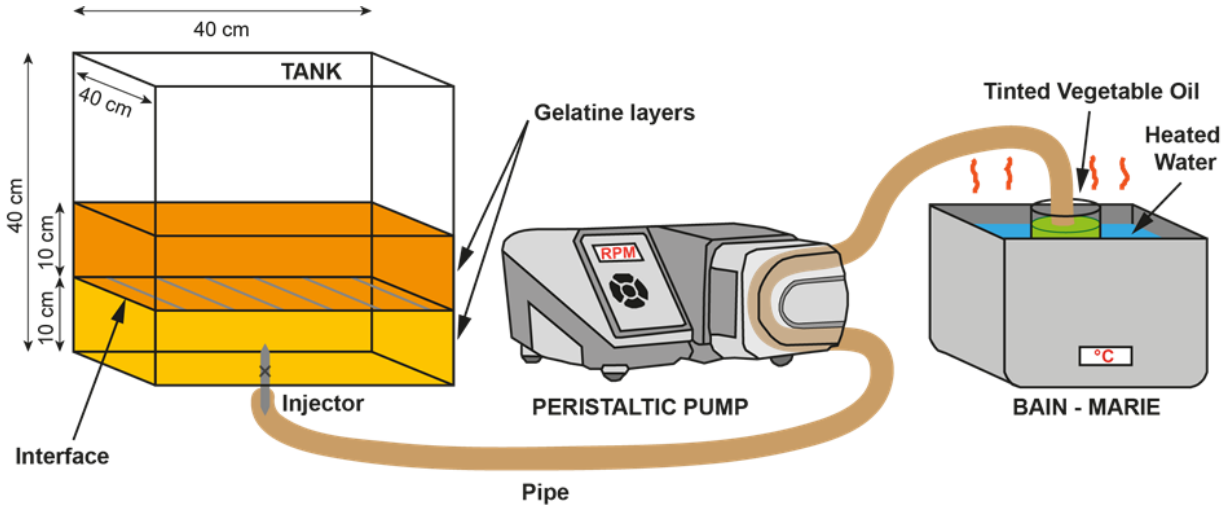

Fig. 1.: Experimental apparatus. The gelatine solid has two layers of different stiffness, to create a priori favourable conditions to form sills. Vegetable oil is heated with a bain-marie and injected at a constant rate with a peristaltic pump in the layered gelatine solid.

Tab. 1.: Behaviour of the dimensionless temperature θ and dimensionless flux ϕ.

$\theta \to 1$	$T_\mathrm{i} \to T_\mathrm{s}$	solidification operates rapidly
$\theta \to 0$	$T_\mathrm{i} \gg T_\mathrm{s}$	almost no solidification
$\phi \to 0$	low Q values	solidification operates rapidly
$\phi \gg 1$	high Q values	almost no solidification

and were varied systematically between experiments to quantify their respective influence of the formation of sills. θ varies between 0 and 1 and ϕ varies between 0 and ∞. Table 1 summarises the behaviour of θ and ϕ. The experiments were carried out under dimensionless conditions (temperature θ and flux ϕ) identical to those present in nature.

Several types of intrusions (fig. 2) were observed: dykes stopping at the interface, dykes passing through the interface and sills. These different shapes demonstrate that contrary to isothermal experiments (no temperature effect able to block sill formation), a rigidity contrast between two layers is not a sufficient condition to create a sill.

The results of the fifteen experiments performed, that is crossing dykes (low solidification effects), sills (moderate solidification effects), blocked dykes (high solidification effects), and cases when fluid could not intrude the gelatine (extreme solidification effects), are all summarized on a graph showing the dimensionless temperature θ, which describes the experimental thermal conditions, as a function of the dimensionless flux ϕ, which describes their dynamical conditions (fig. 3). Solidification effects increase as $\theta \to 1$ and $\phi \to 0$. Four areas are clearly identified:

- When the dimensionless temperature is relatively high and the dimensionless flux is very low ($\theta \approx 0.75$ to 0.95 and $\phi < 6$), there is no propagation (fig. 3, stars). Solidification effects are so important that vegetable oil freezes and solidifies in the tube and no intrusion is observed;

- When the dimensionless temperature is high and for larger dimensionless fluxes ($\theta \approx 0.7$ to 0.95 and $\phi < 15$), dykes are blocked at the interface between the two gelatine layers (fig. 3, squares). Solidification effects are important and the dyke partially solidifies

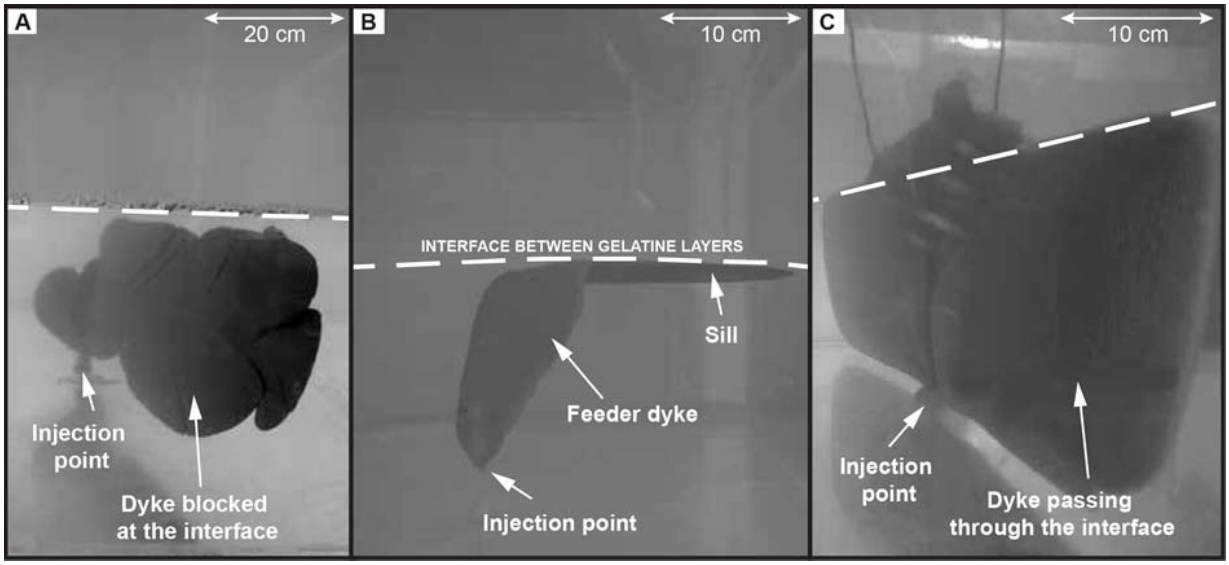

Fig. 2.: Experimental intrusions. (A) Experimental dyke blocked at the interface, three-quarter view. (B) Experimental sill, side view. (C) Experimental dyke passing through the interface, three-quarter view. The dyke takes a triangular shape above the interface.

at its walls during its propagation and development. Solidification at the upper tip of the dyke blocks its propagation, and prevent its piercing of the interface and subsequent propagation in the upper stiffer layer or its spreading along the interface as a sill;

- When the dimensionless temperature has intermediate values ($\theta \approx 0.60$ to 0.90 and $\phi < 16$), sills are created (fig. 3, disks). Solidification effects are smaller. Consequently, the feeder dyke propagates as a sill by spreading at the interface between the two layers;

- Finally, when the dimensionless temperature is low ($\theta \approx$0.6 to 0.7 and $\phi > 2$), dykes passing through the interface are created (fig. 3, triangles). Dykes do not create sills but instead pierce directly the interface to propagate in the upper layer, easily fracturing the gelatine presumably because of their high temperature: higher input of hot vegetable oil at the tip of the feeder dyke leads to lower solidification effects and presumably easier fracturation; the injection flux seemed to have less of an effect. However, solidification along the walls of the dyke seem to prevent the fluid from intruding the interface between the gelatine layers.

Thus, solidification effects restrict sill formation at an interface with a favourable rigidity contrast (upper layer stiffer than the lower one). Sill formation occurs only for a restricted and specific range of dimensionless temperatures θ and fluxes ϕ: $\theta_{\min} \leq \theta \leq \theta_{\max}$, where (c) $\theta_{\min} = 0.0039\phi + 0.61$ and (b) $\theta_{\max} = 0.019\phi + 0.68$ (fig. 3). The thermal conditions (θ) depend on injection temperature T_{i}, and dynamical conditions (ϕ) depend on injection flux Q and rigidity contrast of the intruded solid. Therefore, in our experiments, sill formation along an interface depends on three critical parameters: the injection temperature T_{i}, the injection flux Q, and the rigidity of the solid below this interface.

These experiments demonstrate that contrary to isothermal experiments where cooling could not affect sill formation, the presence of an interface that would be a priori mechanically favourable is not a sufficient condition for sill formation; solidification effects restrict sill formation. The results are consistent with field observations and provide a means to explain why some dykes form sills when others do not under seemingly similar

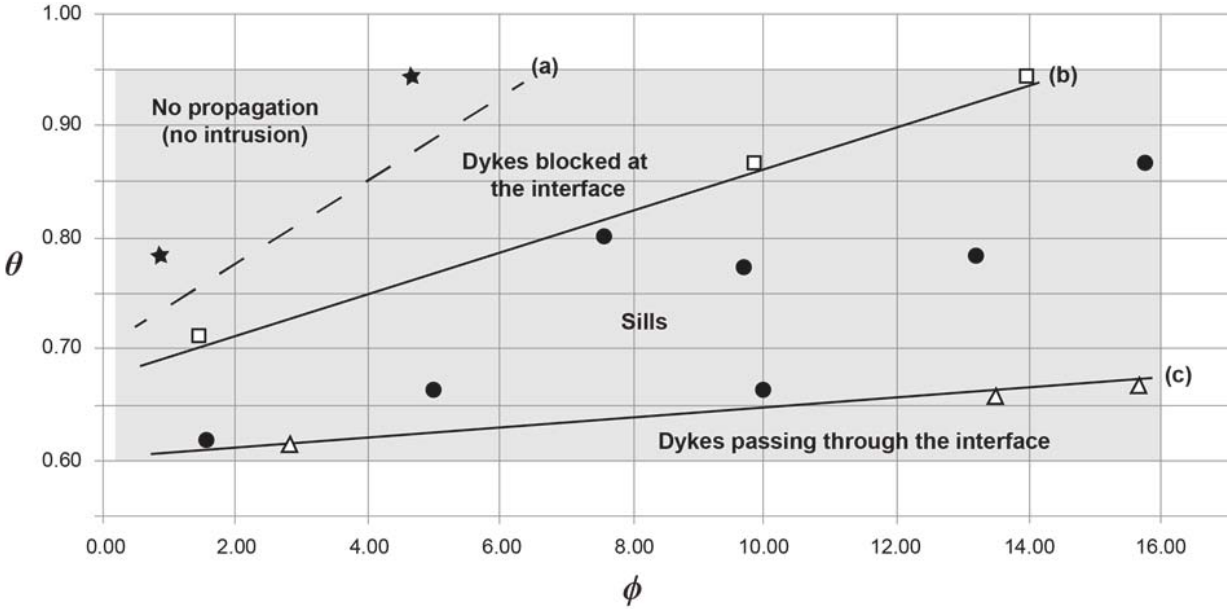

Fig. 3.: Dimensionless temperature θ as a function of dimensionless flux ϕ. Gray area shows natural ranges of values for θ and ϕ. Stars represent experiments where no propagation occurred; squares are dykes blocked at the interface; disks are sills; triangles are dykes passing through the interface. Lines (a), (b) and (c) delimit the areas for each type of intrusions. The dashed line (a) is only qualitative whereas the continuous lines (b) and (c) can be determined reliably. See text for details.

Fig. 4.: Sill with its feeder dyke in the Henry Mountains, Utah, USA, modified from Menand (2011). The view is from the East. The sill, its feeder dyke (both outlined by dashed white lines) and the intruded layered sandstone (continuous white lines) have all been rotated almost $90°$. The feeder dyke crosses several similar interfaces before spreading as a sill.

geological conditions (Fig. 4).

References

Chanceaux, L., & Menand, T. (2014). Solidification effects on sill formation: An experimental approach. Earth and Planetary Science Letters, 403, 79-88.

Galland, O., Cobbold, P. R., Hallot, E., de Bremond D'Ars, J., & Delavaud, G. (2006). Use of vegetable oil and silica powder for scale modelling of magmatic intrusion in a deforming brittle crust. Earth and Planetary Science Letters, 243(3), 786-804. doi:10.1016/j.epsl.2006.01.014

Kavanagh, J. L., Menand, T., & Sparks, R. S. J. (2006). An experimental investigation of sill formation and propagation in layered elastic media. Earth and Planetary Science Letters, 245(3), 799-813. doi:10.1016/j.epsl.2006.03.025

Menand, T. (2011). Physical controls and depth of emplacement of igneous bodies: A review. Tectonophysics, 500(1), 11-19. doi:10.1016/j.tecto.2009.10.016

Taisne, B. and Tait, S., 2011. Effect of solidification on a propagating dike. Journal of Geophysical Research 116 (B1), B01206. doi:10.1029/2009JB007058

The origin of circumferential fissures: insights from analog models

F. Corbi[1], E. Rivalta[1], V. Pinel[2], F. Maccaferri[1], V. Acocella[3]

[1] *GFZ German Centre for Geosciences, Section 2.1, Telegrafenberg, 14473 Potsdam, Germany.*
[2] *ISTerre, Université de Savoie, IRD, CNRS, Campus Scientifique, Le Bourget du Lac F73376, France.*
[3] *Dipartimento di Scienze, University 'Roma Tre', L.S.L. Murialdo, 1, 00146, Rome, Italy.*
e-mail: *fabio.corbi@gfz-potsdam.de*
session: *Volcanism and Volcanotectonics*

At caldera volcanoes eruptive fissures may align with the regional stress field, radiate along the flanks, or circumscribe the caldera [e.g., Acocella, 2007]. The circumferential fissures are often associated with ring faults and only in few cases they appear independent of the existing faults. The origin of the latter is debated [e.g., Chadwick and Dieterich 1995]. Using analog models we find that the stress perturbation due to caldera unloading affects dike dynamics and the resulting eruptive pattern. Air (magma analog) is injected within a cylindrical Plexiglas®. container filled with stiff gelatin (volcano analog) with caldera morphology. The injected air forms a buoyancy driven fracture (dike analog) that, depending on the competition between buoyancy and external forcing, steers outward. We observe analog dikes that arrest at depth, erupt in the caldera region, or in the summit plateau. The summit eruptions form arcuate fissures that develop tangentially to the volcanic edifice as circumferential fissures do in nature. Our gelatin models demonstrate that caldera unloading represents a mechanism responsible for the origin of the circumferential eruptive fissures.

References

Acocella, V. Understanding caldera structure and development: An overview of analogue models compared to natural calderas. Earth-Science Rev. 85, 125–160 (2007).

Chadwick, W. W. & Dieterich, J. H. Mechanical modeling of circumferential and radial dike intrusion on Galapagos volcanoes. J. Volcanol. Geotherm. Res. 66, 37–52 (1995).

Megatsunami generation from caldera subsidence

Max Gallagher, Ben Kennedy[1], Christopher Gomez, Tim Davies

[1] *University of Canterbury*
e-mail: *ben.kennedy@canterbury.ac.nz*
session: *Volcanism and Volcanotectonics*

Mega-tsunamis potentially have devastating global consequences. We use the term mega-tsunami to describe proximal tsunami waves greater than 100m in height. Despite extensive research into fault- and landslide-generated mega-tsunamis, and an ongoing debate about tsunamis generated by explosions and pyroclastic flows, very little is known about the potential of a subsiding caldera to generate a tsunami. Field investigations of historic medium sized caldera-forming events have identified tsunami deposits at runup heights of 10-30m, although numerical modelling has struggled to separate the causative mechanisms of submarine pyroclastic flows, landslides and caldera subsidence. Past efforts to replicate tsunamis generated by caldera subsidence have been dominantly through numerical modelling (e.g. Novikova et al., 2011). To date, only one analogue methodology has been investigated (Gray and Monaghan, 2003). Gray and Monaghan's (2003) analogue model focused on caldera subsidence, where the initial caldera floor is above sea level and the process producing waves in the modelling is most similar to a dam-break flood. As many the majority of potential tsunamis producing calderas are already partially of fully submerged, we focus our modelling on submerged calderas.

Here, we use an analogue model of a submerged subsiding piston to isolate and parameterise the caldera subsidence conditions required to generate a waves (Figure 1).

Our results show that water pours into the space created by the subsiding piston to produce a central dome of water. Waves then radially propagate away from this dome as a series of rings (Figure 1). Wave heights are measured close to the experimental caldera via video analysis of a buoy. Dimensional analysis of our analogue experiment shows that the key parameters are the velocity of subsidence (V_s), the amount of subsidence (S), water depth (D_w). We explored parameter space relevant to scaled submerged calderas. Our wave height data can thus be explained by plotting $V_s^2/\mathrm{g}D_w$ against S/D_w (Figure 2).

Some wave height variation is created in our results by the complex interaction between waves as they leave the caldera. The number and style of waves are affected by the competition between the flow rate into the subsiding caldera and the volumetric rate that space is created by the subsiding caldera and whether waves are created during or after subsidence. Each experiment creates multiple waves that radiate from the centre of the caldera at varying rates and can add and subtract affecting the wave height. Here we focus our results on the largest waves and dominant trends. These data show that larger waves are generated in shallower water and by faster subsidence rates, while the amount of subsidence becomes increasingly important at faster subsidence velocities (Figure 2). The nondimensional parameters allow us to compare our results to natural calderas. We focus our discussion on the formation of mega-tsunamis.

The results show that even large diameter calderas need to subside rapidly to generate mega-tsunamis. The following conditions are necessary for natural calderas to generate mega-tsunamis-subsidence rates $>$ 10m/s, $>$ 3km diameter calderas, $>$100 m subsidence, and water depth

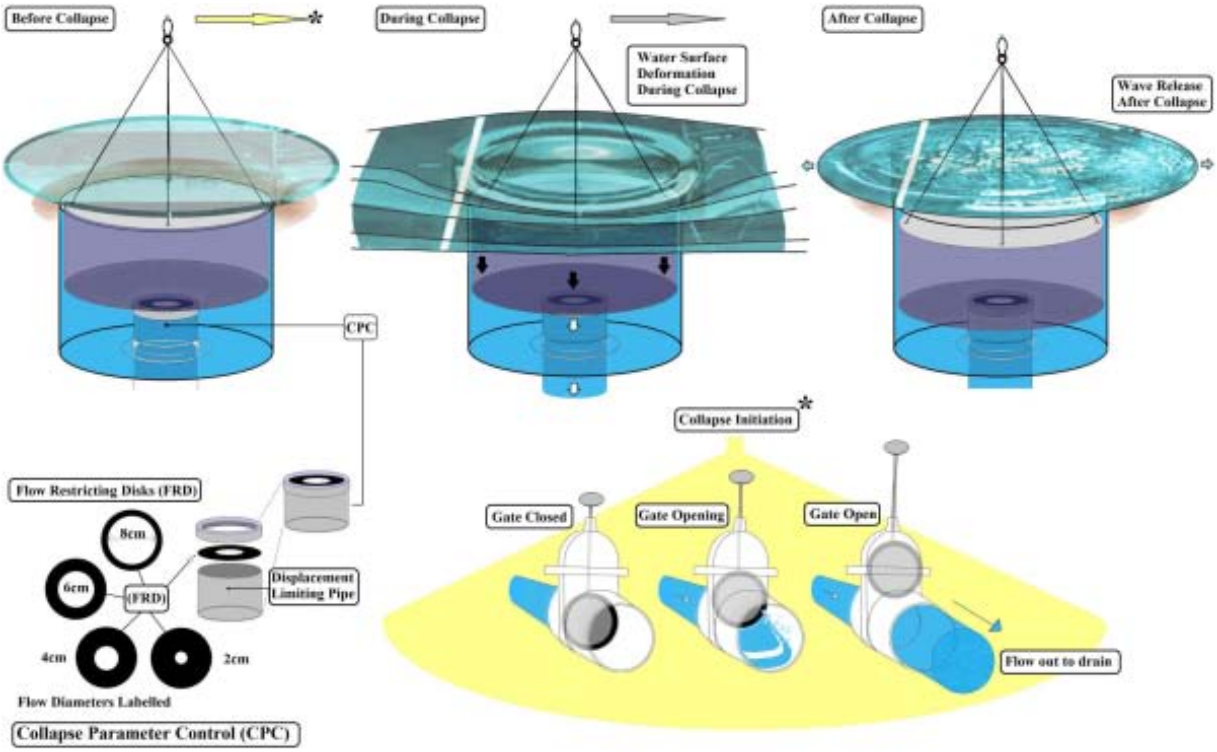

Fig. 1.: Experimental apparatus.

<1000m. These conditions show that near source mega-tsunamis could be generated by many caldera forming events e.g. Krakatoa caldera, Indonesia, Santorini caldera, Greece, Campi Flegrei caldera, Italy, Kikai caldera, Japan, Rabaul caldera, Papua New Guinea. Historic events at Santorini and Krakatoa produced waves with only 10-30m run up on coastlines indicating that these waves either rapidly decreased in height away from source or subsidence rates at these calderas were <10m/s. Unfortunately, the scale of our study prevents extrapolation of wave heights to medial and distal locations and at present subsidence rates at natural calderas are poorly constrained by limited observation. The global effects of caldera generated mega-tsunamis emphasizes the need for numerical modelling to study the propagation of caldera subsidence generated tsunamis and encourages innovative new techniques to estimate subsidence rate during large caldera forming events.

References

Gray, J. P., and J. J. Monaghan, 2003, Caldera collapse and the generation of waves: Geochemistry Geophysics Geosystems, v. 4, p. 1525-2027.

Novikova, T., G. A. Papadopoulos, and F. W. McCoy, 2011, Modelling of tsunami generated by the giant Late Bronze Age eruption of Thera, South Aegean Sea, Greece: Geophysical Journal International, v. 186, p. 665-680.

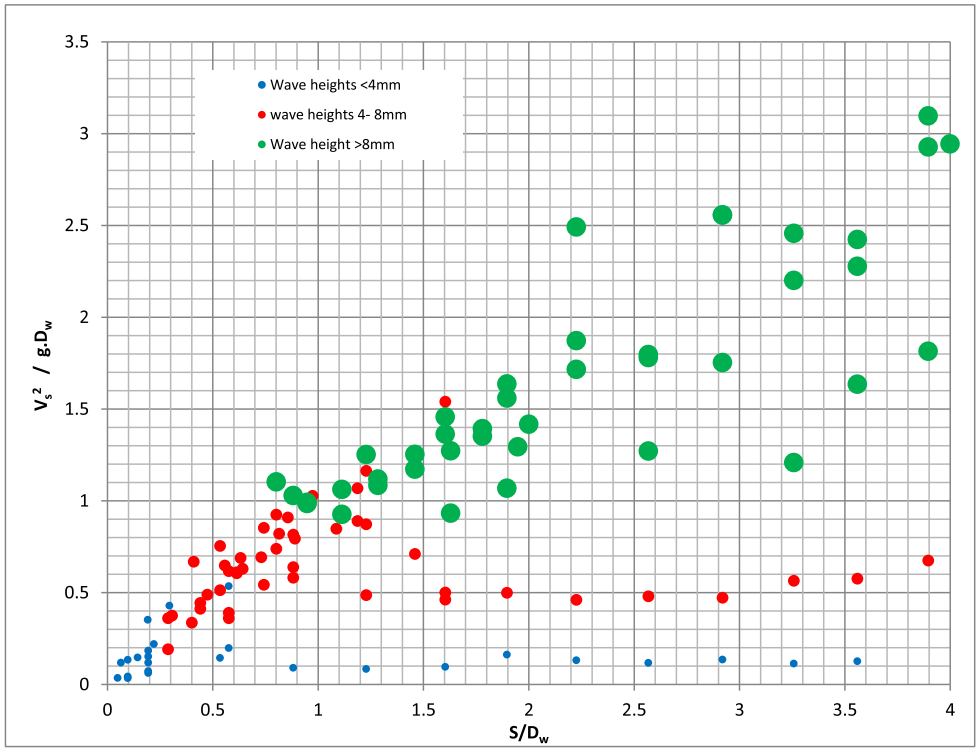

Fig. 2.: Wave height results plotted against critical dimensional parameters.

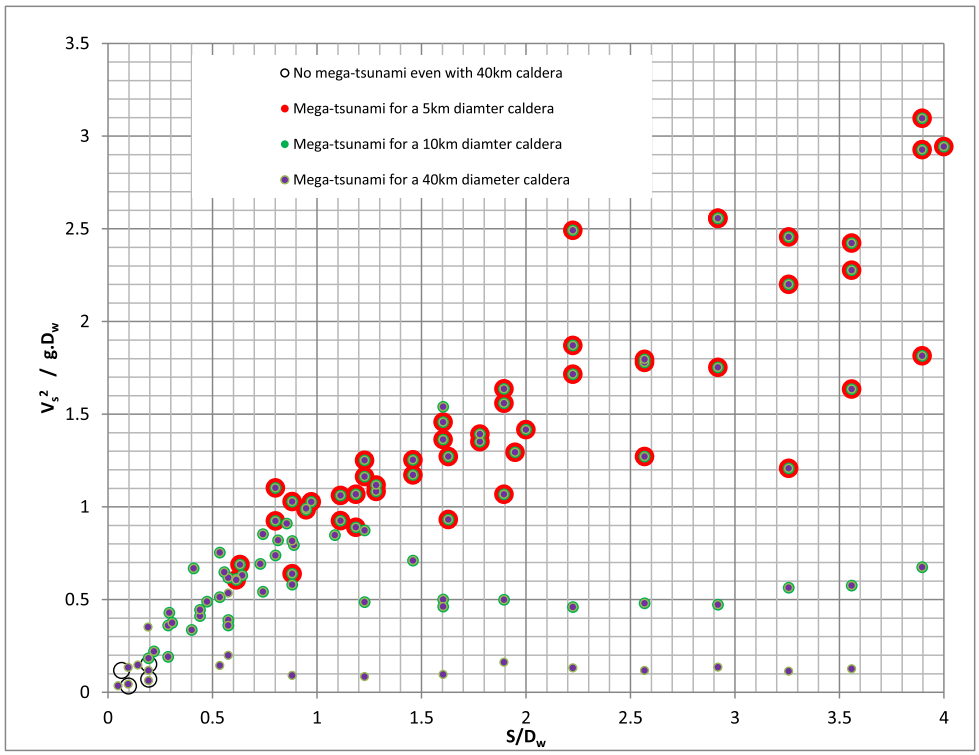

Fig. 3.: By varying the length scale of our experiments, we indicate the different conditions that submerged calderas of 5km, 10km and 40km in diameter can form mega-tsunamis.

Toward a unified dynamic model for dikes and cone sheets in volcanic systems

Olivier Galland[1], Steffi Burchardt[2], Erwan Hallot[3], Régis Mourgues[4], Cédric Bulois[4]

[1]*Physics of Geological Processes (PGP), University of Oslo, Norway*
[2]*Department of Earth Sciences, Uppsala University*
[3]*Géosciences Rennes, University of Rennes1, France*
[4]*L.P.G.N, Université du Maine, France*
e-mail: *olivier.galland@fys.uio.no*
session: *Volcanism and Volcanotectonics*

Swarms of hundreds to thousands of igneous sheet intrusions represent the main magma pathways through the Earth's brittle crust. Field observations in extinct and exhumed volcanic areas worldwide have identified different geometries of sheet intrusions, among which (i) vertical dikes [e.g., Pollard, 1987; Rubin, 1995], (ii) inclined cone sheets [Burchardt et al., 2011], and (iii) horizontal sills [e.g. Burchardt, 2008; Galland et al., 2009] represent the main types (Figure 1). The spatial association and the close temporal relations between cone sheets and dikes led Walker [1992] to propose that they may be fed by a common source. The following key question, however, remains unsolved: what are the physical parameters that lead either to vertical dikes or cone sheets in volcanic systems, and particularly those fed from the same source?

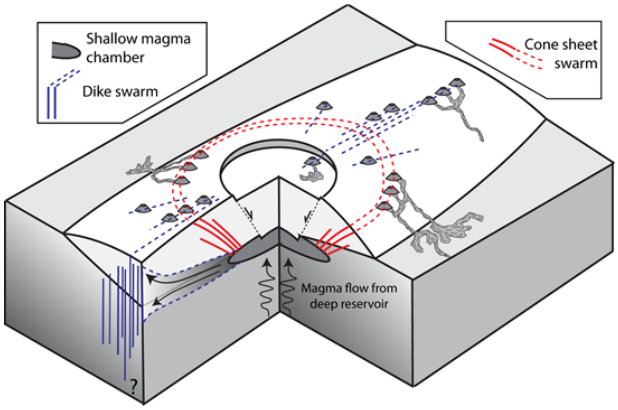

Fig. 1.: a) Schematic drawing of the characteristic structure of volcano plumbing systems [Galland et al., in revision]. A shallow magma reservoir may feed different conduits, such as dikes (blue) or cone sheets (red). Some of the dikes and cone sheets may result in eruptive fissures.

Here we present scaled laboratory experiments that reproduced dike and cone sheet intrusion geometries under controlled conditions. The model rock is crystalline silica flour. Its average grain size is $\sim$15 μm. The flour fails according to a Mohr-Coulomb criterion, and we measured its cohesion (C) and friction coefficient (μ) at 369 $\pm$ 44 Pa and 0.81 $\pm$ 0.06, respectively [Galland et al., 2009]. The model rock is a vegetable oil. It is solid at room temperature but melts from $\sim$31°C. The viscosity of the oil is poorly temperature-dependant [Galland et al., 2006]; we injected it at $\sim$50°C, temperature at which its viscosity is $\eta \sim 2 \cdot 10^{-2}$ Pa s and density is 890 kg m^{-3}.

The experimental apparatus used in this study is a modified version of that of Galland et al. [2009], Galland [2012] and Galland et al. [in revision]. The models laid in a 40 cm wide square box filled with a layer of compacted silica flour of variable thickness and controlled density of 1050 kg m^{-3} (Figure 2). A pump injected the oil at constant and controlled flow rate through a circular inlet of variable diameter (d) into the model, and the oil intruded directly into the silica flour. After the experiments, the oil solidified and the intrusion was excavated to observe its shape.

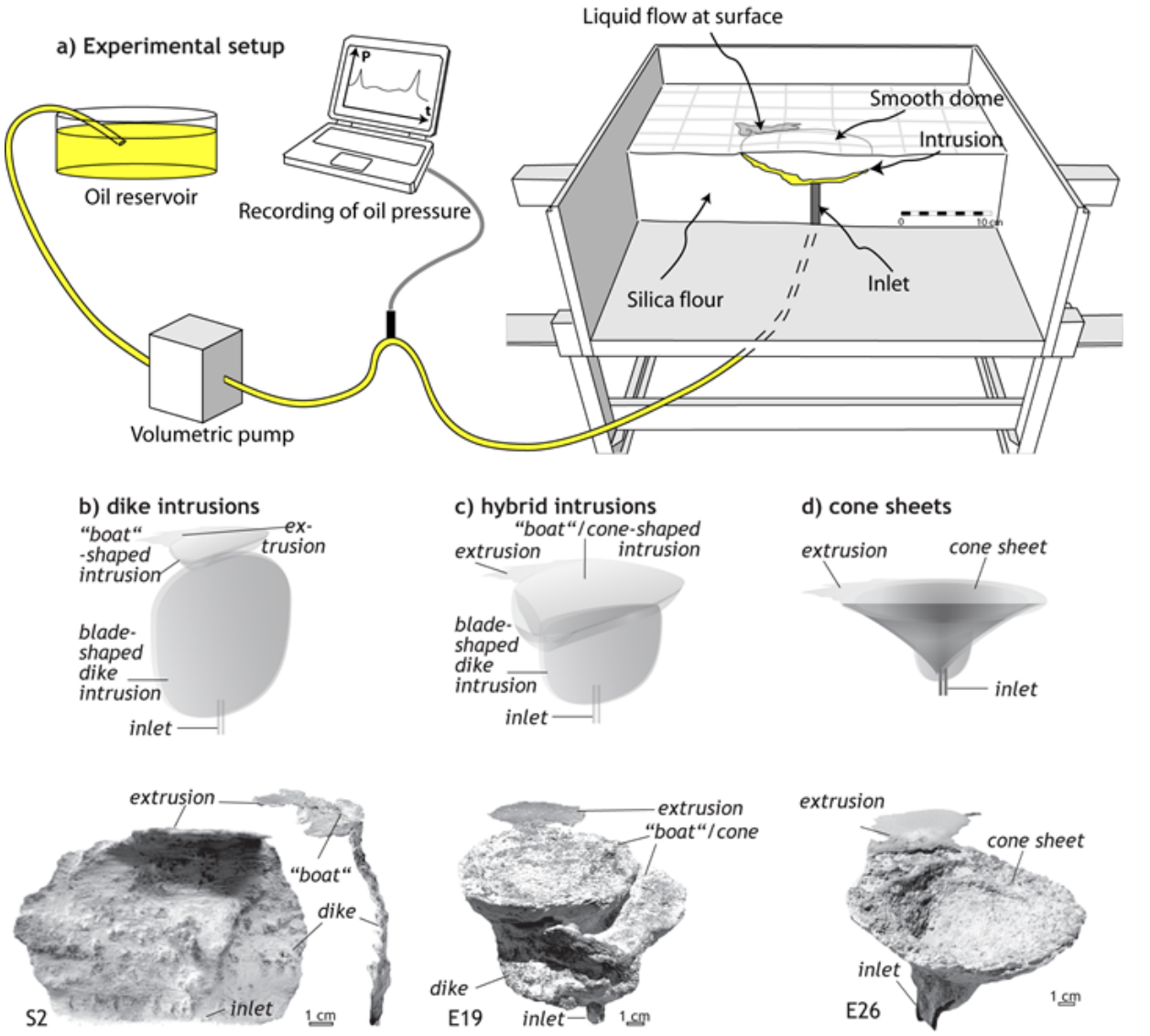

Fig. 2.: a) Drawing of the experimental apparatus used in this study [modified after Galland et al., 2009; Galland, 2012]. b) Schematic drawing (top) and photograph (bottom) of a typical dike produced during the experiments and excavated from the host-powder after solidification of the oil [Galland et al., in revision]. The dike initiated from the inlet at the bottom and fed an elongated v-shaped, or "boat"-shaped, sheet intrusion to the very top. c) and d) Schematic drawings (top) and photographs (bottom) of typical excavated hybrid and cone sheet intrusions, respectively.

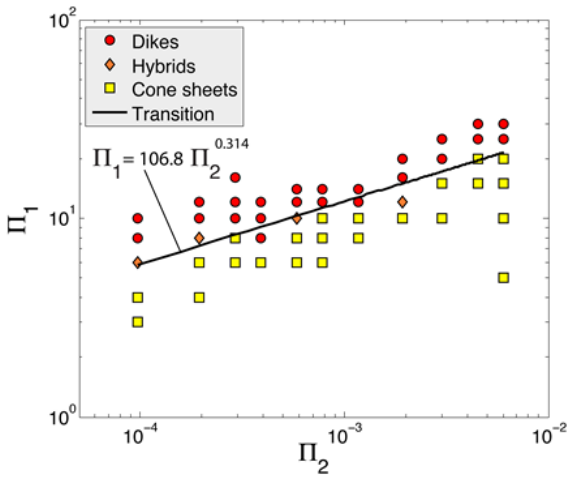

Fig. 3.: Log-log dimensionless phase diagram distinguishing the intrusion shapes obtained in the 52 experiments of this study: dikes (red circles), hybrid intrusions (orange lozenges), and cone sheets (yellow squares) [Galland et al., in revision]. Π_1=h/d and Π_2=vη/Cd. The dikes and cone sheet experiments plot in two distinct fields, separated by a line, expressed by the power law $\Pi_1 = 106.8 \cdot \Pi_2^{0.314}$.

We present the results of 52 experiments, in which we varied independently three controlled parameters: the depth of the injection inlet (h) below the free surface, the diameter of the injection inlet (d), and the oil injection velocity (v). The experiments produced two basic sheet intrusion morphologies that compare to natural dikes and cone sheets, as well as a transitional type of intrusion referred to as hybrid intrusions (Figure 2b, c, d).

We performed a dimensional analysis of the studied system and identified two dimensionless parameters that account for the coupling between the host rock and the magma source: a geometric dimensionless ratios (Π_1=h/d), which describes the geometry of the magma source, and a dynamics dimensionless ratio (Π_2=vη/Cd), which compares the local viscous stresses in the flowing magma to the host-rock strength. Plotting our experiments against these two numbers results in a phase diagram evidencing a dike and a cone-sheet field, separated by a sharp transition that fits a power law (Figure 3). This result shows that dikes and cone sheets correspond to two distinct physical regimes of magma emplacement in the Earth's crust. Cone sheets preferentially form when their source is shallow relative to their size, when the magma influx (or viscosity) is large, or when the host rock is weak. In addition, both dikes and cone sheets may form from the same source, the shift from one regime to the other being then controlled by magma dynamics, i.e. different values of Π_2.

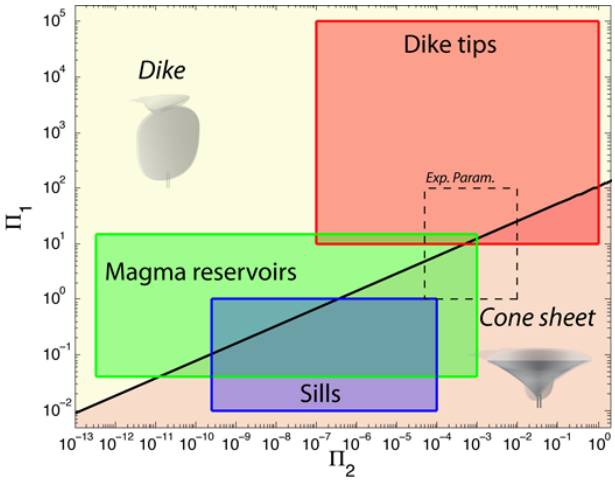

Fig. 4.: Graph comparing the experimental results of this study (dashed line box) to characteristic geological values of Π_1 and Π_2 [Galland et al., in revision]. The dike-to-cone sheet transition is extrapolated from experimental phase diagram of Figure 3. Geological boxes correspond to dike tips (red), magma reservoirs in volcanoes (green) and shallow sills in sedimentary basins (blue).

In order to test the relevance of our empirical law highlighted in Figure 3, we extrapolate it over the geological ranges of Π_1 and Π_2, and compare it with magmatic feeders of dikes and cone sheets of different scales and shapes. In Figure 4, we consider three main types of magmatic feeders leading to dikes and/or cone sheets: (i) magmatic reservoirs in central volcanoes, which feed both dikes and cone sheets (Figure 1a); (ii) sills in sedimentary basins dominantly leading to the formation of sub-circular inward-dipping inclined sheets; (iii) dike tips, considered as local moving magma sources, which dominantly propagate as dikes or sometimes split into V-shaped, boat-

shaped or cup-shaped intrusions. The excellent match between our experimental results and geological data from various magmatic feeding systems suggest that our empirical dike-to-cone sheet power law transition can be extrapolated to a wide range of magmatic settings. This indicates that our experimental models capture general magma emplacement mechanisms, reconciling existing specific models of distinct magmatic feeding systems.

References

Burchardt (2008), New insights into the mechanics of sill emplacement provided by field observations of the Njardvik Sill, Northeast Iceland, J. Volcanol. Geotherm. Res., 173(3-4).

Burchardt et al. (2011), Three-dimensional geometry of concentric intrusive sheet swarms in the Geitafell and the Dyrföll volcanoes, eastern Iceland, G3, 12(7).

Galland (2012), Experimental modelling of ground deformation associated with shallow magma intrusions, Earth Planet. Sci. Lett., 317-318(0).

Galland et al. (2009), Experimental modelling of shallow magma emplacement: Application to saucer-shaped intrusions, Earth Planet. Sci. Lett., 277(3-4).

Galland et al. (2006), Use of vegetable oil and silica powder for scale modelling of magmatic intrusion in a deforming brittle crust, Earth Planet. Sci. Lett., 243.

Galland et al. (in revision), Toward a unified model for dykes versus cone sheets in volcanic systems, J. Geophys. Res.

Pollard (1987), Elementary fracture mechanics applied to the structural interpretation of dikes, edited by H. C. Halls and W. F. Fahrig, Geological Association of Canada Special Paper.

Rubin (1995), Propagation of magma-filled cracks, Annu. Rev. Earth Planet. Sci., 23.

Walker (1992), "Coherent intrusion complexes" in large basaltic volcanoes – a new structural model, J. Volcanol. Geotherm. Res., 50(1-2).

Morphology and dynamics of explosive vents through cohesive rock formations

Olivier Galland[1], Galen Gisler[1], Øystein Thordén Haug[1,2]

[1] *Physics of Geological Processes, University of Oslo, Norway*
[2] *GFZ German Research Center for Geosciences, Holmholz Center Potsdam, Potsdam, Germany*
e-mail: *olivier.galland@fys.uio.no*
session: *Volcanism and Volcanotectonics*

Shallow explosive volcanic processes, such as kimberlite volcanism, phreatomagmatic and phreatic activity, produce volcanic vents exhibiting a wide variety of morphologies, including vertical pipes and V-shaped vents. So far, most studies on explosive eruption dynamics have focused on the processes within existing magmatic conduits, i.e. magma degassing and fragmentation, assuming that the walls were infinitely rigid [Melnik et al., 2005, Starostin et al., 2005, Dellino et al., 2007]. Hence, these studies were not suitable for unraveling the formation of explosive vents.

In this study we report on experimental and numerical models designed to capture a range of morphologies in an eruptive system. Using dimensional analysis, we identified key governing dimensionless parameters, in particular the gravitational stress-to-fluid pressure ratio ($\Pi_2 = P/\rho gh$), and the fluid pressure-to-host rock strength ratio ($\Pi_3 = P/C$). We used combined experimental and numerical models together to test the effects of these parameters.

The experiments build on the experiments by Haug et al. [2013] and were used to test the effect of Π_2 on vent morphology and dynamics. Two distinct morphologies were observed in the experiments: vertical pipes (Figure 1a) and diagonal fractures (Figure 1b). A phase diagram demonstrates a separation between morphologies, with vertical structures occurring at high values of Π_2, and diagonal ones at low values of Π_2 (Figure 1c).

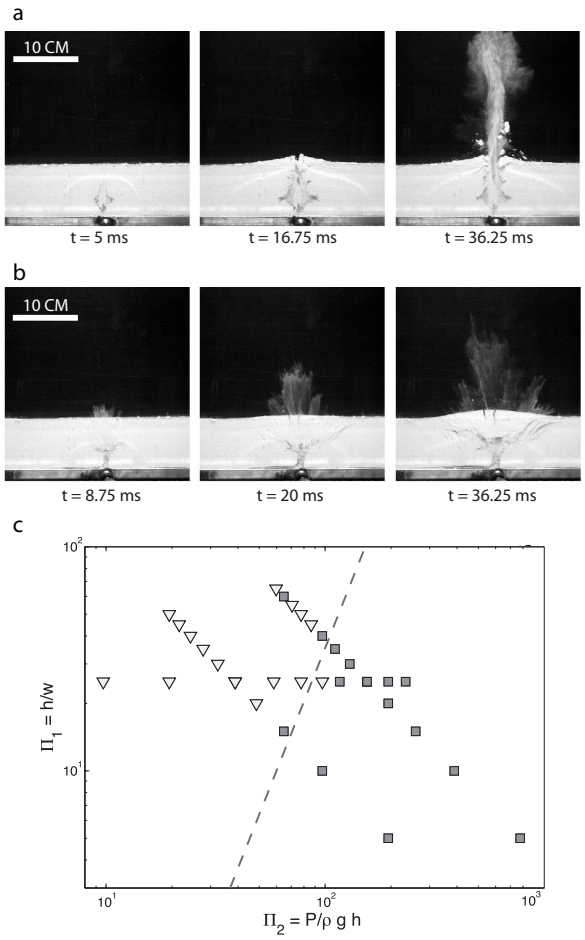

Fig. 1.: (a) Snapshots of experiments with relative high pressure compared to thickness: the air carve straight through the layer. (b) Experiment with relatively low pressure compared to the thickness of the layer: diagonal fractures propagate towards the surface. (c) Phase diagram showing that the two morphologies are determined by Π_1 and Π_2

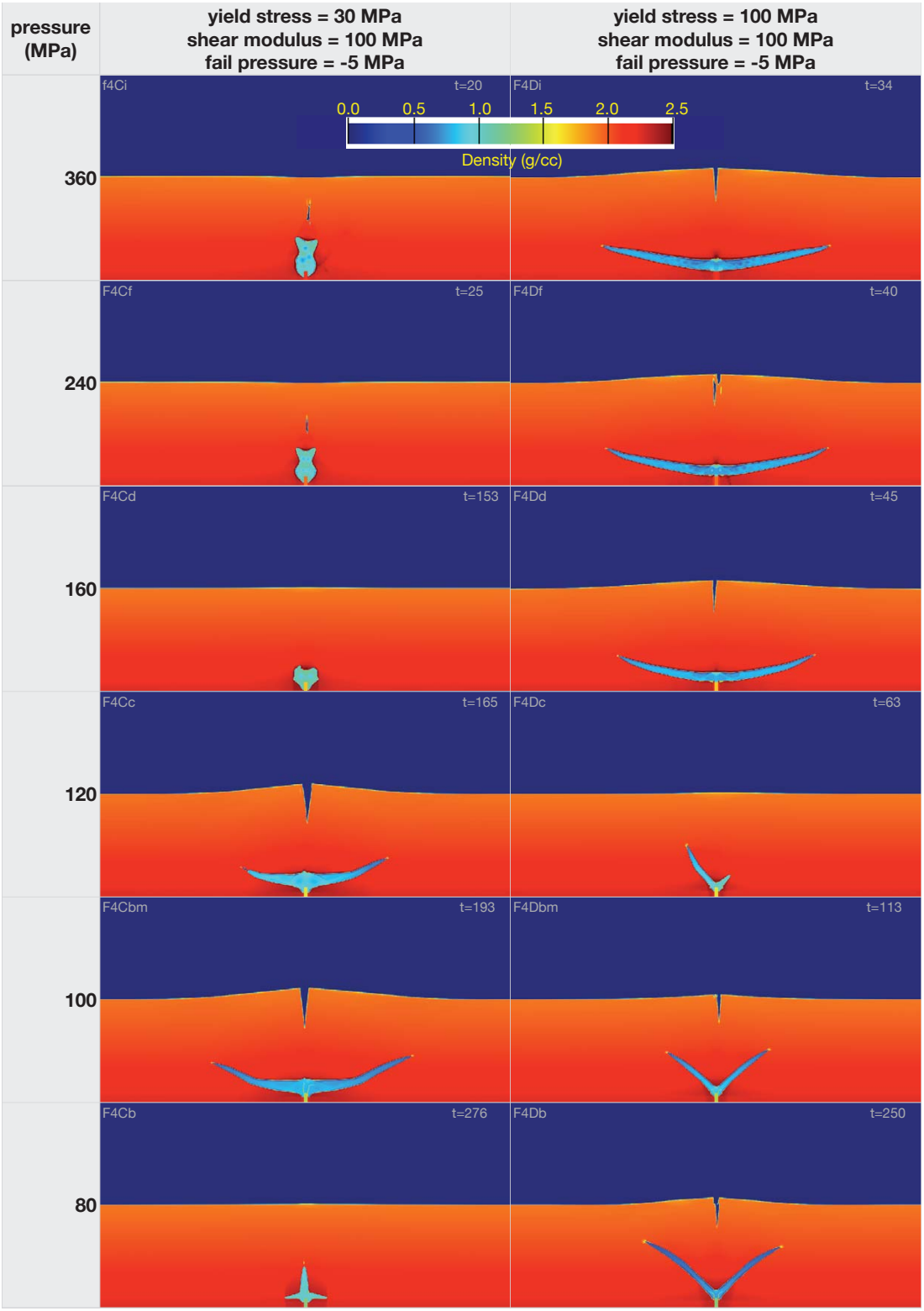

Fig. 2.: Phase diagram showing snapshots of numerical simulations. It is observed that for high value of Π_3 vertical pipes, for low values of Π_3 diagonal pipes and for intermediate Π_3 horizontal sills are produced.

The numerical simulations were used to test the effect of Π_3 on vent morphology and dynamics. In the numerical models we see three distinct morphologies: vertical pipes are produced at high values of Π_3, diagonal pipes at low values of Π_3, while horizontal sills are produced for intermediate values of Π_3 (Figure 2).

The distribution of stress (Figure 3) reveal that vertical pipes form by plasticity-dominated yielding for high-energy systems (high Π_2 and Π_3), whereas diagonal and horizontal vents dominantly form by fracturing for lower-energy systems (low Π_2 and Π_3).

Although our models are 2-dimensional, they suggest that circular pipes result from plastic yielding of the host rock in a high-energy regime, whereas V-shaped volcanic vents result from fracturing of the host rock in lower-energy systems.

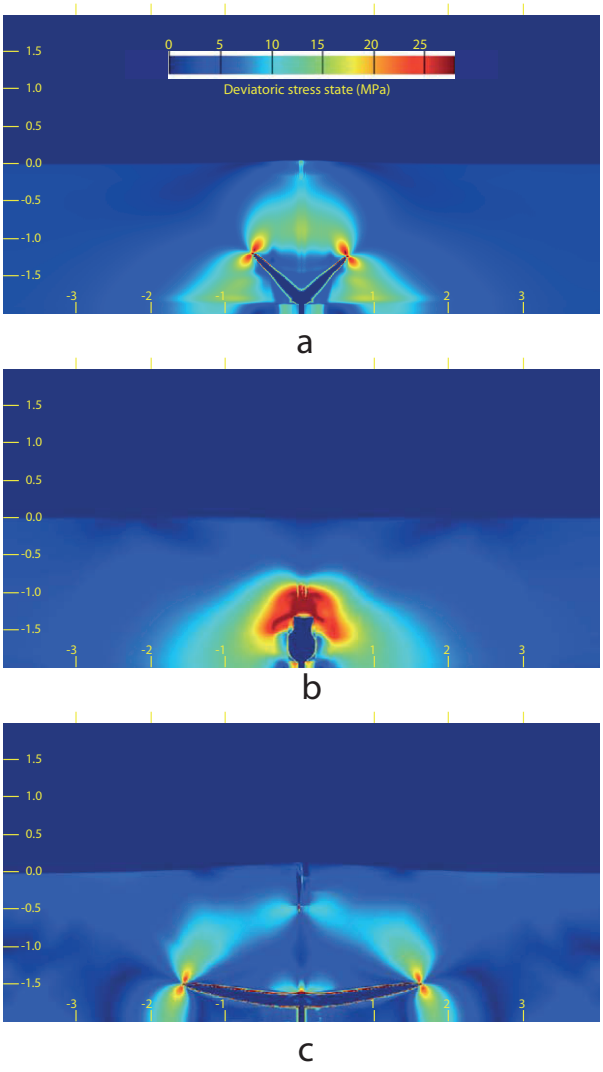

Fig. 3.: Snapshots of the deviatoric stress for the three morphologies observed in the numerical simulations. The diagonal fractures, as well as the horizontal sills have a distribution of stress compatible with elastic fracturing. The vertical pipes, however, display distributed stress around the propagating fracture, suggesting a plastic yielding.

References

P. Dellino, B. Zimanowski, R. Büttner, Luigi La Volpe, D. Mele, and R. Sulpizio. Large-scale experiments on the mechanics of pyroclastic flows: Design, engineering, and first results. Journal of Geophysical Research: Solid Earth (1978-2012), 112(B4), 2007.

Ø. T. Haug, O. Galland, and G. Gisler. Experimental modelling of fragmentation applied to volcanic explosions. Earth and Planetary Science Letters, 384:188-197, 2013.

O Melnik, A.A. Barmin, and R. S. J. Sparks. Dynamics of magma flow inside volcanic conduits with bubble overpressure buildup and gas loss through permeable magma. Journal of Volcanology and Geothermal Research, 143 (1):53-68, 2005.

A. B. Starostin, A. A. Barmin, and OE Melnik. A transient model for explosive and phreatomagmatic eruptions. Journal of volcanology and geothermal research, 143(1):133-151, 2005.

Temporal changes in mantle wedge geometry and magma generation processes in the Central Andes: towards linking petrological data to thermomechanical models

Rosanne Heistek[1], Melanie Brandmeier[1], Heye Freymuth[1,2], Gerhard Wörner[1]

[1]*Institut für Geowissenschaften, Universität Göttingen, Goldschmidtstr. 1, 38077 Göttingen, Deutschland.*
[2]*Dept. Earth Sciences, Univ. Bristol, Uk*
e-mail: *rheiste@gwdg.de*
session: *Volcanism and Volcanotectonics*

Temporal and spatial patterns of Neogene ignimbrite magmatism in the Central Andes were analyzed using GIS and geostatistical modeling. We compiled a comprehensive ignimbrite database using available literature, satellite imagery and geochemical data. 203 individual ignimbrite sheets were digitized in GIS, for which geochemical, isotopic (partly), and geochronological data are available from literature sources and own data (`http://www.arcgis.com/home/item.html?id=47038ddc0628473f9f0ce67aa2eff8be`). Based on this analysis, we estimate composition, volumes and sources of erupted ignimbrite magmas through space and time for five segments of the Central Andes.

The total erupted ignimbrite magma volume is estimated to be about 31,000 km^3 for the past 30 Ma, with the highest average eruption rates (r^m) for the northern Puna segment (3.4 km^3 Ma^{-1} km $(arc)^{-1}$), followed by 0.7 km^3 Ma^{-1} km $(arc)^{-1}$ for the Altiplano. For Southern Peru, r^m is smaller (0.5 $km^3 Ma^{-1} km$ $(arc)^{-1}$), which might be due to the lack of knowledge about intra-caldera volumes. Furthermore there is a clear N-S "younging" of ignimbrite pulses. Major pulses of high magma eruption rate occurred at 19-24 Ma (e.g. Oxaya, Nazca Group), 13-14 Ma (e.g. Huaylillas ignimbrites), 6-10 Ma (Altiplano and Puna ignimbrites, e.g. Vilama ignimbrite) and 3-6 Ma (e.g. Atana, Los Frailes, Toconao). In contrast, small volume young ignimbrites from 0-3 Ma (e.g. Lauca-Perez, Purico) do not show the spatio-temporal pattern of eruptions that are documented for the large- volume ignimbrite flare-ups.

Compositional and Sr-O isotopic data indicate that ignimbrite magmas are more crustally derived in younger flare-ups in the Southern Central Andes (up to 50 % crustal melts) compared to older ignimbrites in the north (only up to 20 % crustal melts). This suggests that thermal conditions, juvenile magma production in the mantle, thickness, and/or composition of the crust must have been different along the Central Andes at the time when ignimbrite flare up magmas formed.

The amount of juvenile magmas that entered the crust and the degree and volume of partial melting within the crust can thus in principle be constrained in time and space by these data. Such data are essential in order to understand the thermal evolution of the Andean crust in space and time.

The Miocene large-volume, plateau forming ignimbrites always overly a pronounced unconformity and occur after a time with no magmatism. They are followed, however, by andesitic arc magmatism characterized during the Late Miocene by low angle, large-volume ($\sim$2.2 km^3 per lava flow) volcanic shields with long single lava flows up to 20 km. These shields are succeeded by younger and more evolved steeply-sided strato-cones that characterize much of the CVZ active volcanic

front for Pliocene-Quaternary times. Andesites in such young stratovolcanoes (∼0.7 km^3 per lava flow) are often characterized by amphibole phenocrysts.

In principle, the transition between these andesite regimes could be due to:

1. a change in the mantle melting regime from decompression (hot and dry?) to flux melting (wet and lower T?),

2. different rates in magma production and effusion, and

3. different P-T-regimes of magma evolution within the crust as is shown by the depletion in HREE and Y from Miocene to Pleistocene volcanic rock caused by a residual garnet after crustal assimilation in a thickened crust.

To understand the shift from andesite shields to stratovolcanoes we studied Miocene to modern Central Andean volcanic rocks that represent different ages but are similar in petrography and composition in order to test differences in processes of magma generation. Based on a survey of ∼1300 chemical analyses of lava samples (`http://andes.gzg.geo.uni-goettingen.de/`) we selected three representative sample types: (1) most mafic samples (50-55 % SiO_2), (2) intermediate andesites representing 63 % of the data (55-60 % SiO_2), and (3) felsic samples (60-65 % SiO_2), all of which were identified before as important end-member magma type in the Central Andes. Using a range of geothermometers, hygrometers and MELTS modelling we show that the P-T parameters at the time of eruption, for a given composition, remained surprisingly constant trough time and throughout the Central Andes (e.g. 975 °C to 985 °C for 2-px thermometry). Moreover, the depth of the last (phenocryst) crystallization of Miocene to Present magmas took place between 9 and 3.5 km throughout Andean history. These observations clearly indicate that estimated temperatures only reflect the late crystallization history at shallow levels and that any distinct regimes of magma formation in the mantle wedge that may have existed are entirely dampened out during the passage through the crust. Density, viscosity and degassing of andesite magmas control the latest stages of ascent and crystallization and these parameters are independent of crustal conditions, subduction geometry and mantle wedge conditions. Therefore, the thickened upper crust not only serves as a chemical filter for mantle wedge magmas but also controls (and synchronizes) P-T conditions of crystallization as recorded in erupted products.

Deep evolution at the level of the magma sources and lower crust, where assimilation and magmatic differentiation takes place, is thus completely decoupled from the shallow processes of late crystallization. Therefore only the rate of effusion, and by implication, magma production and upper crustal stress regime remain as primary factors that may have influenced differences between Miocene and Recent magmatic products.

Since the sequence of distinct magmatic regimes (plateau-ignimbrites, shield andesites and evolved stratovolcanoes) is diachronous during the past 26 Ma of Andean evolution with ages getting younger from N to S. This suggests control by "deeper" processes guided by the geometry of the slab and the thermal evolution of the upper plate during Andean orogeny. As patterns, timing of events, subduction parameters and magma production rates in the mantle wedge change regionally and temporally during ongoing thickening of the Central Andean crust, the upper plate reacts at any given location individually to these changes according to its present thermal state, crustal composition, magmatic history and tectonic stress conditions at that time and space.

We propose that large-volume ignimbrite eruptions occurred in the wake of subduction of the Juan-Fernandez ridge that passed below the Central Andes from N to S during the past 25 Ma. This event resulted in compression, uplift, low angle subduction (flat slab) and fluid release in a first stage, followed by massive inflow and melting of asthenospheric mantle after the passing of the ridge when the slab again steepened rapidly. This in turn caused massive melting within the crust

aided by advective heat transport shortly after slab steepening. Differences in chemical and isotopic composition of the large-volume ignimbrites are related to changes in crustal thickness, and its "preconditioning" during the Anden orogeny over time.

The change in effusion rate during the Miocene to Pliocene/Quarternary may be the only parameter that relates to changing angles and/or convergence rates of the slab. Since only convergence rates changed during the last 26 Ma (Sérbier and Solar, 1991), this parameter likely controls magmatic activity (Cagnoicle et al., 2007). In southern Peru, Miocene voluminous magmatic activity correlates with high convergence rates, both decreasing in the last 10 Ma (Sébrier and Soler, 1991).

Previous model predictions for arc magmatism (Sobolev et al., 2006) follows from the comparison between the evolution of tectonic shortening and the evolution of the mantle temperature beneath the magmatic arc. Processing the delamination material throught the asthenospheric wedge by corner flow results in an increasing shortening rate. Simultaneously, the temperature of the asthenospheric wedge beneath the magmatic arc decreases, which in turn should lead to reduced magmatic activity. However, apart from the Puna (Kay and Kay, 1993) and Northern Altiplano (Back and Zandt., 2002; Yuan et al., 2002)) no evidence exists for mantle lithosphere delamination in the Central Andes. Therefore a new model based on our volumes, eruption rates, petrological constraints and the movement of the Juan Fernández ridge should give a better understanding of the controlling factors of arc magmatism.

References

Back SL, Zandt G (2002) The nature of orogenic crust in the Central Andes. J Geophys Res 107:n doi 10.1029/2000JB000124

Cagnioncle AM, Parmentier EM, Elkins-Tanton LT (2007) Effect of solid flow above a subducting slab on water distribution and melting at convergent plate boundaries. J Geophys Res 112: B09402

de Silva, S., Gosnold, W.D. (2007) Episodic construction of batholiths: Insights from the spatiotemporal development of an ignimbrite flare-up. J. Volcanol. Geotherm. Res. 167: 320–335.

Kay RW, Kay SM (1993) delamination and delamination magmatism. Tectonophysics 219:177 - 189

Sébrier, M., Solar, P. 1991. Tectonics and magmatism in the Peruvian Andes from late Oligocene time to the Present. Geological Society of America 265, 259–278.

Sobolev SV, Babeyko AY, Koulakov I, Oncken O (2006) Mechanism of the Andean orogeny: insight from numerical modeling. In: Oncken O, Chong G, Franz G, Giese P, Götze H-J, Ramos VA, Strecker MR, Wigger P (eds) The Andes – active subduction orogeny. Frontiers in Earth Science Series, Vol 1. Springer-Verlag, Berlin Heidelberg New York, pp 513–536, this volume

Yáñez, G., Cembrano, J., Pardo, M., Ranero, C., Selles, D., 2002. The Challenger–Juan Fernández– Maipo major tectonic transition of the Nazca–Andean subduction system at 33–34 S: geodynamic evidence and implications. Journal of South American Earth Sciences 15, 23-38.

Yáñez, G.A., Ranero, C.R., Huene, R., Díaz, J., 2001. Magnetic anomaly interpretation across the southern central Andes (32–34 S): The role of the Juan Fernández Ridge in the late Tertiary evolution of the margin. Journal of Geophysical Research: Solid Earth (1978–2012) 106, 6325-6345.

Use of the Distinct Element Method in Volcano-tectonic Modeling

E.P. Holohan[1,2], H. Sudhaus[1], M.P.J. Schöpfer[2,3], T.R. Walter[1], J.J. Walsh[2]

[1] *German Research Centre for Geosciences (GFZ-Potsdam), Sektion 2.1 – Physics of Earthquakes and Volcanoes, Helmholtzstrasse 7, 14467 Potsdam, Germany.*
[2] *Fault Analysis Group, UCD School of Geological Sciences, University College Dublin, Ireland.*
[3] *Department for Geodynamics and Sedimentology, University of Vienna, Althanstrasse 14, Vienna, Austria.*
e-mail: *holohan@gfz-potsdam.de*
session: *Volcanism and Volcanotectonics*

Introduction

Certain volcano-tectonic processes, such as caldera collapse, flank spreading or sector collapse, involve large discontinuous (i.e. fault- or fracture-related) strains of rock masses. Analogue models can readily reproduce such deformation, but their exact scaling to natural systems is often uncertain. Numerical models scale more accurately, but the continuum-based approaches typically used to date have an inherent difficulty in simulating fracture or fault system development. Moreover, since continuum-based analytical solutions are routinely used to model geodetic data from actively-deforming volcanoes, the effects of fracturing (particularly in the sub-surface) on deduced finite deformation sources may be underestimated and misinterpreted.

Distinct Element Method (DEM) models

The DEM simulates the finite displacements and rotations of discrete particles[1]. In the 2D DEM code PFC2D[2], the particles are rigid discs (Fig. 1). The particles interact with each other and with rigid boundary walls through a contact law based on linear force-displacement and Coulomb friction. Other contact laws are also possible. Beam-like elastic bonds ('parallel bonds') can be added to hold the particles together. The bonds transmit both forces and moment, and they break if their tensile or shear strength is exceeded. As broken bonds accumulate within a particle assembly, they link together and promote further strain localisation, such that large-displacement fracture systems may ultimately develop. Consequently, the DEM material undergoes a transition from quasi-continuum behaviour to discontinuum behaviour, and so bridges past analogue and numerical approaches.

An important feature of the DEM is that material properties are defined and varied at the bond and particle scale. Bulk material properties (elasticity, strength, friction) emerge from the larger-scale interaction of particles and bonds based on the micro-scale properties. Bulk properties must therefore be calibrated by means of simulated rock deformation tests (Fig. 2). For the caldera collapse model shown here, the bulk material properties lie within the ranges characteristic of natural rock masses on a large (c. 100 m) scale [3].

Application to Pit-crater and Caldera subsidence

One suitable use of DEM models in volcano-tectonic modelling is for the simulation of the structural development of pit crater or caldera

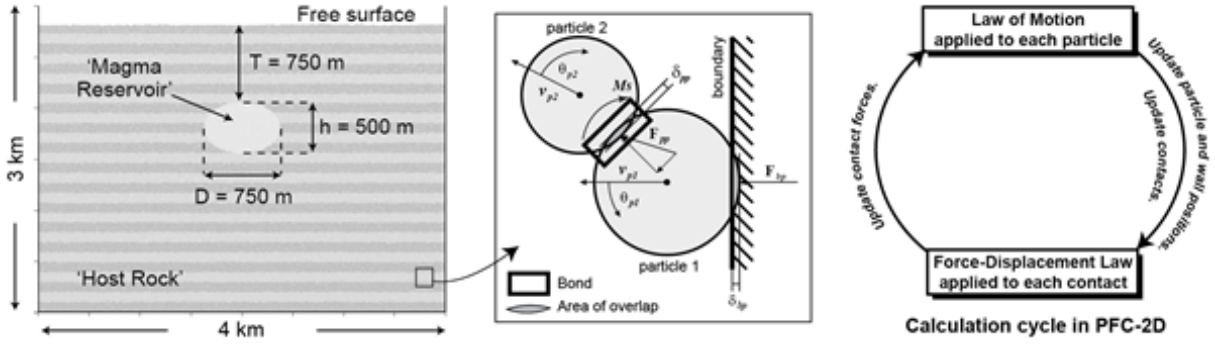

Fig. 1.: Overview of DEM as implemented in PFC-2D and applied to model caldera collapse. Left: Pre-depletion view of a collapse caldera model. Shaded light grey are non-bonded, low friction (0.01) particles that make up the simulated magma reservoir. Around this are bonded, higher-friction (0.5) particles that make up the simulated host rock. Note that the layers here are passive markers and do not represent any material heterogeneity. The boundary wall conditions are free-slip. Centre: Close up of particle-bond-boundary relations used in PFC-2D calculations. M = moment, F = force, v = particle velocity, θ = angular rotation, δ = particle-particle or particle-boundary overlap. Right: Schematic of PFC calculation cycle.

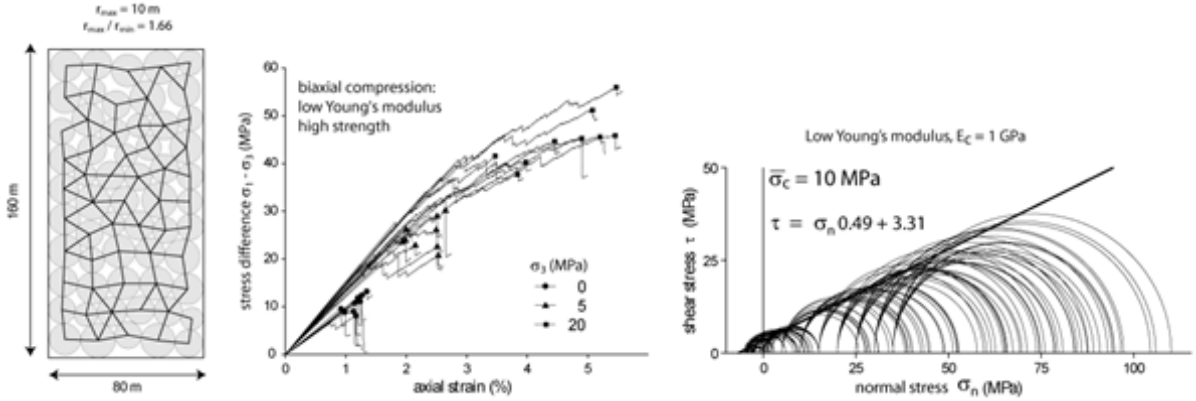

Fig. 2.: Illustration of the process for bulk property calibration in DEM models (modified from [3]). Left: Sample of the model assemblage in Figure 1 to be subjected to biaxial compression and tension tests. Centre: Stress-strain plot for biaxial compression tests at various confining pressures, each with 10 realisations (i.e. different particle arrangements). Symbols on stress-strain curves denote peak strengths at differing confining pressures (σ_3). Most of these curves' post-peak extents were removed for clarity. The pre-failure slopes of these curves indicate a confining-pressure-dependent Young's modulus of 1 – 1.4 GPa. Right: A linear Mohr-Coulomb failure envelope fitted to the biaxial compression test results. The envelope indicates a bulk material cohesion of 3.31 MPa and a friction coefficient of 0.49 for this sample (sample has particle contact modulus of 1 GPa and bond strength of 10 MPa).

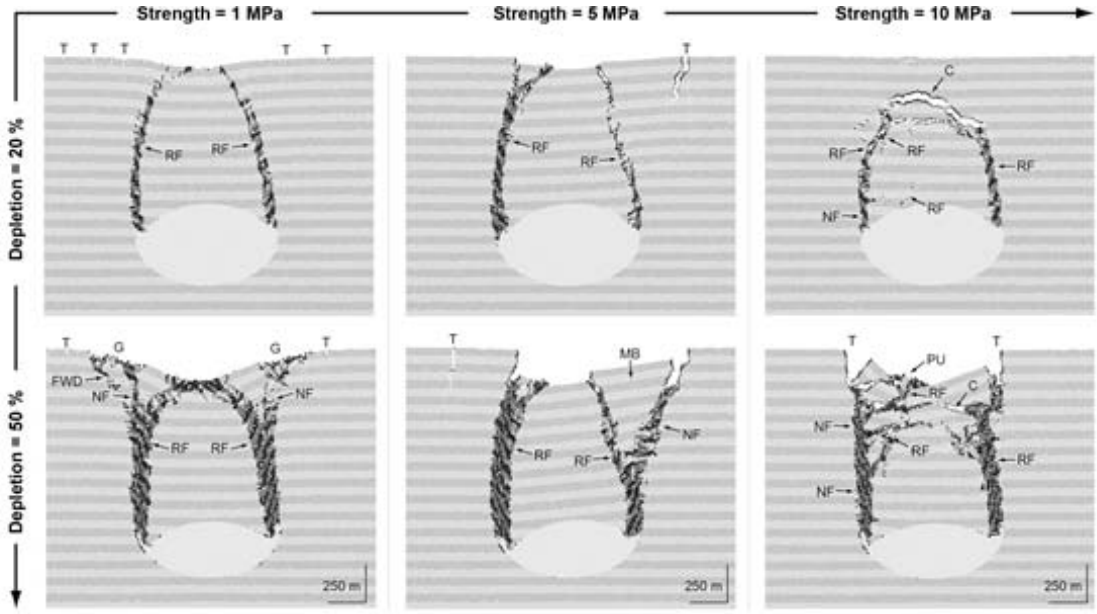

Fig. 3.: Structural development in DEM models of pit crater or caldera collapse (modified from [3]). Shown here are three models that differ only in host-rock strength (unconfined compressive strength). Each model is shown at reservoir area depletions of 20% and 50%. Strain localisation is shown by shading those particles around which the maximum finite shear strain exceeds 0.75. Structures are annotated as follows: T= tensile fracture (crevasse), RF = reverse fault, NF = normal fault, G = graben, FWD = footwall detachment, MB = marginal bench, C = cavity, PU = pop-up structure. For this geometry of the reservoir roof, low to intermediate strength models show a single central block collapse style, with near surface sagging at the lowest strength. In contrast, high strength models show a collapse style comprising the upward-migrating detachment of multiple blocks (resulting in opening and closure of ephemeral cavities) before finally forming a depression at surface.

subsidence [3, 4]. Here we illustrate the effects of host-rock strength on this development with models for which the initial model state shown above (Fig. 1). Magma withdrawal in these models is simulated by incrementally reducing the area of each reservoir particle. Resultant gravity-driven failure and fault-controlled subsidence of the overlying reservoir roof is explicitly replicated (Fig. 3).

The DEM models reproduce the main structural features seen in both analogue models and nature (cf. [3]). These include reverse faults that are steeply outward-inclined from the crater centre, as well as more peripheral near-surface tensile fractures and inward-dipping normal faults. Moreover, the DEM also reproduces strength related effect on the collapse style, such as coherent collapse with sagging at low strength and non-coherent collapse with cavity formation at high strength.

Such DEM models can also be used to examine how sub-surface fracturing may affect analytically-inferred source models for deformation at active volcanoes. By reproducing surface displacements observed at active volcanoes, such continuum-based analytical models are typically used to constrain the characteristics of the deformation source(s), e.g. magma bodies, responsible for the surface changes (cf. [5]).

Here we similarly 'blindly' fit surface displacements arising in DEM models of magma reservoir deflation to those from an analytical solution (Fig. 4), as for natural cases, but in which the extent and nature of sub-surface fracturing are known. To approximate the 2D conditions of the DEM simulation, our analytical source model comprises two intersecting rectangular dislocation planes [6] that are fixed to be perpendicular

to the 2D plane of interest and, in that direction, are extremely long relative to the model scale. In the absence of fracturing, the orientation and location of the optimum analytical source model are consistent with those of the DEM reservoir. Where significant fracturing occurs, however, the optimum analytical source may become strongly tilted and be sited in the roof above the reservoir. In such fracture-influenced cases in nature, analytical source models may hence underestimate the true reservoir depth.

Wider Application of DEM in Volcano-tectonics, Limitations and Future Directions

Other recent applications of the DEM in volcano-tectonics include simulations of volcano-spreading[7], volcano flank collapse[8], and sill intrusion[9]. That all applications published thus far have been 2D studies reflects one of the main limitations of the DEM: its computational intensity. This necessitates a trade-off between model size, particle resolution, and computing time, which particularly impacts simulations at length-scales typical for many volcano-tectonic processes.

Advances in computing power are nonetheless reducing DEM computing times, such that high-resolution 3D-DEM modelling is now an increasingly viable approach for volcano-tectonic studies. These developments open the door for the closest yet integration of volcano-tectonic models with geodetic and seismic observations.

Acknowledgements

Research grants awarded to EPH by the Irish Research Council and Marie Curie Actions.

References

[1] Cundall and Strack

[2] Potyondy, D.O. & Cundall, P.A., (2004), Int. J. Rock Mech. Mining Sci., 41: 1329–1364.

[3] Holohan, E.P. et al., (2011), J. of Geophys. Res., 116: B07202.

[4] Hardy, S., (2008), Geology, 36: 927-930.

[5] Dzurisin, D., (2007), Volcano Deformation, Springer Verlag.

[6] Okada Y., (1992), Bull. Seismol. Soc. Am. 82: 1018-1040

[7] Morgan, J. & McGovern, P. (2005), J. of Geophys. Res., 110: B05402.

[8] Thompson et al., (2010), J. Volcanol. Geotherm. Res. 192: 191-200

[9] Malthe-Sørensen et al., Geol. Soc. Spec. Pub. 234: 215-227.

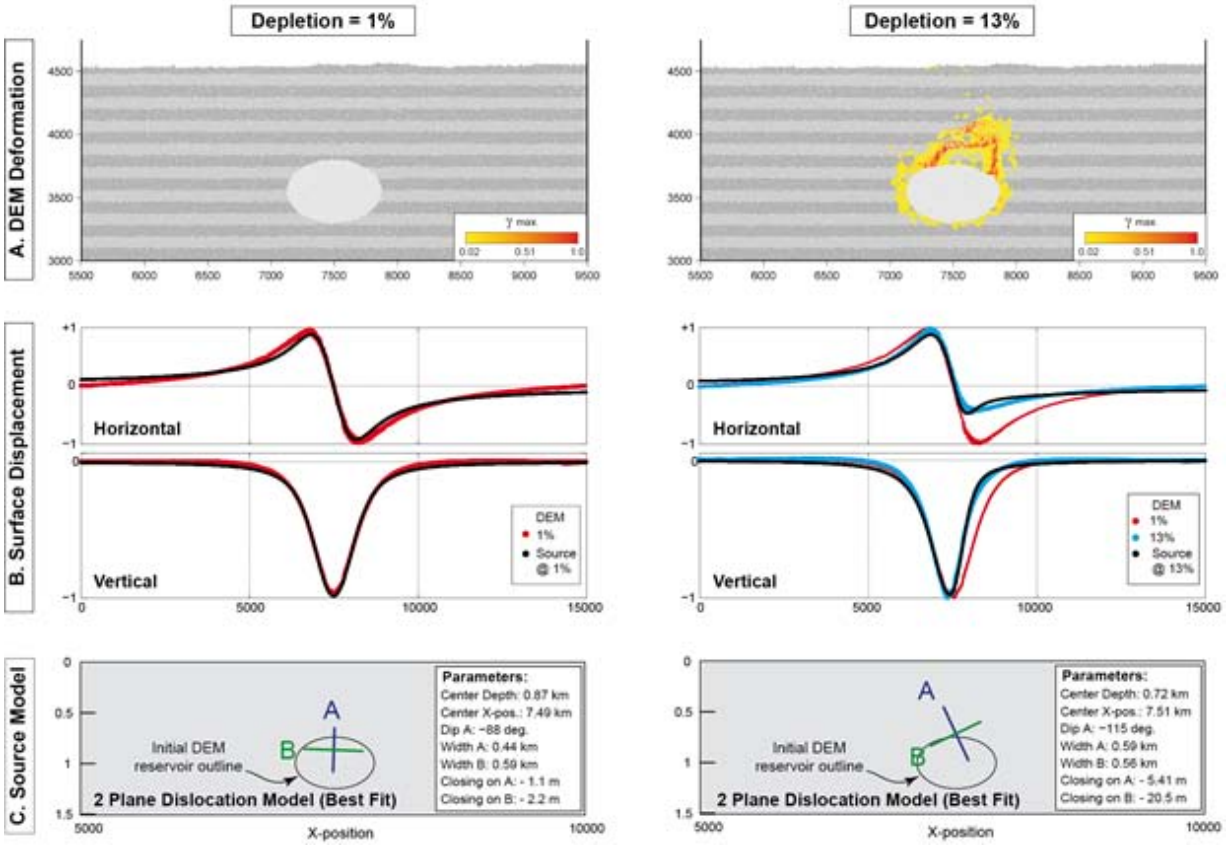

Fig. 4.: 2D-DEM model displacements and 'blindly-fitted' analytical finite sources. (A) Close-up images of deformation in a model set-up as in Figure 1, but with a height of 5 km and width of 15 km. Deformation is visualised as the maximum finite shear strain around each particle (see colour scale). The low-strain yellow areas correspond closely to areas of bond breakage. (B) Normalised horizontal and vertical components of surface displacement in the 2D-DEM model. Note the asymmetry in the displacement profiles at 13% depletion. This reflects the typically asymmetrical development of the sub-surface fracturing. (C) Optimum analytical finite deformation sources inferred for the 2D-DEM surface displacement data at each stage of depletion. The source models tested here comprise two rectangular dislocation planes[6] that are fixed to be mutually perpendicular, but all other parameters are otherwise free. To approximate the 2D conditions of the DEM models, the dislocation planes are infinitely long in the direction normal to the plane of observation. Note the changes in shape, orientation and depth of the inferred deformation source at 13% depletion. These reflect the combination of magma chamber depletion and host rock deformation.

Three-Dimensional Analysis of dike/fault interaction at Mono Basin (California) using the Finite Element Method

D. La Marra[1], M. Battaglia[2]

[1]*Dept of Sciences, Roma Tre University*
[2]*Dept of Earth Sciences, Sapienza - University of Rome*
e-mail: *daniele.lamarra@uniroma3.it*
session: *Volcanism and Volcanotectonics*

Mono Basin, Inyo Dike and the Hartley Springs Fault

Mono Basin is a northward trending graben situated east of the Sierra Nevada, extending from the northern edge of Long Valley Caldera to Body Hills, north of Mono Lake (Bursik and Sieh, 1989). The Mono-Inyo volcanic chain forms a northward trending line of volcanic vents extending within the Mono Basin (Figure 1). Several studies indicate that the youngest eruptions in the Mono-Inyo chain occurred, most likely around ∼1350 A.D. (Bailey, 1989). The existence of a dike at shallow depth between vents was confirmed by the drilling program along the trend of the Inyo Domes (Fink, 1985). Stratigraphic data suggest that a series of strong earthquakes (M ∼5.5–6.5) occurred during the North Mono-Inyo eruption sequence of ∼1350 A.D. Several geomorphologic data suggest that more than 0.5 m of mean slip occurred along the Hartley Springs Fault in numerous events at the time of the ∼1350 A.D. eruption. The spatial and temporal immediate proximity between earthquakes on the Hartley Springs Fault and Inyo Dike intrusions suggest a possible relationship between seismic events and eruptions (Bursik et al., 2003).

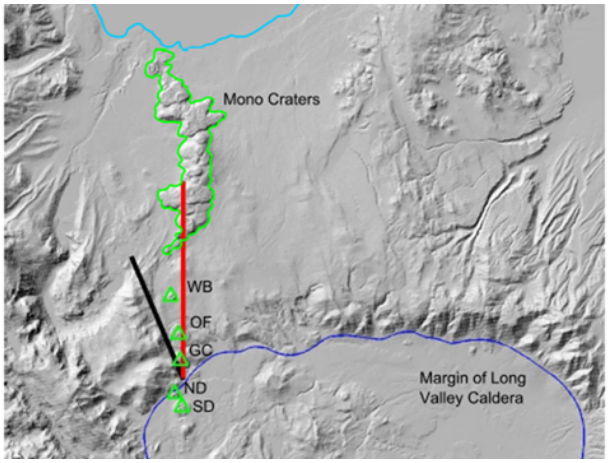

Fig. 1.: The Mono Basin area: the Inyo Dike (red line), trending approximately N-S, intercepts the Hartley Springs Fault (black line), extending from the northern rim of Long Valley caldera to the June Lake.

Three-dimensional Finite Element Method model

We use the Finite Element Method to develop a three-dimensional model of the Mono Basin and investigate the feedback mechanism between dike intrusion and slip along the Hartley Springs fault. The three-dimensional geodynamic model is implemented using the Structural Mechanics module of COMSOL Multiphysics (www.comsol.com). The crust is modeled as an elastic medium (500 km of width and length, 200 km depth), divided in cylindrical sub-domains with increasing radii to achieve a gradual refining of the mesh toward the center of the domain (Figure 2A). The medium is not homogenous: a representation of the mechanical heterogeneities in the region is obtained by combining a 40-km-long density profile across the Mono Basin (after McDonell et al., 2013; Figure 2B) with a P-waves velocity profile

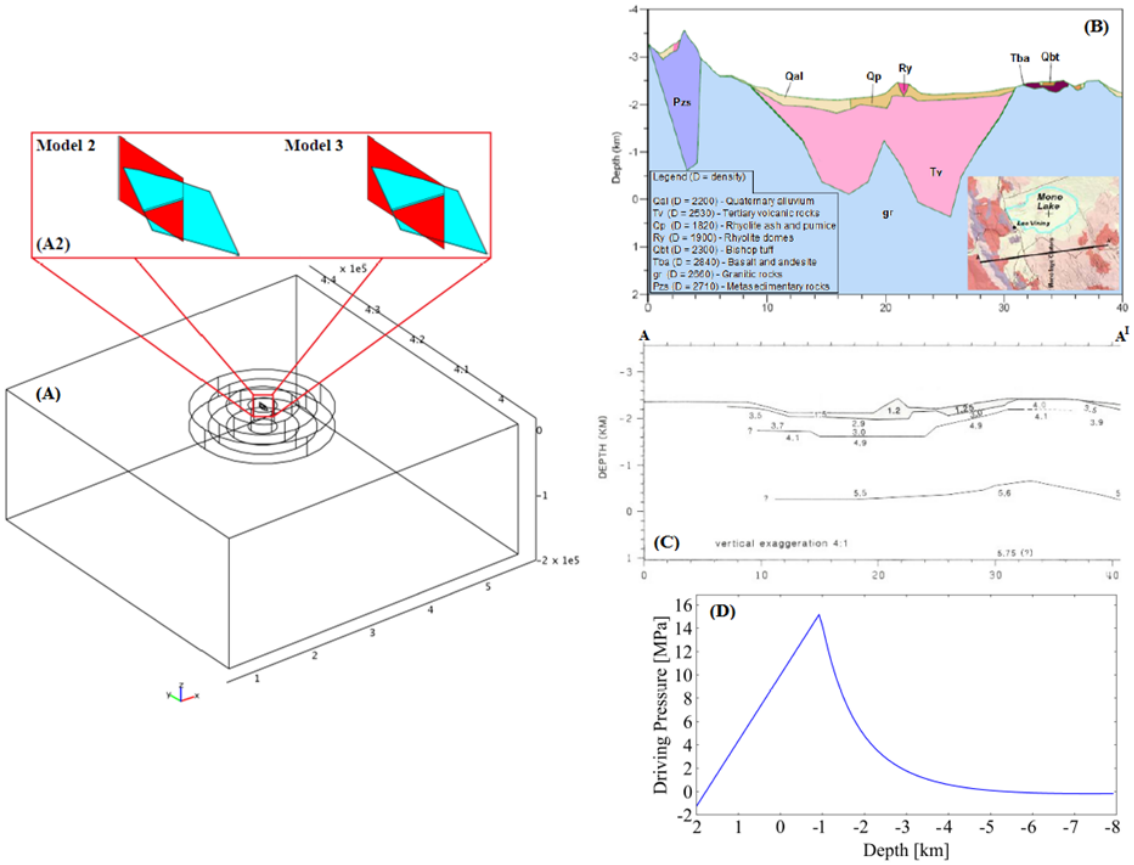

Fig. 2.: 3D geodynamic model: (A) geometry; (A2) geometry of the Inyo Dike (red surface) and the Hartley Springs Fault (light-blue surface) for the dike 10 km-length (Model 2) and 12 km-length (Model 3); (B) 40-km-long density data profile across the Mono Basin (after McDonell et al., 2013); (C) seismic profile velocities (after Hill et al., 1985) along the profile A-A' used in the models; (D) driving pressure applied as tensile component to the vertical sides of the dike (after Reches and Fink, 1988).

with depth (Hill et al., 1985; Figure 2C). To include the topography in our model (Figure 3), we used the Moving Mesh ALE module. The module allows us to insert an external vector function that assigns to each point on the surface of the model a value of altitude (topography). Using the elevation data from the Digital Elevation Model (DEM), the module distorts the mesh in the z-direction simulating the topographic relief that cover Mono Basin, Long Valley Caldera and part of the Sierra Nevada. The georeferenced topography has been exported as a CAD data file and imported to be used in the next steps of modeling.

We simulate the Hartley Springs Fault (HSF) and the Inyo Dike (ID) as mechanical discontinuities. Following Bursik et al. (2003), we approximate the HSF by a sub-vertical plane 9.5 km-long, 10 km-deep from the surface and with a 60° dip. The top edge of the fault cuts and follows the free surface to represent a relisting escarpment (Figure 4B). The Inyo Dike is simulated by a rectangular cavity 10 m-wide, and 7 km-deep with the top of the dike between 300 and 500 meters below the surface. We used the normal driving pressure values extrapolated from the model of Reches and Fink (1988) to model the opening of the Inyo dike (Figure 2D).

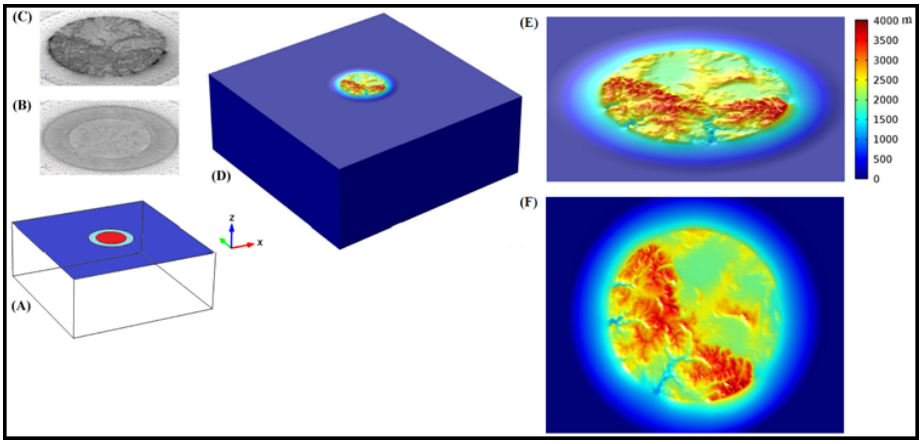

Fig. 3.: 3D FEM model with topography using the Digital Elevation Model: (A) flat domain where, on the red surface the deformed mesh is applied in order to build the topography; the light blue surface is left free to deform in order to accommodate the connection with the topography; the blue surface is kept fixed at the sea level; (B-C) mesh of red surface pre- and post-deformation; (D) domain with topography; (E-F) highlight of the topography of Mono-Basin/Long Valley Caldera.

Case (1): Inyo dike intrusion triggers earthquakes along the Hartley Springs Fault

We analyze the distribution of the Coulomb stress change (ΔCFS) along the fault plane (simulated as a passive receiver fault) for different length of the opening fracture (Model 1: dike 4, 6, 8, 10, 12, 14 km-long from the center of Mono Craters; Figure 4). In particular, we compute the percentage of fault area encouraged to slip normally and right laterally because of the dike intrusion for ΔCFS$>$ 0, 0.1, 1, 5, 10 bar (Figure 4A). We use an effective friction coefficient of 0.5 (e.g., Bursik et al., 2003). Positive Coulomb stress changes $>$ 1 bar are considered to be significant to trigger earthquakes (Walter et al., 2005). The ΔCFS changes $>$ 1 bar imply that the fault is encouraged to slip only when the dike is approaching the fault. When the dike is near the south tip of the Hartley Springs Fault, normal and right lateral slips are more difficult to initiate. Since earthquakes can be triggered by ΔCFS as small as 0.1 bar (Walter et al., 2005 and reference therein), our first numerical experiments investigate seismic triggering for values of ΔCFS $>$ 0.1 bar. In this case, when the dike is 10 km-long, close to the location of the Obsidian Dome, about 46 % of the fault plane may slip with a release of energy equal to an earthquake of magnitude 6.0, consistent with observed geological data. When the dike is 12 km-long, with its southern tip close to Glass Creek, about 42 % of the fault may slip with the possibility to trigger an earthquake of magnitude 6.0.

Case (2): slip along the Hartley Springs fault facilitates the opening of the Inyo dike

The Hartley Springs Fault is simulated (in Model 2-3, Figure 2 A2) creating "master-slave" contact pairs between subdomains to take into account the ratio of contacts and stress transfer between the planes. We move only the part of the fault that may slip (ΔCFS $>$ 0.1 bar; Figure 4B).

We run numerical experiments both for a 10 km long dike for a slip along the HSF equivalent to an earthquake of magnitude 6.0 (Model 2), and a dike 12 km-long for a slip along the HSF equivalent to an earthquake of magnitude 6.0 (Model 3). The numerical results show that when the dike is near Obsidian Flow (dike 10 km-long), a slip along the fault can increase the

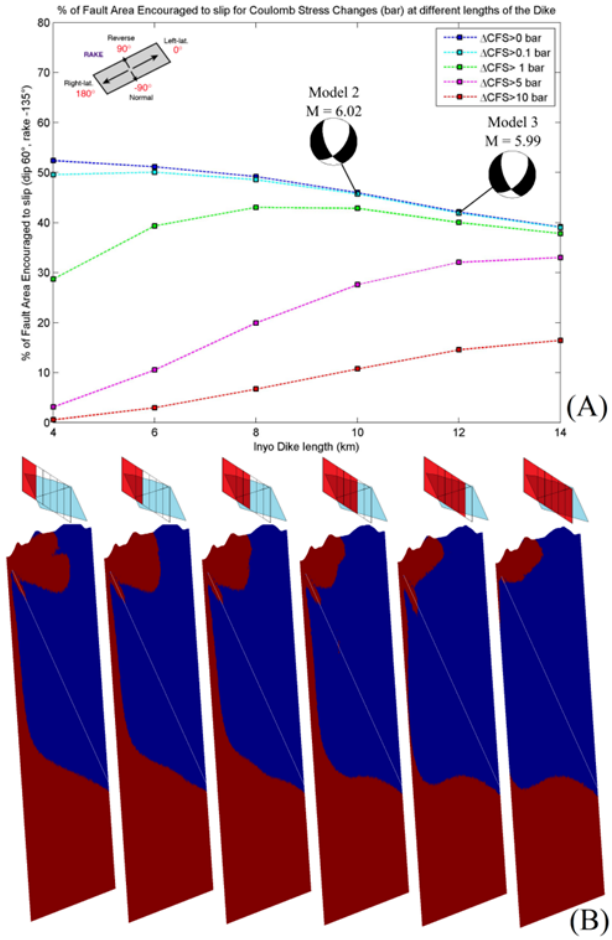

Fig. 4.: Analysis of Coulomb stress changes: percentage of fault area encouraged from a dike intrusion for different lengths of the dike; (B) distribution of Coulomb stress changes (ΔCFS $>$ 0.1 bar) on the fault plane for different lengths of the dike (red for slip encouraged; blue for slip discouraged).

maximum tensile stress in correspondence of the Obsidian Flow and Glass Creek domes (Figure 5 A,C). When the dike is near Glass Creek (dike 12 km-long) a slip along the fault can increase the maximum tensile stress nearby this dome (Figure 5 B,D).

Conclusions

The quasi-static analysis of the Coulomb stress change indicates that the opening of the Inyo Dike could enable right-lateral and oblique-slip motions along the Hartley Springs Fault. In particular, slip along the fault is facilitated when the dike is approaching the fault near Obsidian Flow dome. However, the opening of the dike does not promote slip along the fault when it reaches the south tip of the Hartley Springs Fault. The analysis of stress changes along the dike surface indicates that slip along the HSF could increase the local maximum tensile stresses facilitating the opening of the Inyo dike. Furthermore, the increase in tensile stress at the top of the dike indicates local conditions promoting the propagation of the dike toward the surface, especially near the southern tip of the fault, close to the Obsidian Flow and Glass Creek Flow domes.

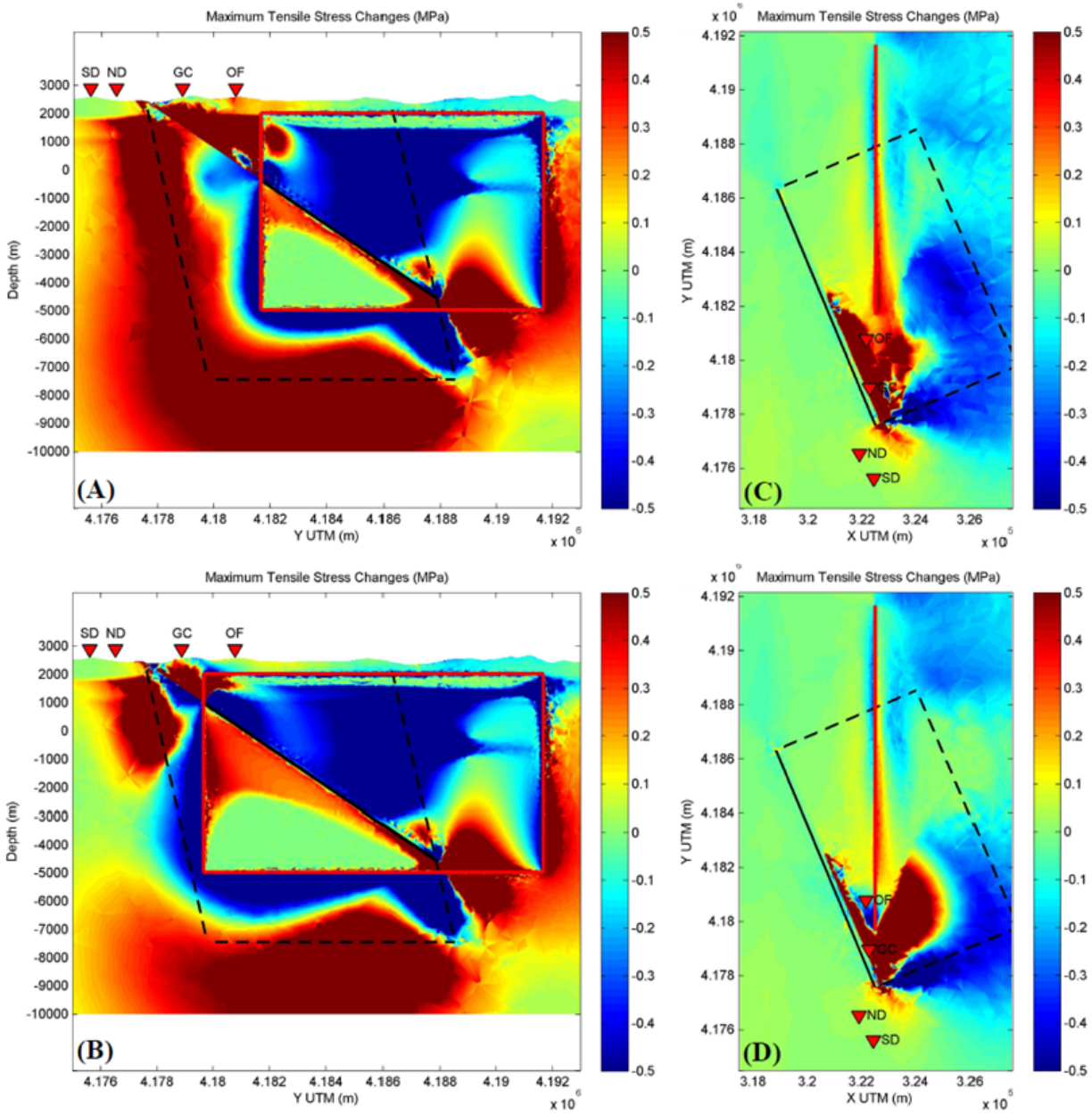

Fig. 5.: Maximum Tensile stress changes (MPa) triggered by earthquakes along Hartley Springs Fault: slice parallel to the dike (YZ plane) for Model 2 (A) with a dike 10 km long and Model 3 (B) with a dike 12 km long; slice on the top of dike (XY plane) for Model 2 (C) and Model 3 (D); red triangles indicates the position of the craters (OF = Obsidian Flow; GC = Glass Creek Flow; ND = North Deadman Dome; SD = South Deadman Flow); solid black line indicate the superficial trace of the Harley Springs Fault, dashed black line indicate the deep position of the fault; solid red line indicate the trace of the Inyo Dike.

Modeling of Cooling History for the Jurassic Composite Granitic Plutons in the Central Nanling Region, South China: Implications for the Mineralization Process and Tectonic Evolution

Huan LI[1], Koichiro WATANABE [1], Kotaro YONEZU[1]

[1] *Department of Earth Resources Engineering, Faculty of Engineering, Kyushu University, Fukuoka 819-0395, Japan*
e-mail: *li-huan@mine.kyushu-u.ac.jp*
session: *Volcanism and Volcanotectonics*

Introduction

The southern part of China (South China) is an excellent natural laboratory for studying intra-continental geological processes. The intra-continental magmatism in the South China is characterized by huge volumes of Phanerozoic granitoids, which indicate a widespread, episodic crustal reworking.

The Nanling region in the central part of South China is a most unique and very important W, Sn, Mo, Bi, Pb, Zn, Cu, REE, and U metallogenic belt in the world (Chen et al., 2002; Hsieh et al., 2008; Fig.1a). It occupied more than 60% and about 20% of the world's total W and Sn reserves, respectively, formed within a short period which is known as the Early Yanshanian period (aged at 190–140 Ma, between the middle to late Jurassic periods) (Shu et al., 2011). The former explorers and researchers have investigated lots of representative granites and mineral deposits of this area, and gained abundant information. The Early Yanshanian magma activity is frequent and is characterized by multiple stages and multiple intrusions, resulting in lots of granite composite and related resources (Fig.1b). Although the mineralization is widely known to be associated with the Yanshanian intrusions, the genetic relationships with the granitic exhumation and cooling of the plutons remain poorly understood. Discrepancies among various U–Pb ages and younger age determinations based on Rb–Sr, Ar–Ar and K–Ar isotopic systems from granitoids of the Nanling region have raised questions about the timing of the most related mineralization of these rocks and the details of their cooling path. In this study, we systematically collected a wide variety of dating data of some Early Yanshanian granitic intrusions in the central Nanling region, and based on the different types of age results given by different minerals with different closure temperature, we try to rebuild the cooling history and calculate the exhumation process for each representative granite composite, and hopefully to give some insight to the granite related mineralization and the tectonic evolution in this area.

Data collection and cooling–exhumation calculations

In this study, published zircon U–Pb, whole rock Rb–Sr, and muscovite, biotite and K-feldspar K–Ar or Ar–Ar age data for the different intrusive stages of the respective granite composites in the central Nanling region were systematically collected. These age data was deliberately screened, and the unreliable data was removed. Here, we assumed that the closure temperature of zircon, Rb–Sr whole rock, muscovite, biotite and K-feldspar are 800°C, 600°C, 350°C, 300°C and 150°C, respectively.

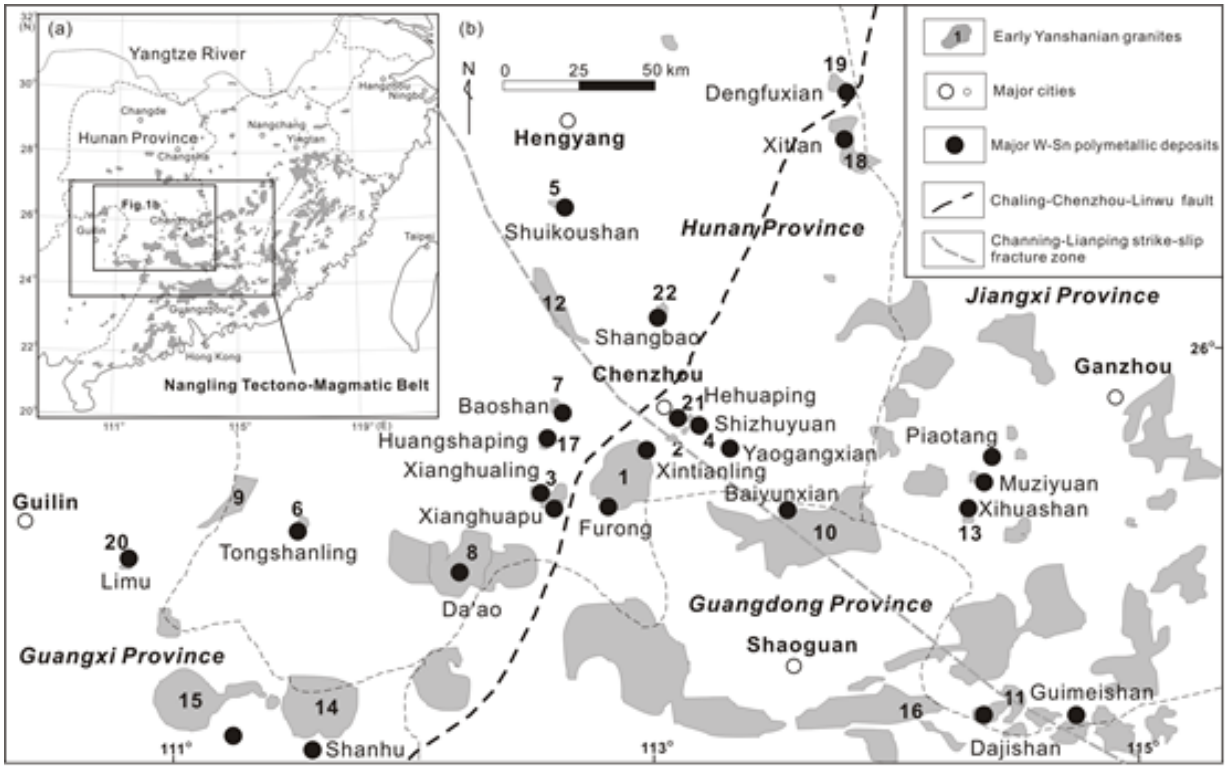

Fig. 1.: Distribution of Early Yanshanian granite composite and related ore deposits in (a) South China and (b) central Nanling region (modified from Yu, 2011). Granite composites: 1=Qitianling, 2=Qianlishan, 3=Xianghualing, 4=Yaogangxian, 5=Shuikoushan, 6=Tongshanling, 7=Baoshan, 8=Jinjiling, 9=Dupangling (eastern pluton), 10=Zhuguangshan, 11=Dajishan, 12=Dayishan, 13=Xihuashan, 14=Guposhan, 15=Huashan, 16=Guidong, 17=Huangshaping, 18=Xitian, 19=Dengfuxian, 20=Limu, 21=Wangxianling-Hehuaping, 22=Shangbao

Based on the above reliable age determinations and estimates of closure temperature, estimates have been done for the cooling rates of the composites in the Nanling Region. Fig. 2 shows a reconstruction of the cooling rates of these granite composites. Based on the modelling results we can conclude that the cooling paths of the first stages of these granites are steepest (e.g., BS1, ZGS1, and TSL1), indicating the fastest cooling processes. On the contrary, the cooling paths of the followed intrusive stages gradually become more flat, suggesting increasingly slower cooling history. For the purpose of computing the cooling path, we consider that the first stages of these composite cooled from 800°C to 300°C within a very short time span of 5 Ma. The followed subsequently second stages experienced a time span of 15 Ma from 800°C to 150°C. Collectively, the temperatures go down from 800°C to 150°C for the third stages may spend a time span of around 40 Ma, and 50 millions of years could be taken for the final stages of these granites to cool them down from 800°C to 300°C. The average cooling rates of the first stages are about 100°C Ma^{-1}, and the second, the third and the fourth are around 45°C Ma^{-1}, 15°C Ma^{-1}, and 10°C Ma^{-1}, respectively. In short, compared to the granites in other areas, the cooling rates of these granite composites in the central Nanling region are markedly fast, especially for the first two stages.

If we assume that the temperatures maintained by granitic intrusions are mainly affected by the geothermal gradients which are corresponded to different burial depths, we can calculate the uplift rates based on the cooling rates of the granites in the central Nanling region. We assume the geothermal gradient in the central Nanling region

was 50 °C km^{-1}. Accordingly, we calculate that the uplift rates of the first stages of the granite composites are the fastest, with the value of $\sim$ 2 mm y^{-1}, followed by 0.9, 0.3, and 0.2 mm y^{-1} for the rest stages, respectively. Active denudation and erosion was due to ongoing tectonic uplift of the area by thrusting and thickening of the crust.

Mineralization implications

The most famous peak episode of Mesozoic large-scale magmatism and associated ore formation in South China is 170–150 Ma. Mineralization of the 170–160 Ma age range is mostly of porphyry and skarn type (Cu–Au) and of granite-related vein type (Pb–Zn–Ag), while the 160–150 Ma age range is characterized by granite-related W–Sn polymetallic mineralization (Li et al., 2012). According to this study, the 170–160 Ma Cu–Pb–Zn mineralization was related to the earlier round quick ascended magmas, whereas the later 160–150 Ma W–Sn polymetallic mineralization was resulted from the slower cooling and ascending plutons.

Different ascent rates and evolutionary process of the magmas and intrusions caused the different mineralization related intrusions. If the intrusions ascend slowly, the crystal fractionation as well as upper crustal contamination and assimilation would have enough time to occur. W, Sn, Bi, Mo, As, and Sb become more enriched during fractionation compared to the base metals Zn, Pb, and Cu (Mustard et al., 2006). The rift-related rapid extension of the crust caused deep Cu source evoked and generated in a low-pressure environment, while the extreme crystal fractionation aided by high volatile activity, coupled with crustal contamination and assimilation under a relatively stable settings produced the W–Sn polymetallic mineralization in the central Nanling region.

Mantle plume-generated triple junction rifts: A new model

Intraplate lithospheric thickening events rather than the subduction of the Pacific plate was proposed for Nanling region (Shu et al., 2011). Based on the distribution of major W–Sn polymetallic deposits and deep faults in the central Nanling region and the calculations of the cooling and uplift rates, we proposed a new model for this region during the early Yanshanina period: mantle plume generated triple junction rifts (Fig. 3). This triple junction rift system was centered by the Qiantianling granite composite and composed of three major cross arms which extended to the NE, SW, and SE directions, respectively, and the extension length for each arm was more than 200 km. the NE and SW arms extended basically along the Chaling–Chenzhou–Linwu deep fault, while the SE arm mostly overlapped with the Channing–Lianping strike-slip fracture zone. The basic supports for this model come from the following two points: 1), the distribution of the granite associated deposits. Fig.1b shows that large scale deposits are concentrated and surrounded in the Qitianling area, and diverging to three different opposite directions which reach at the Denghuxian–Xitian deposit, the Shanhu deposit, and the Xihuashan–Dajishan deposit, respectively. In the Qitianling area where the mantle plume lies below, Cu, Pb, and Zn are also largely outputted besides W-Sn mineralization (Fig. 3). 2), the differences in the cooling and uplift rates. Most of the granite composites located in the Qitianling area have very quick cooling and uplift rates, especially for their first stage of their intrusive activities. On the contrary, far away from the center, granite composites such as the Guposhan, the Huashan, the Dajishan, and the Dengfuxian have much slower cooling and uplift rates. They may be formed by more highly evolved magma and have more discernable intrusive stages. In our model of mantle plume generated triple junction rifts system, the mantle plume started its activities at the beginning of the early Yanshanina period, causing large amount of

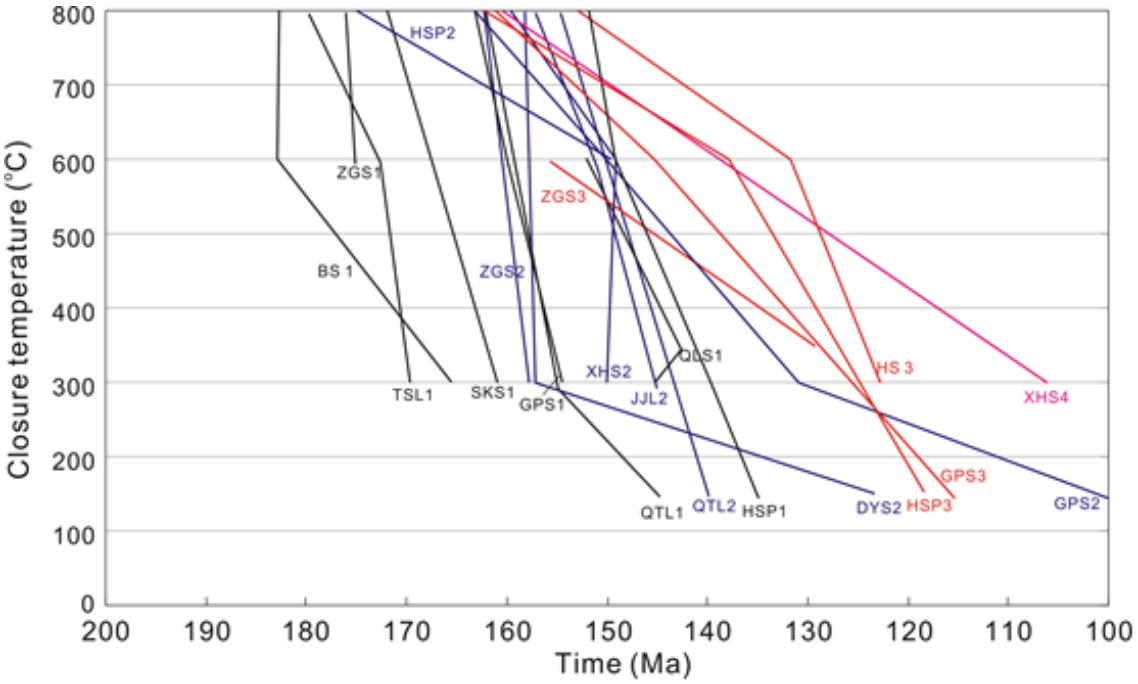

Fig. 2.: Cooling paths of some representative granite composite in the central Nanling region. Granite composites: BS = Baoshan, ZGS = Zhuguangshan, TSL = Tongshanling, SKS = Shuikoushan, GPS = Guposhan, QTL = Qitianling, QLS = Qianlishan, HSP = Huangshaping, XHS = Xihuashan, DYS = Dayishan, HS = Huashan. The figures followed by each granite composite represent the intrusive stage.

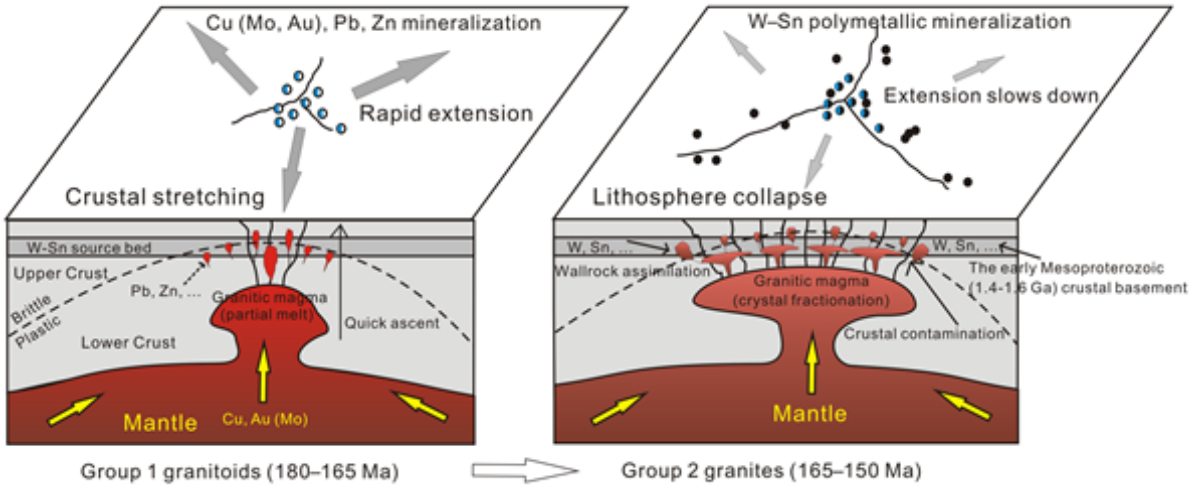

Fig. 3.: A model of mantle plume generated triple junction rifts for the central Nanling region during the 180–150 Ma period.

magma activities and resulting in the most of the earlier stages of the intrusions of the granite composites. During this period (180–165 Ma), triple junction rift activity was generated by the mantle plume and lasted effectively for a short period of time. The intrusions ascended very quickly and cooled down fast, and also brought some Cu, Pb and Zn base mental mineralization, forming

the major parts of the Baoshan, the Shuikoushan, the Huangshaping and the Shangbao deposits. After this period, the extension activity slowed down (165–150 Ma), and the following magmatisms have more time to extract more ore-forming elements from the upper crust by contamination and assimilation, resulting in the world-famous Nanling W–Sn mineralization belt (Fig. 3).

References

Chen, P.R., Hua, R.M., Zhang, B.T., Lu, J.J., and Fan, C.F., 2002. Early Yanshanian post-orogenic granitoids in the Nanling region–Petrological constraints and geodynamic settings. Science in China Series D: Earth Sciences, 45, 755–768.

Hsieh, P. S., Chen, C. H., Yang, H. J., and Lee, C.Y., 2008. Petrogenesis of the Nanling Mountains granites from South China: Constraints from systematic apatite geochemistry and whole-rock geochemical and Sr–Nd isotope compositions. Journal of Asian Earth Sciences, 33, 28–451.

Li, C.Y., Zhang, H., Wang, F.Y., Liu, J.Q., Sun, Y.L., Hao, X.L., Li, Y.L., and Sun, W.D., 2012. The formation of the Dabaoshan porphyry molybdenum deposit induced by slab rollback, Lithos, 150, 101–110.

Mustard, R., Ulrich,T., Kamenetsky, V. S., and Mernagh, T., 2006. Gold and metal enrichment in natural granitic melts during fractional crystallization. Geology, 34, 85–88.

Shu, X.J., Wang, X.L., Sun, T., Xu X.S., and Dai, M.N., 2011. Trace elements, U–Pb ages and Hf isotopes of zircons from Mesozoic granites in the western Nanling Range, South China: Implications for petrogenesis and W–Sn mineralization. Lithos, 127, 468–482.

Yu, C.W., 2011. The characteristic target-pattern regional ore zonality of the Nanling region, China (I). Geoscience Frontiers, 2, 147–156.

The gravitational unloading due to rift depression: A mechanism for the formation of off-rift volcanoes in (continental) rift zones

Francesco Maccaferri[1], Eleonora Rivalta[1], Derek Keir[2], Valerio Acocella[3]

[1] *GeoForschungsZentrum Potsdam, Section 2.1, Telegrafenberg, 14467, Potsdam, Germany*
[2] *National Oceanography Centre Southampton, University of Southampton, Southampton, SO14 3ZH, UK*
[3] *Dipartimento Scienze, University of Roma Tre, L. S.L. Murialdo, 1, 00146, Roma, Italy.*
e-mail: *francesco.maccaferri@gfz.potsdam.de*
session: *Volcanism and Volcanotectonics*

Introduction

Rift valleys are the surface expression of prolonged extension of the continents. During rift initiation, the lithosphere thins by ductile stretching and normal faulting, creating a rift valley [1]. The upwelling asthenosphere melts by adiabatic decompression, with the greatest degree of partial melting beneath the most thinned part of the crust [2,3]. Melt can accumulate at the brittle-ductile transition, in magmatic reservoirs centred on the rift axis. Crustal stretching and melt production underneath the rift axis, often result in the formation of volcanoes within the rift valley, as observed, for instance, in the North Volcanic Zone of Iceland. A not trivial but relatively common observation in continental rift zones, is the occurrence of off-rift volcanism [4,5,6]: which is the presence of volcanoes located out of the rift border faults, displaced up to tens of kilometres outside the rift valley (Fig. 1). Off-rift volcanoes and off-rift volcanic provences are generally aligned, parallel to the rift axis, and they are often associated with early rifting [4,5]. In the Red Sea Rift, ∼25 Ma-old rift-parallel dykes focus near the ∼30 Ma-old rift margins, while the youngest volcanoes focus along the ridge axis [7]. Even in far less magmatically active settings, such as the Baikal Rift (Siberia) or the Chaine des Puys (CdP) in the Cenozoic rift system of France, off-rift volcanism occurred after the onset of rifting. The mechanism driving magma from deep rift-centred magma reservoirs to feed off-rift volcanic systems is still debated.

Methodology

We used a numerical (boundary element) model to simulate the propagation of magmatic dykes [8,9,10] starting from a deep magmatic reservoir located at the base of the crust, and centred on the rift axis. Our model gives as output the expected location of volcanism at surface, as well as the path followed by dykes before getting arrested within the crust or arriving at surface.

A fundamental input for our model is the stress field within the crust, since dykes tend to orient perpendicular to the direction of the minimum compressive stress ($\sigma 3$). We model the stress field in the rift setting accounting for:

1. the lithostatic pressure;
2. the tectonic stress;
3. the mechanical effect due to the gravitational unloading (decompression) induced by the mass deficit at the rift valley.

The resulting stress field in the crust is the superposition of 1, 2 and 3. Where 1 is assumed

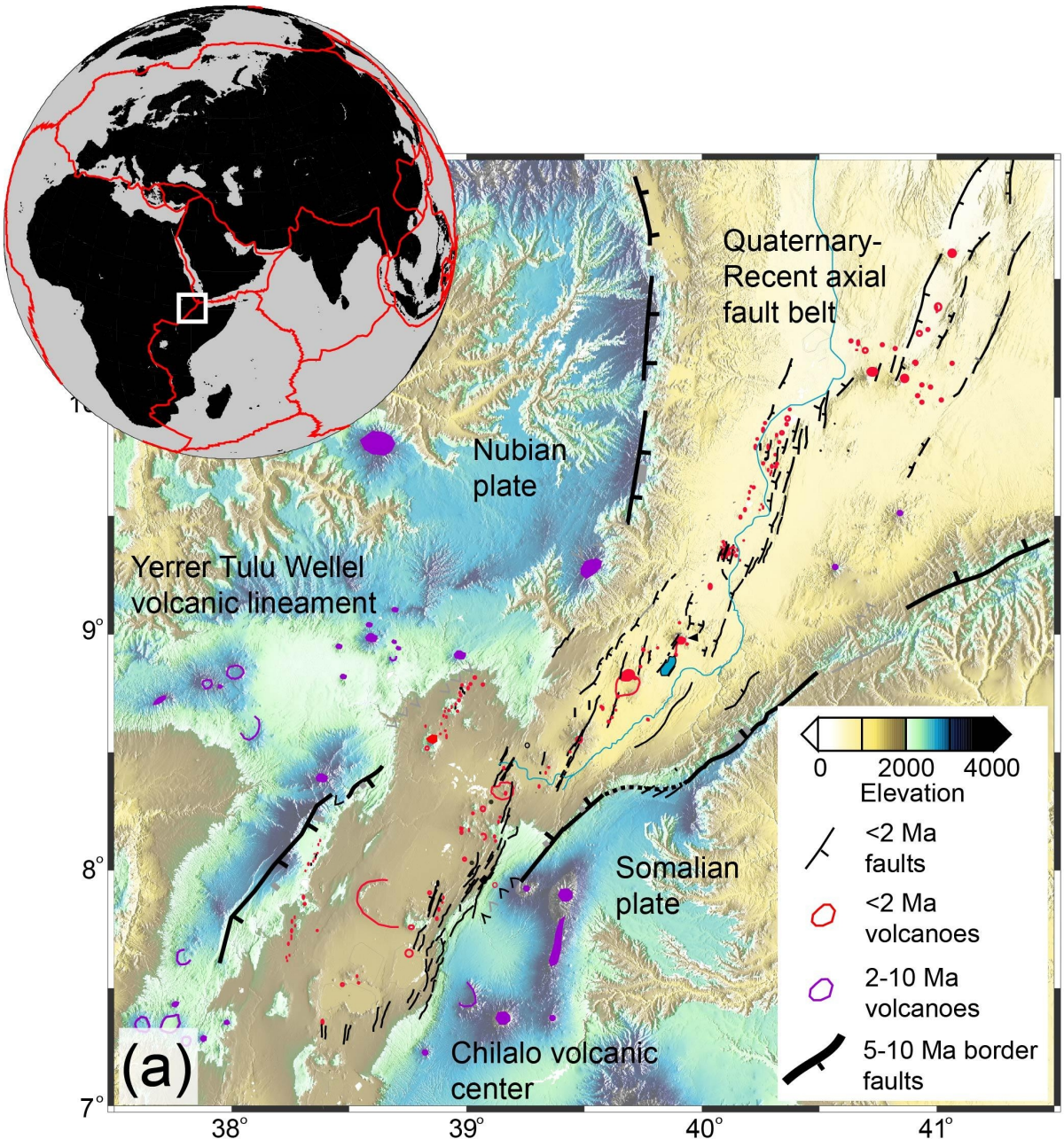

Fig. 1.: Topographic, structural and volcanic architecture of the Main Ethiopian Rift. Miocene border faults are thick black lines with direction of down throw indicated and the Quaternary-Recent faults within the rift are thin black lines. Early syn-rift volcanic edifices are purple and Quaternary-Recent volcanoes and cones are red. Note that the early syn-rift volcanism ranges from being just outboard of the Miocene border faults, to as far as 100 km from the rift valley. (Figure from [13])

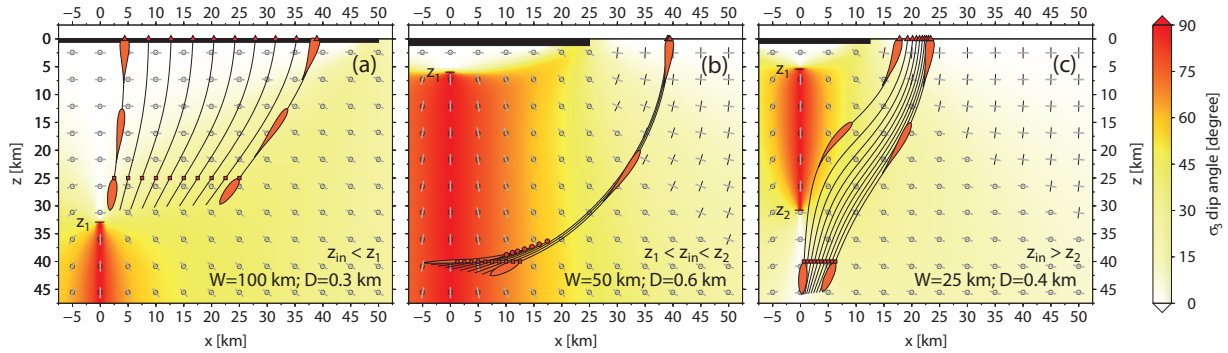

Fig. 2.: Dyke trajectories for scenarios A, B, and C. Red squares indicate the upper tip of the dyke at injection, red circles indicate that a dyke has been arrested as sill; red triangles indicate the position of the arrival at surface. Black and gray segments show the directions of $\sigma 1$ and $\sigma 3$ respectively (a circle indicates direction perpendicular to the page) for three nominal sets of graben width, W, and depth, D, (see insets). The dip angle of $\sigma 3$ is color-shaded: where sub-vertical (reddish color), a stress barrier to vertical ascent of dykes is acting. The stress barrier is expected to dissipate in a weak lower crust or mantle. (Figure from [13])

to be isotropic and therefore does not contribute to the orientation of the principal stress; 2 is the horizontal tension due to crustal stretching (assumed to be in the range of 5 to 10 MPa) and tend to favour the horizontal orientation of $\sigma 3$; 3 can be computed with the analytical formulas by [11].

Results

The contribution of gravitational unloading is the essential component in our study. When the gravitational unloading dominates over the tectonic stretching, $\sigma 3$ becomes vertical in a confined volume beneath the rift. This volume constitutes a sort of "stress barrier zone", in which stacked sills are favoured, and which deflects the ascending dykes to the rift sides. Sideways from the rift centre, $\sigma 3$ becomes first inward dipping and then horizontal (Fig. 2).

Depending on where the dykes nucleate relative to the stress barrier zone, three scenarios for their propagation and for the final surface distribution of magmatism occur:

A *If dykes start above the stress barrier* (or if the theoretical location of the stress barrier is deeper than the crustal thickness) in-rift volcanism occurs. Magma-filled dykes ascend subvertically, or propagate laterally within the rift parallel to the axis (Fig. 2a), and the dyke arrivals are spread within the graben.

B *If dykes start within the stress barrier* (or the stress barrier extends across the crust and extends until the brittle-ductile transition), our model predicts off-rift volcanism with sill formation. The injected magma at the base of the crust forms sub-horizontal magmatic sheets that, depending on their initial distance from the rift axis, get trapped as stacked sills above the ponding zone or escape to the side of the stress barrier, turning into subvertical dykes and eventually reaching the surface (Fig. 2b). For a given set of parameters, dykes emerge very tightly spaced at a distance from the rift axis equal to about 1 to 2 (and up to 3) graben half-widths.

C *If dyke starts underneath the stress barrier*, off-rift volcanism occurs without sill formation: vertical dykes are deflected towards the rift sides, with a more scattered arrival distribution at the surface (Fig 2c). This occurs with deep nucleation depths below shallow and narrow grabens, and is the least likely configuration for a reasonable range of values for graben depths and widths and crustal thickness.

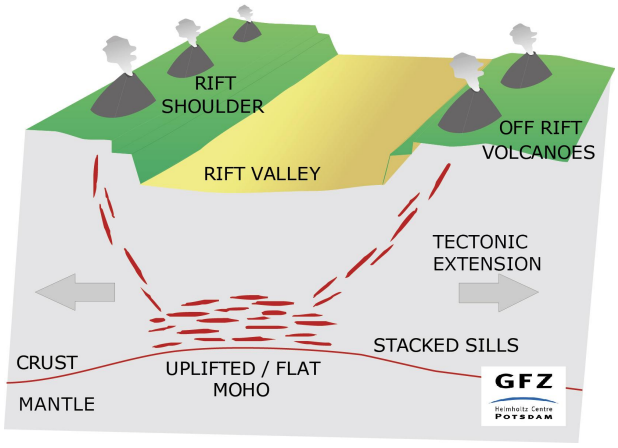

Fig. 3.: Summary cartoon illustrating the magma paths behind off-rift volcanism.

Conclusions

For deep grabens the upper limit of the stress barrier (z1) is shallow (z1∼10 km for a 100 km wide and 1 km deep graben) so that in-rift arrivals occur only for shallow nucleation depths. For a nucleation depth in the range of 30 - 40 km, which represent a reasonable estimate for the crustal thickness at the early stage of continental rifting, in-rift volcanism occurs only for wide (>100 km) and shallow (<0.6 km) rift depressions, or for graben depths which are too small to create a stress barrier (i.e. the tectonic stretching dominates over the gravitational unloading). A thinner crust thickness or the presence of shallower reservoirs, result in favouring "in-rift volcanism", as expected for the North Volcanic Zone of Iceland (NVZ) or for Quaternary volcanism in the MER.

According to our findings, the most likely configuration for the early stages of continental rifting is scenario B. This may result in the construction of large off-rift volcanoes aligned parallel to the rift. Also, for this scenario, our model predict that magmatic intrusion will get easily trapped as stacked sills underneath the rift axis, above the Moho (Fig. 2b and Fig. 3). Recent results from seismic tomography at Baikal rift suggest that a deep, rift centred reservoir, at Moho depths, formed by means of staked sills [12].

As the rift matures, the magma ponding zone near the base of the crust becomes progressively shallower due to crustal thinning and to sills piling one above the other and functioning as new, shallower reservoirs, driving the system towards the condition of case A and to a transition to in-rift volcanism.

References

1. McKenzie, D. Some remarks on the development of sedimentary basins. Earth Planet. Sci. Lett. 40, 25-32 (1978).

2. Lubimova, E. A. Heat flow patterns from Baikal and other rift zones. Tectonophysics 8, 457-467 (1969).

3. Bown, J. W. & White, R. S. Effect of finite extension rate on melt generation at rifted continental margins. J. Geophys. Res. 100, 18011-18029 (1995).

4. Ellis, M. & King, G. Structural control of flank volcanism in continental rifts. Science 254, 839-842 (1991).

5. Morton, W. H., Mitchell, J. G., Rex, D. C. & Mohr, P. Riftward younging of volcanic units in the Addis-Ababa region, Ethiopian rift valley. Nature 280, 284-288 (1979).

6. Kiselev, A. I. Volcanism of the Baikal rift zone. Tectonophysics 143, 235-244 (1987).

7. Bosworth, W., Huchon, P. & McClay, K. The Red Sea and Gulf of Aden Basins. J. African Earth Sci. 43, 334-378 (2005).

8. Dahm, T. Numerical simulations of the propagation path and the arrest of fluid-filled fractures in the Earth. Geophys. J. Int. 141, 623-638 (2000).

9. Maccaferri, F., Bonafede, M. & Rivalta, E. A numerical model of dike propagation in layered elastic media. Geophys. J. Int., vol. 180, pp. 1107-1123 (2010)

10. Maccaferri, F., Bonafede, M. & Rivalta, E. A quantitative study of the mechanisms governing dike propagation, dike arrest and sill formation. J. Volcanol. Geotherm. Res. 208, 39-50 (2011).

11. Davis, R. & Selvadurai, A. Elasticity and Geomechanics (Cambridge Univ. Press, Cambridge, 1996).

12. Thybo, H. & Nielsen, C. A. Magma-compensated crustal thinning in continental rift zones. Nature. 457, 873-876 (2009).

13. Maccaferri, F., Rivalta, E., Keir, D., Acocella, V., Off-rift volcanism in rift zones determined by crustal unloading Nature Geosci., vol 7, pp. 297-300, doi: 10.1038/ngeo2110.

The formation of terrace-bounding faults on Olympus Mons volcano, Mars

S. Musiol[1], B. Cailleau[2], E. P. Holohan[3], T. R. Walter[3], D. A. Williams[4], A. Dumke[1], S. van Gasselt[1]

[1]*Freie Universität Berlin Planetary Sciences and Remote Sensing*
[2]*Freie Universität Berlin, Institute of Geological Sciences, Geophysics, Berlin, Germany*
[3]*Helmholtz-Zentrum Potsdam, Deutsches Geoforschungszentrum, Sektion Erdbeben- und Vulkanphysik, Potsdam, Germany*
[4]*Arizona State University, School of Earth and Space Exploration, Planetary Geology Group, Tempe, AZ, USA*
e-mail: *stefanie.musiol@fu-berlin.de*
session: *Volcanism and Volcanotectonics*

Introduction and Background

Olympus Mons volcano is located in the northern hemisphere of Mars, west of the Tharsis volcanic province. It is a basaltic shield volcano with a height of 22 km, a diameter of 600 km, and an average flank slope of 5° (Plescia 2004). The main features of Olympus Mons include a summit caldera complex, upper- to mid-flank terraces, lower-flank radial scarps, and a basal circumferential scarp up to 9 km high with a slope of about 30°.

The morpho-structural map of Olympus Mons below (Fig. 1) shows radial scarps and mesas, as well as circumferential graben and troughs on the lower flanks that were previously interpreted as extensional features, probably due to volcanic spreading (e.g., Morris and Tanaka 1994, Borgia et al. 2000, McGovern and Morgan 2009). On the other hand, the terraces on the upper flanks were interpreted as compressional features due to lithospheric flexure (McGovern and Solomon 1993, Byrne et al. 2009, 2013). Lithospheric flexure is observed from a prominent trough around Olympus Mons that is filled by lava (Isherwood 2013).

Since the asthenospheric mantle behaves like a fluid on long timescales, the overlying elastic lithosphere bends due to volcanic loading. A flexural trough forms around the volcano and a bulge forms further outside the trough. This flexure leads to a lateral compression of the volcano and a lateral extension of the upper lithosphere peripheral to the volcano (e.g., Comer 1983, Watts 2001). Spreading affects the volcano when a basal layer or interface characterized by low friction decouples the volcano from the lithosphere, such that the volcano can slide over the lithosphere during flexure (e.g., Byrne et al. 2013).

The aim of our work is to understand terrace development over time, and the relation of terraces and flank instability to volcano growth, lithospheric flexure, and volcanic spreading (i.e. basal decoupling).

Finite Element Modeling

The deformation of a volcanic cone under Martian gravity was investigated with finite element models that take into account the combined effects of lithospheric flexure and volcanic spreading. The axisymmetric setup consists of three parts: an elastoplastic volcano and lithosphere overlying a viscoelastic asthenospheric mantle. Spreading was realized by means of a frictional interface

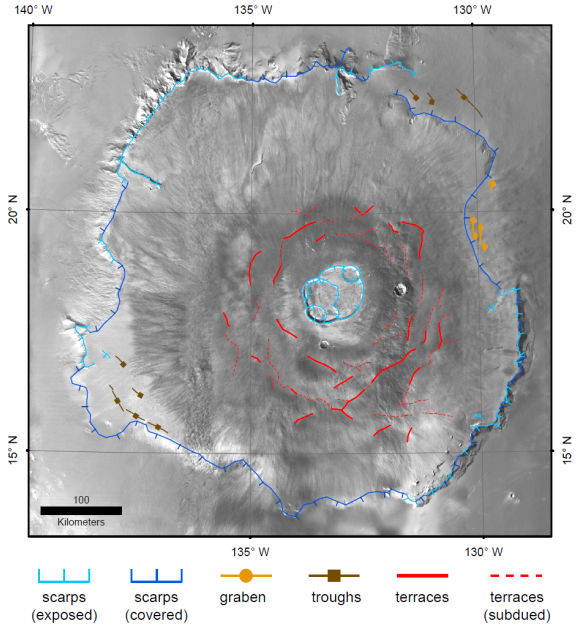

Fig. 1.: Mapping results. Structural mapping of Olympus Mons based on a High Resolution Stereo Camera (HRSC) slope map, and on Thermal Emission Imaging System (THEMIS) daytime data.

between volcano and lithosphere. The interface's coefficient of friction was varied between 0 and 0.6 and in addition, a welded contact was investigated. The cohesion of the volcano was varied between 6 and 60 MPa (basaltic rock mass vs. laboratory-measured basaltic sample, according to Schultz 1995).

We simulated two cases of loading: (1) an instantaneously-emplaced volcano and (2) an incrementally grown volcano. For the latter, the volcano was constructed by successively adding five parts of equal volume, and viscous relaxation of the asthenospheric mantle was allowed between the five loading steps. After emplacement of a volcano load, the lithosphere and asthenospheric mantle behave elastically in the beginning. As the asthenospheric mantle relaxes and becomes increasingly viscous, the volcano and lithosphere develop plastic deformation. Isostatic equilibrium of the load and mantle is reached after about 500,000 years. Further model details can be found in Musiol (2013).

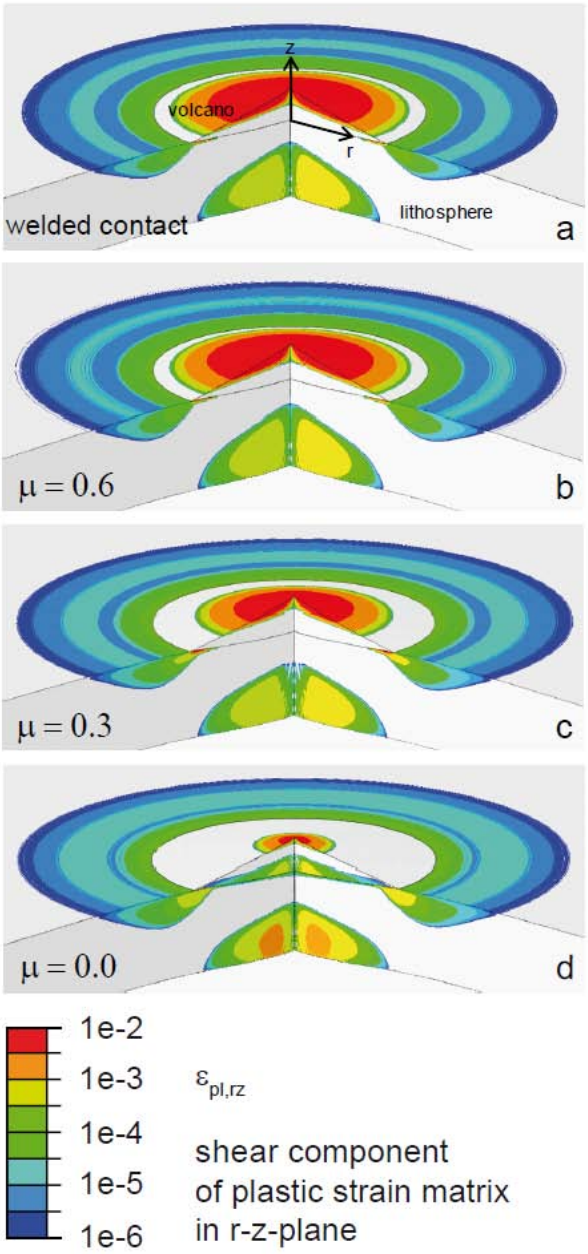

Fig. 2.: Plastic shear strains at the end of isostatic adjustment within models of instantaneous volcano emplacement and varying basal friction. Shown here are cut-away, vertically-exaggerated views of: a) a model with welded contact; b-d) models with decreasing coefficient of friction on the edifice-lithosphere interface. Note the migration of the zone of high plastic strain on the edifice flanks toward the summit with decreasing friction, and an increasingly large plastic strain zone at the interface of volcano and lithosphere.

Results

We show the model results for the instantaneous volcanic load as accumulated plastic shear strains in the axisymmetric plane (Fig. 2). Highest shear strain denotes potential faulting, which is observed on the volcano flanks and at the interface of volcano and lithosphere. With decreasing friction at the interface of volcano and lithosphere, the zone of plastic deformation on the flanks migrates toward the summit area and the zone of basal overthrusting increases. Terrace-bounding faults can be seen at high resolution and are compatible with radial compression leading to thrust faulting on the volcano flanks.

In the models with a growing load, and regardless of cohesion, the areas of observed faulting for the first increment are in agreement with the instantaneous model. As more layers are added, no further plastic straining of the volcano flanks is observed with high cohesion, but plastic strain zones corresponding to terrace-related faulting were produced on every incrementally-formed volcano surface with low cohesion.

Conclusions

Terrace-bounding faults on Olympus Mons upper flanks are explained with thrust faulting resulting from lithospheric flexure. The presence and expression of terrace-bounding faults depends on the coupling of volcano and lithosphere, on the time of volcano growth relative to mantle relaxation, and on the edifice cohesion.

References

Borgia, A., P. T. Delaney, and R. P. Denlinger (2000), Spreading volcanoes, Annu. Rev. Earth Pl. Sci., 28, 539-570.

Byrne, P. K., B. van Wyk de Vries, J. B. Murray, and V. R. Troll (2009), The geometry of volcano flank terraces on Mars, Earth Planet. Sci. Lett., 281, 1-13, doi:10.1016/j.epsl.2009.01.043.

Byrne, P. K., E. P. Holohan, M. Kervyn, B. van Wyk de Vries, V. R. Troll, and J. B. Murray (2013), A sagging-spreading continuum of large volcano structure, Geology, 2013090, doi: 10.1130/G33990.1.

Comer, R. P. (1983), Thick plate flexure, Geophys. J. R. astr. Soc., 72, 101-113.

Isherwood, R. J., L. M. Jozwiak, J. C. Jansen, J. C. Andrews-Hanna (2013), The volcanic history of Olympus Mons from paleotopography and flexural modeling, Earth and Planet. Sci. Lett., 363, 88-96, doi: 10.1016/j.epsl.2012.12.020.

McGovern, P. J., and J. K. Morgan (2009), Volcanic spreading and lateral variations in the structure of Olympus Mons, Mars, Geology, 37, 139-142.

McGovern, P. J., and S. C. Solomon (1993), State of stress, faulting, and eruption characteristics of large volcanoes on Mars, J. Geophys. Res., 98, 23,553-23,579, doi:10.1029/93JE03093.

Morris, E. C., and K. L. Tanaka (1994), Atlas of Mars: Olympus Mons Region, Geol. Inv. Series I-2327, U. S. Geological Survey, Denver.

Musiol, S. (2013), Geodynamics of the Volcanoes Hadriaca Patera and Olympus Mons on Mars, Ph.D. Thesis, Fachbereich Geowissenschaften, Freie Universität Berlin.

Plescia, J. B. (2004), Morphometric properties of Martian volcanoes, J. Geophys. Res., 109, E03003, doi:10.1029/2002JE002031.

Schultz, R. A. (1995), Limits on strength and deformation properties of jointed basaltic rock masses, Rock Mech. Rock Engng., 28, 1-15.

Watts, A. B. (2001), Isostasy and Flexure of the Lithosphere, 1st ed., 458 pp., Cambridge Univ. Press, Cambridge.

Surface deformation simulations of volcanic and tectonic processes in Iceland

Rikke Pedersen[1]

[1]*Nordic Volcanological Center, Institute of Earth Sciences, University of Iceland, Iceland.*
e-mail: *rikke@hi.is*
session: *Volcanism and Volcanotectonics*

Spatially and temporally dense observations of crustal deformation events is an important data source when trying through numerical modeling to obtain insight into geological processes working at depth, for instance by visualization of magma transport and emplacement beneath volcanic structures, as well as simulations of tectonic processes within plate boundary zones. Iceland is an excellent target for remote sensing of crustal deformation processes, especially for the use of interferometric combination of synthetic aperture radar images (InSAR). The Icelandic crust deform continuously due to a variety of volcanic and tectonic processes, and the relatively barren ground furthermore makes an ideal reflector for radar beams emitted from SAR satellites. Three recent Icelandic examples of crustal deformation events related to active plate spreading processes and subsurface magma movements, and the inferences numerical modeling facilitate, will here be demonstrated.

1

The Northern Volcanic Zone (NVZ) is an extensional rift segment, forming a sub-aerial exposure of a part of the mid-Atlantic ridge. The NVZ is bounded to the south by the Icelandic mantle plume, and to the north by the Tjörnes transform zone. The NVZ has typically been divided into five partly overlapping en-echelon fissure swarms, each with a central main volcanic production area. A complex interplay of a number of tectonic and magmatic processes in the NVZ has been revealed by a series of InSAR images: A) two shallow sources experiencing subsidence coincides with known crustal magma chambers at Askja and Krafla central volcanoes, B) elongated subsidence signals within the relatively narrow fissure swarms (15-20 km), inferred to be related to plate spreading, C) horizontal plate spreading distributed over a much wider zone (∼80-100 km), and finally D) a wide area of uplift which may reflect on processes near the crust mantle boundary. Construction of finite element method (FEM) models of the NVZ, have facilitated exploration of the role spatial variation of rheological properties may play, in modifying the style of regional and local surface deformation at this extensional plate boundary. The models indicate that the observed inter-rifting plate spreading deformation field is controlled by local rheological variations within the arrangement of fissure segments, and that a regional central ridge axes model does not apply. The best fitting crustal structure within the most active fissure swarms consists of a wedge of weak elastic material on top of a local visco-elastic ridge.

The Askja system is one of the five *en echelon* volcanic systems making up the NVZ. It consists of a fissure system elongated along the plate boundary and a central complex of at least three nested calderas. The smallest, most recent caldera formed over an extended period of up to 40 years following a highly explosive eruption in 1875. The volcano has been somewhat of a geodetic enigma for many years, as continuous subsidence has been observed by dry-tilt level-

ing there since 1983, and possibly been ongoing since 1973. Seismic studies around Askja have provided new information on possible magma pathways from deep crustal levels, to inferred storage zones in the upper crust. FEM models, simulating surface deformation locally at the Askja volcano, indicates that the tectonic setting with an established shallow magma chamber situated within a diverging plate boundary plays a major role in the continuous, long-term high subsidence rates observed at Askja for the past 30-40 years. In order to fully understand the cause and effect of the complicated volcano-tectonic setting additional advanced models integrating realistic rheological subsurface structures are needed.

2

Since Iceland was settled in the 9th century Hekla volcano has had 23 confirmed eruptions, varying considerably from highly explosive (VEI 5) to calm effusive (VEI 1). Hekla produces mainly andesitic melts, though products range from basaltic to rhyolitic. The silica content is directly correlated to the repose interval, providing a strong argument for the presence of a well-established magma chamber. Numerous geophysical studies have attempted to determine the depth and location of the Hekla magma chamber, but results are as many as the number of studies. Several other characteristics of Hekla volcano make it unique in a global context. The ridge shaped edifice is highly unusual, and the dual nature of the seismicity is not only unusual but also poorly understood. In inter-eruptive periods the volcano is practically aseismic, and the few micro-earthquakes that do occur appear to be related to a nearby transform-zone, whereas co-eruptive earthquakes are clearly connected to magmatic movements. No earthquakes occur below 4 km depth before eruption onset, but during eruptions most are located at 4-9 km depth.

Since InSAR imaging have been applied, a highly improved map of the Hekla surface deformation has been achieved. The spatial density of deformation measurements obtained by this technique revealed a rather complicated surface deformation pattern, which more than one process is thought to contribute to. A roughly circular area 20 km in diameter (centered at the summit) subsides continuously during inter-eruptive periods. The subsidence peaks on the most recent lava flows, primarily due to cooling and compaction of the erupted material, although subsidence is not confined to areas covered by recent lava flows. A subtle, but continuous, uplift signal ($\sim$5 mm/yr) circumscribes the region of local subsidence. This uplift region has a diameter of $\sim$40 km (centered on the summit).

A relatively simple model capable of predicting the observed deformation pattern combines a contracting shallow magma chamber (local subsidence of the edifice), a deeper chamber that is expanding (regional uplift), and finally thermal contraction of recent lava fields. However, this model is problematic, because no independent evidence for a shallow magma chamber exists. An alternative model is here presented, where the composite pattern of deformation is attributed to local thermal contraction of recent lava fields combined with gravitational loading of the volcano edifice and finally magma accumulation at a deep-seated magma chamber. Finite element models where a gravitational load on a 2D problem domain having an elastic upper crust, underlain by a viscoelastic mantle that hosts magma accumulation within a deep-seated magma chamber have been explored.

3

Eyjafjallajökull volcano is situated south of the intersection between the South Iceland Seismic Zone and the Eastern Volcanic Zone (EVZ). The area is characterized by significant topographic relief and a lower spreading rate than the EVZ. As opposed to tholeiitic products in the axial rift zone further north, volcanic products here belong to the alkaline or transitional suite, and the area is, based on the petrological difference as well as poorly developed extensional fractures, characterized as a volcanic flank zone. Eyjafjallajökull is

an icecap covered stratovolcano rising to an elevation of 1666 m.a.s.l.. The icecap covers an area in the summit region about 80 km2 in size, making interferometric measurements unattainable within this area throughout the year. The volcano is characterized by its quiet nature. Activity in the system is episodic, with only four eruptions in the last 1400 years. About a handful of earthquakes associated with the volcanic system had been detected prior to the 1990s. Earthquake swarms did, however, occur in 1994, 1996, 1999 and finally in 2009-2010 preceding the eruption in the spring of 2010 which caused an exceptional, unprecedented disruption to European air traffic. Ground deformation measurements through the 18 years of intermittent unrest have facilitated a coarse mapping of the volcano's current plumbing system, through inverse modeling.

The typical pattern of surface deformation observed prior to, spanning and following eruptions of Iceland's frequently active volcanoes, often referred to as "the volcanic cycle", relates to melt accumulation, drainage and renewed replenishment from an established crustal magma chamber, which can be reproduced by pressure changes within a simple Mogi point source. However, such a simple modeling approach cannot explain the complex behavior observed at the moderately active Eyjafjallajökull volcano. Homogeneous elastic half-space modeling of a complicated network of sill intrusions forming at more than 5 km depth explains the distinct behavior of the volcano. The temporal development of the intrusive complex over the 18 years of intermittent unrest will be demonstrated.

Overburden bulking in analogue models of depletion-induced collapse quantified with computed X-ray micro-tomography

S. Poppe[1], E. P. Holohan[2], E. Pauwels[3], V. Cnudde[3,4], M. Kervyn[1]

[1] *Department of Geography, Vrije Universiteit Brussel, Brussels, Belgium*
[2] *Helmholtz Centre Potsdam, German Research Center for Geosciences (GFZ), Section 2.1, Potsdam, Germany.*
[3] *UGCT, Department of Physics and Astronomy, Ghent University, Ghent, Belgium.*
[4] *UGCT, Department of Geology and Soil Science, Ghent University, Ghent, Belgium*
e-mail: *sam.poppe@vub.ac.be*
session: *Volcanism and Volcanotectonics*

Introduction

Closed, near-circular, topographic depressions are common features on Earth and other planets. These are termed sinkholes or dolines in karst rock regions, and pit-craters (diameter $<\sim$1 km) or calderas (diameter $>\sim$ 1 km) in volcanic regions. Past analytical, numerical and analogue models mainly explored collapse caldera structures by documenting 2D and 3D model surface deformation, and 2D model cross-sections (e.g. Martí et al. 1994; Roche et al. 2000; Holohan et al. 2011). Kinematic and dynamic aspects of caldera collapse are less well understood, though a necessity for the interpretation of recent monitoring data.

We present here a novel application of computed X-ray micro-tomography (μCT) in (volcano-) structural analogue modeling. In this study, we illustrate the methodology through models of volumetric depletion of a sub-surface body and consequent destabilisation and gravitational collapse of the overburden. We investigate two end-member models: 1. Near-continuous collapse into a depleting sub-surface body; and 2. Near-instantaneous collapse into a large sub-surface cavity. Our model results correspond to a natural length scale of $\sim<$ 2 km of the surface depression's diameter, hence applicable to sinkholes, pit-craters and 'small' calderas.

The X-ray micro-tomography methodology

Our analogue model set-up is similar to the 'sandbox' used in most analogue studies (e.g. Martí et al. 1994; Roche et al. 2000). Two dry well-sorted silica sand – plaster mixtures (SP-mix) with cohesions of $\sim$180 and $\sim$300 Pa simulated brittle rock in near-continuous and near-instantaneous experiments, respectively. Golden syrup (GS) with a viscosity of $\sim$50 Pa.s (22°C) served as a fluid analogue (i.e. rock salt, fluid magma; see Figure 1). Garnet sand was used to make passive marker layers, as the difference in elemental composition and density between silica and garnet sand ensured an easily detectable contrast in radiographs. Drainage was initiated by lowering an external GS reservoir below the model base. Geometric, dynamic and kinematic scaling of the simulations was ensured by dimensionless analysis (cf. Roche et al., 2000).

Time-lapse radiographs taken at 2.5-minute intervals documented ongoing model deformation. Vertical subsidence rates were calculated from vertical displacements of the garnet marker layers in the radiographs. Volumes of the sub-surface fluid reservoir, collapsing overburden column and surface depression were calculated from surface areas assuming an axi-symmetrical geometry. After de-

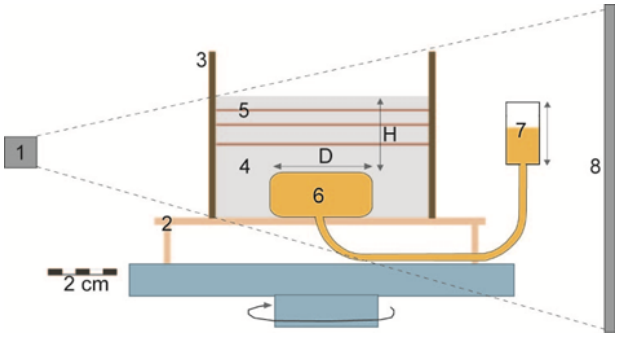

Fig. 1.: X-ray tomography set-up: 1. X-ray beam source; 2. Plastic stand with central outlet; 3. Plastic tube; 4. SP-mix; 5. Thin garnet sand marker layers; 6. GS analogue fluid body; 7. Silo containing GS, adaptable in elevation; 8. X-ray beam detector; H. Overburden height; D. Fluid body diameter.

formation, models were scanned with the μCT scanners of the UGCT (www.ugct.ugent.be; Masschaele et al. 2006). The spatial resolution was 80 - 111 μm, higher than in medical CT scanners. Data sets were reconstructed with the Octopus software. The Morpho+ and VGStudioMax software were used for 3D rendering of model volumes.

Results and Discussion

Near-instantaneous vs. near-continuous collapse

Two representative end-member models are depicted in Figure 2. Despite their much-reduced scale, our analogue models reproduced overall structural and morphological characteristics as modelled previously ((Fig. 2a-c); e.g. Martí et al., 1994; Roche et al., 2000; Geshi et al., 2012), and as observed or inferred from natural collapsed sinkholes, pit-craters and small calderas. Our highest-cohesion models reproduced sub-surface meta-stable cavities (Fig. 2d-e), which collapsed when triggered by mild tapping on the model (Fig. 2f). In these 'near-instantaneous' models, GS depletion had initially resulted in the coherent subsidence of a sub-surface block. Above this formed a convex-upward cavity, with its apex half-way in between initial reservoir level and the model surface. A 3D scan of a collapsed near-instantaneous model into a cavity demonstrates how the overall collapse structure resembles the near-continuous one, however the initial stratigraphy is highly disrupted on the small-scale (Figure 2f). Similar to rockslide avalanches (Glicken, 1996), this effect can be attributed to a rapid acceleration of the collapsing roof into the unconfined cavity.

Syn-collapse velocity and volume evolution

Patterns of vertical subsidence rate during depletion in models of near-continuous collapse demonstrate that, even within an apparently coherent column, spatially and temporally distinct slip events occur (cf. Ruch et al., 2012). The volumetric growth of the subsiding overburden occurred in our models through three processes: 1. Material was added as the collapse propagated upward and laterally within the overburden; 2. Material within the subsiding overburden underwent a volumetric expansion. This is seen as a decrease in the grey value of the subsiding overburden volume, (effective decrease of grain packing - cf. Panien et al., 2006); and 3. Material was added as debris from scarp failure of the surface depression once the collapse reached the surface. Differences between initial and final affected overburden column volumes in our models can be mainly attributed to the volumetric expansion of the brittle overburden within a collapse-bounding ring fault system. Such volumetric expansion of collapsing overburden is termed 'bulking', and has been reported in studies of mining collapse (e.g. Whittaker and Reddish, 1989), sinkhole formation (e.g. Andrejchuk and Klimchouk, 2002) and debris avalanches (Siebert, 1984).

Conclusion

This study illustrates a first use of computerized X-ray micro-tomography (μCT) to image and quantify the evolution of deformation in analogue models of overburden collapse induced by sub-surface fluid withdrawal. 3D μCT scans of

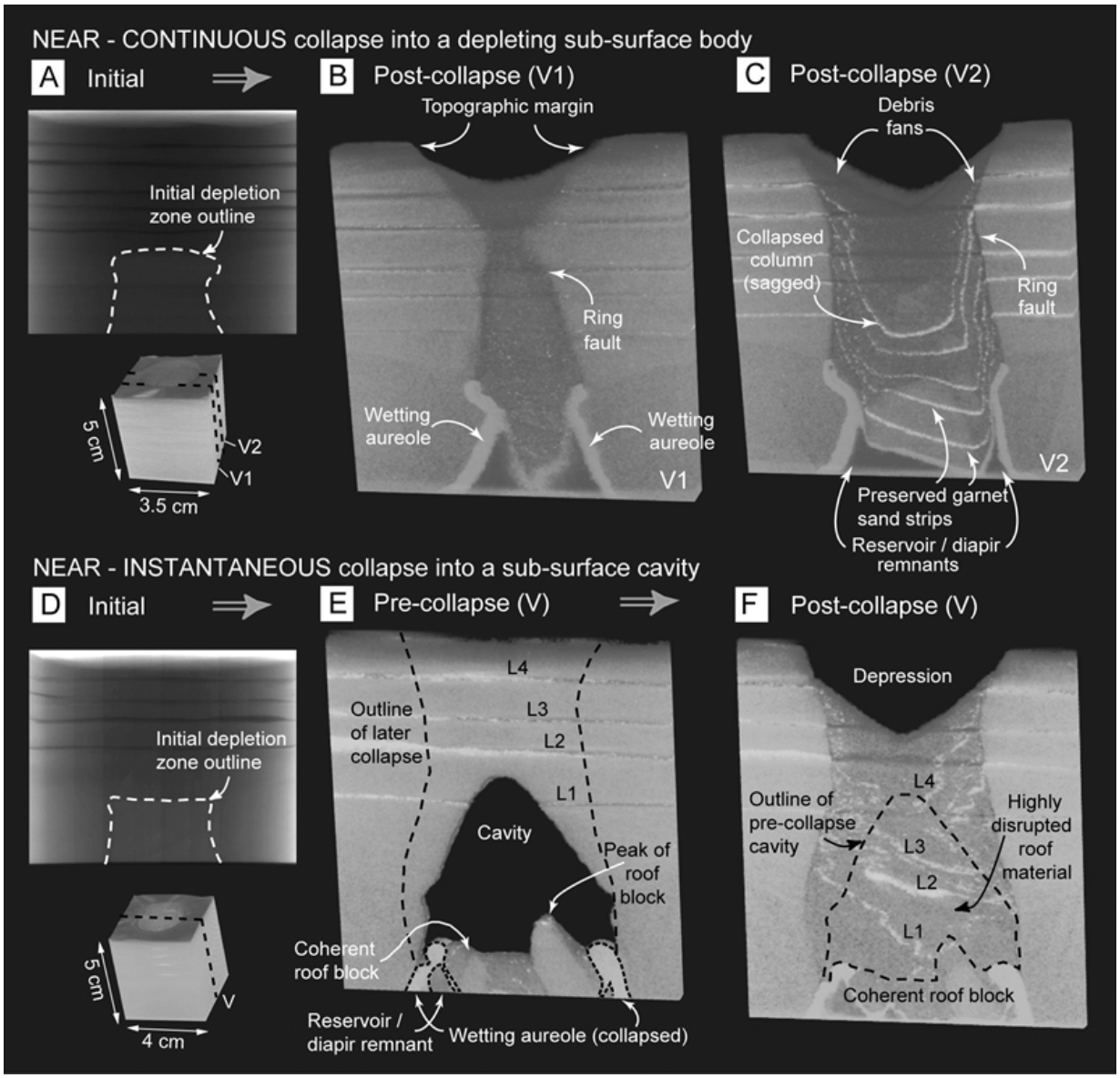

Fig. 2.: Representative models of (above) near-continuous collapse into a depleting sub-surface body and (below) near-instantaneous collapse into a sub-surface cavity: (A, D) Radiographs before depletion; (B, C) Vertical slices - V1 and V2, respectively, in part A - through a 3D scan of the near-continuously collapsed model. Note the differences in apparent ring fault geometry depending on position of cross section from the collapse center; (E, F) Vertical slices through 3D scans of the pre- and post-collapse stages of near-instantaneous collapse model. Note the greater small-scale disruption of the initial stratigraphy in (F) compared with that in (C).

models representing end-member styles of near-continuous collapse into a depleting sub-surface body versus near-instantaneous collapse into a large sub-surface cavity reveal that the final collapse structures are quite similar, except for a more pervasive small-scale disruption of the overburden in the latter case. Subsidence velocity patterns demonstrate subtle differential movements of discrete sections of overburden columns in 3D space, similar to previous results in 2D-space (Ruch et al., 2012). Lastly, a volumetric expansion of the collapsing overburden can be accounted for by a density reduction, i.e. 'bulking', of the brittle material. Further improvements of this μCT imaging methodology could lead to enhanced quantitative assessment of the geometry, kinematics and dynamics of volcano-tectonic processes, with the unique advantage of immediate comparison of modelling results to monitoring data in the field.

References

Andrejchuk, V. and Klimchouk, A., 2002. Int. J. Speleol., 31:1/4, 89-114.

Burchardt, S. and Walter, T.R., 2010, Bull. Volc., 72, 297-308.

Dahm, T., Heimann, S., and Bialowons, W., 2011, Nat. Haz., 58, 1111-1134.

Geshi, N., Shimano, T., Chiba, T. and Nakada, S., 2002, Bull. Volc., 64, 55-68.

Geshi, N., Acocella, V. and Ruch, J., 2012. Bull. Volc., 74, 1553-1567.

Glicken, H., 1996, U.S.G.S. Open File Report, 96-677, 90 pp.

Holohan, E.P., Schöpfer, M.P.J. and Walsh, J.J., 2011, J. Geophys. Res., 116.B07202, 23pp.

Kervyn, M., Boone, M.N., van Wyk de Vries, B., Lebas, E., Cnudde, V., Fontijn, K. and Jacobs, P., 2010, Geosph., 6(5), 482-498.

Martí, J., Ablay, G.J., Redshaw, L.T. and Sparks, R.S.J., 1994, J. Geol. Soc. Lond., 151, 919-929.

Masschaele, B.C., Cnudde, V., Dierick, M., Jacobs, P., Van Hoorebeke, L. and Vlassenbroeck, J., 2006, Nucl. Instr. & Meth. Phys. Res. Abstr., 580, 266-269.

Panien, M., Schreurs, G. and Pfiffner, A., 2006, J. Struct. Geol., 28, 1710-1724.

Roche, O., Druitt, T.H. and Merle, O., 2000, J. Geophys. Res., 105, 395-416.

Ruch, J., Acocella, V., Geshi, N., Nobile, A. and Corbi, F., 2012, J. Geophys. Res., 117, B07301.

Siebert, L., 1984. J. Volc. Geoth. Res., 22, 163-197.

Whittaker, B.N. and Reddish, D., 1989, Dev. Geotech. Engin., 56, Elsevier, 528 pp.

Mechanisms of entrainment of a granular substrate by pyroclastic density currents: insights from laboratory experiments and models, and implications for flow dynamics.

Olivier Roche[1], Yarko Niño[2]

[1]*Laboratoire Magmas et Volcans, Université Blaise Pascal-CNRS-IRD, Clermont-Ferrand, France.*
[2]*Department of Civil Engineering and Advanced Mining Technology Center, Universidad de Chile, Santiago, Chile.*
e-mail: *o.roche@opgc.univ-bpclermont.fr*
session: *Volcanism and Volcanotectonics*

Introduction

Pyroclastic density currents (PDCs) are gas-particle mixtures generated during volcanic eruptions by gravitational collapse of a lava dome or of an eruptive column, lateral explosion of a pressurized magma body, or during caldera collapse. They represent important natural hazards because they can propagate on distances of several kilometers from the eruptive vent, even on relatively horizontal topographies. Mitigation of hazards posed by PDCs, for instance through numerical simulations that can predict areas covered by the currents, requires a good knowledge of their fundamental physics.

Field studies of PDCs deposits have led volcanologists to propose two end-member emplacement mechanisms of the parent flows (Figure 1). A PDC is either a pyroclastic surge that is a fully turbulent dilute mixture with low particle volume fraction of ∼0.1-1% and bulk density of ∼1-10 kg/m^3, or consists of a pyroclastic flow that is a ground-hugging dense gas-particle mixture with a bulk density of ∼10^3 kg/m^3 and that is overridden by a turbulent ash cloud. Particle transport away from the eruptive vent is favored by turbulence in dilute PDCs or by long-lived high interstitial pore fluid pressure that reduces internal friction of the dense basal flow of PDCs. These two mechanisms have been proposed in particular for large ash-rich PDCs, whose accumulation form ignimbrites of volume up to several tens to hundreds of km^3. Such deposits often contain particles of size of several centimeters to decimeters captured from an underlying substrate by the parent currents. The substrate is commonly an earlier coarse-grained pyroclastic fall or flow deposit, the disaggregated surface of a debris avalanche or of a lava field, or a sedimentary fluvial conglomerate. In contrast, granular substrates such as fine-grained pyroclastic ash fall deposits are often not reworked by PDCs. These counter-intuitive observations serve as a base for the present study. Here we investigate the interaction mechanisms of PDCs with a granular substrate in order to discuss the mode of emplacement (dilute or dense) of the currents.

Dense gas-particle flow on a granular substrate

We carried out laboratory experiments to investigate the propagation of a dense PDC on a granular substrate. Experiments consisted on dam-break flows generated by sudden release of a granular material fluidized in a reservoir and that propagated on a horizontal granular layer of particles (Figure 2). The flow particles were fine glass

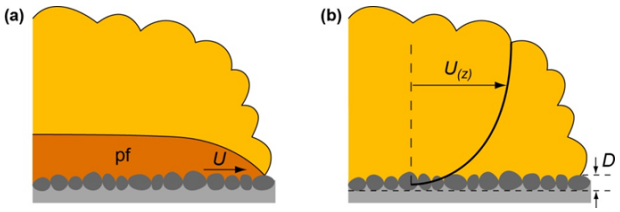

Fig. 1.: End-member pyroclastic density currents propagating on a granular substrate (not to scale). (a) Pyroclastic flow (pf) with front velocity U, overridden by a turbulent ash cloud. (b) Dilute turbulent current on a substrate of particles of mean size D, with mean velocity U(z) increasing upward.

beads of diameter d=80 μm that conferred a low material hydraulic permeability of $\sim 10-11$ m^2, which permitted slow diffusion of the interstitial pore fluid pressure generated before release and hence propagation in a fluid-like state at front velocity U$\sim$(gH)$^{1/2}$, with H the height of the initial reservoir height (Roche 2012). The flows were non turbulent, according to the terminology used for single-phase fluids. The granular substrate consisted of particles identical to those of the flows (d=80 μm) or were coarse glass or steal beads of size d=1500-1590 μm.

Experiments filmed at 1000 frames/s revealed different modes of interaction between the sliding head of the flow and the substrate (Figure 2). In case of a smooth substrate of fine particles, shear wake-like instabilities of height of $\sim$1 mm were generated. These structures stretched so much as the flow propagated that the final deposit revealed almost no evidence of entrainment. In contrast, flow particles penetrated into interstices between coarse beads forming a rough substrate. Most of the uppermost beads were first surrounded by the fines and entrained from the substrate, and then dragged very slowly (at $\sim$0.07U) at flow base. Many of the dragged beads were uplifted within the flow to a height up to $\sim$6-8 mm and were transported downstream. These beads finally settled at flow base and stopped motion, at the same time as the granular flow, at height up to $\sim$4-5 mm above the original top of the substrate.

Pore fluid pressure measurements at flow base revealed that the sliding head generated a relative underpressure (i.e. pressure less than atmospheric):

$$\Delta P = \gamma \rho U^2 \qquad (1)$$

where $\gamma \sim 0.06$ was an empirical constant in the experiments and $\rho \sim$1400 kg/m^3 was the bulk flow density. This caused an upward pressure gradient because (atmospheric) pore pressure within the substrate was almost unchanged. We made the hypothesis that this pressure gradient could cause uplift of the coarse substrate beads dragged slowly at flow base (this implies that the uplift mechanism was non operant in case of a smooth substrate whose particles were not entrained individually). Beads of volume V and density ρ_p could be uplifted at a critical pressure gradient $\Delta P_c = (\rho_p - \rho_{air})Vg/S$, where $S = \pi d^2/4$ was the effective area to which the upward force due to the pressure gradient was applied, so that $\Delta P_c = 2(\rho_p - \rho_{air})gd/3$. Experiments involving substrates of coarse glass or steal beads confirmed that onset of uplift did occur approximately at ΔP_c.

We used our experimental findings to infer the velocity of pyroclastic flows as a function of the characteristics of substrate-derived particles found in PDC deposits. Assuming that particles had the ideal shape of a parallelepiped and were uplifted with their short axis a vertical according to the condition of minimum energy, then $\Delta P_c = (\rho_p - \rho_{air})ga$, and from eq. 1,

$$U = \sqrt{\frac{(\rho_p - \rho_{air})ga}{\gamma \rho}} \qquad (2)$$

Results in figure 3 predict that the biggest blocks of typical size a$\sim$1-1.5 m and density $\rho_p \sim$2000-3000 kg/m^3 reported in literature can be entrained by dense PDCs of velocity of 25-30 m/s (assuming ρ 875-1400 kg/m^3 for fluidized dense pyroclastic flows, see Roche et al. 2013 for details). Comparison with natural data suggests that our model is robust. The 18 May 1980 eruption at Mount St Helens is a rare example where velocity of pyroclastic flows was measured from video analysis. Blocks of size a=0.25-0.35 m and

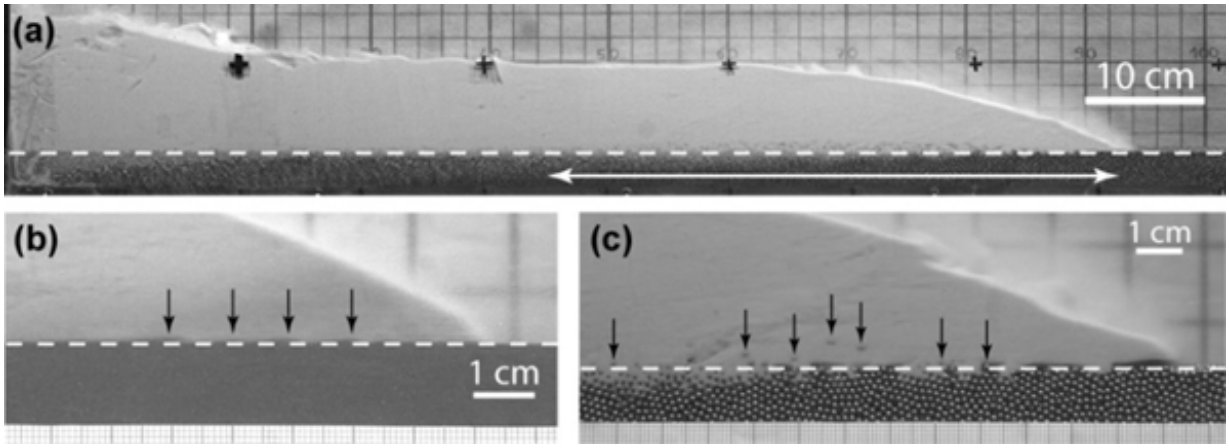

Fig. 2.: Experimental dam-break dense gas-particle flows on a granular substrate. (a) General view of a flow fluidized initially in the reservoir (left, not shown) and propagating at front velocity U=3.06 m/s. The double arrow shows the sliding head. (b) Flow on a smooth substrate of fine glass beads, with small instabilities at base (arrows). (c) Flow on a rough substrate of steal beads, with individual uplifted beads shown by arrows.

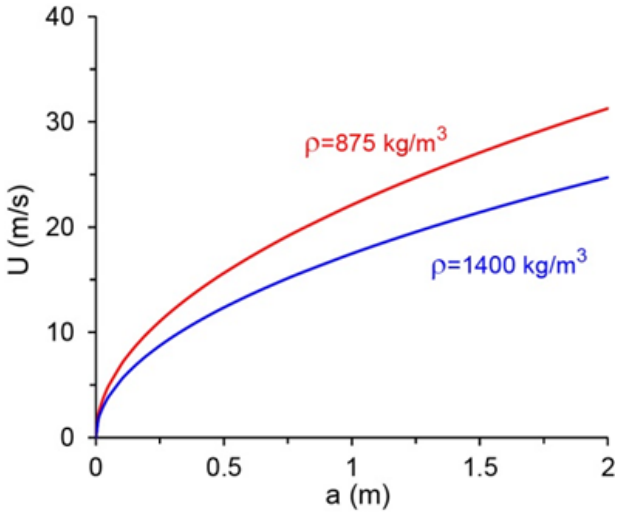

Fig. 3.: Front velocity of pyroclastic flows as a function of the size of substrate-derived particles of typical density ρ_p=2500 kg/m^3. ρ is the bulk flow density.

density ρ_p ~2600 kg/m^3 were captured by pyroclastic flows at ~5.6-7.2 km from the vent on gentle slope <4° (Brand et al. 2014). According to eq. 2, the corresponding velocity of the pyroclastic flows was ~10 m/s, in excellent agreement with field observations.

Dilute turbulent current on a granular substrate

The case of a dilute PDC on a substrate of particles is treated theoretically by considering a hydraulically rough, turbulent fluid flow with low particle concentration (Figure 1). The aim is to determine the current velocity at some height above the ground, where it can be measured in nature, and the corresponding velocity profile required for entrainment of substrate particles of mean size D. The velocity profile of the current is:

$$U_{(z)} = \frac{u_*}{\kappa} ln\Big(\frac{z}{z_0}\Big), \qquad (3)$$

where $U_{(z)}$ is the mean flow velocity at height z, u_* is the shear velocity, κ=0.4 is the von Karman constant, and z_0=D/30 is the hydrodynamic roughness (Garcia 1999). The ability of the current to entrain substrate particles through both traction and saltation depends on the dimensionless Shields number:

$$\theta = \frac{\rho u_*^2}{(\rho_p - \rho) g D}. \qquad (4)$$

The critical Shields number required to set particles in motion depends on the particle Reynolds number $Re_p = u_* D/\nu$, where ν is the gas

kinematic viscosity. Here we consider the dimensionless particle diameter $R_p = Re_p/\theta^{1/2} = [(\rho_p - \rho)gD^3/\rho]^{1/2}$ defined by Niño et al. (2003) because it is independent on u_*, which is unknown in the present case. For turbulent PDCs and substrate particles of typical size of 0.1-1 m and density of 2000-3000 kg/m^3, $R_p > 10^5$ (i.e. $Re_p > 10^4$), which means that we have to consider a range of critical Shields number θ_c=0.052-0.086 according to the extensive data compilation of Buffington and Montgomery (1997). This range reflects various arrangements and shapes of the substrate particles. Combining eqs. 3 and 4 permits to eliminate u_* and gives the critical velocity profile required to set in motion substrate particles of maximum size D,

$$U_{c(z)} = \frac{1}{\kappa}\sqrt{\frac{\theta_c(\rho_c - \rho)gD}{\rho}}ln\Big(\frac{z}{z_0}\Big) \qquad (5)$$

Results are presented in Figure 4 for a current of bulk density of 2 kg/m^3 (larger than that of atmosphere) or 10 kg/m^3 (maximum value given in literature) and considering typical substrate particle density ρ_p=2500 kg/m^3 and current thickness of ∼500 m. They show that even for relatively small blocks of size of 10 cm, the flow velocity at height of a few hundred meters above the ground required for entrainment is significantly higher than the maximum velocity U_{max}=100 m/s commonly accepted in literature for dilute PDCs. In fact, the size of substrate particles that can be entrained by dilute currents is of a few centimeters if U_{max}, for instance at height of 500 m typical of most currents, is assumed.

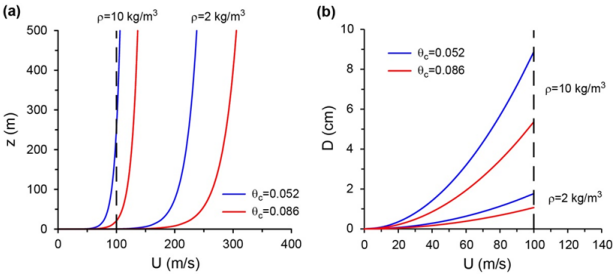

Fig. 4.: Conditions required for entrainment of substrate particles of density ρ_p=2500 kg/m^3 by a dilute PDC, for ranges of bulk flow densities (ρ) and critical Shields number (θ_c), with maximum velocity U_{max}=100 m/s indicated by a dashed line. (a) Critical current velocity as a function of height z for particles of size D=10 cm. (b) Size of entrained substrate particles as function of the critical current velocity at z=500 m.

Conclusion

Our study suggests that substrate-derived particles in PDC deposits can provide information on the dynamics of the parent currents. Dilute turbulent PDCs are able to entrain substrate particles of size of a few centimeters if a maximum current velocity of ∼100 m/s at height of a few hundred meters above the ground is considered. Therefore, we infer that blocks larger than ∼10 cm can be entrained by PDCs if these consist of a concentrated basal pyroclastic flow. According to our experiments, capture can occur through uplift caused by an upward pressure gradient at the flow-substrate interface once substrate particles are dragged individually at flow base. Considering the size and density of substrate particles found in PDC deposits, we infer front velocities up to ∼25-30 m/s for pyroclastic flows. In contrast, substrates of fine particles of size similar to that of the flow particles are not eroded because the flow slides on the smooth substrate and renders the uplift mechanism non operant.

References

Brand, B.D., Mackaman-Lofland, C., Pollock, N.M., Bendaña, S., Dawson, B., Wichgers, P. (2014). Dynamics of pyroclastic density currents: Conditions that promote substrate erosion and self-channelization - Mount St Helens, Washington (USA). J. Volcanol. Geotherm. Res. 276, 189-214.

Buffington, J.M., Montgomery, D.R. (1997). A systematic analysis of eight decades of incipient motion studies, with special reference to gravel-bedded rivers. Water Res. Res. 33, 1993-2029.

García, M. (1999). Sedimentation and erosion hydraulics, in: Mays, L.W. (Ed.), Hydraulic

Design Handbook, McGraw-Hill Professional, chapter 6. Niño, Y., García, M. (2003). Threshold for particle entrainment into suspension. Sedimentology 50, 247-263.

Roche, O. (2012). Depositional processes and gas pore pressure in pyroclastic flows: an experimental perspective. Bull. Volcanol. 74, 1807–1820.

Roche, O., Niño,Y., Mangeney, A., Brand, B., Pollock, N., Valentine, G.A. (2013). Dynamic pore-pressure variations induce substrate erosion by pyroclastic flows. Geology 41, 1107–1110.

Influence of crust type on the long-term deformation of a volcano: example from Mt. Etna (Italy)

Salvatore Scudero[1], Giorgio De Guidi[1], Sebastiano Imposa[1], Mimmo Palano[2]

[1] *University of Catania, Department of Biological, Geological and Environmental Sciences, Earth Science Section, Corso Italia 57, 95129, Catania, Italy*
[2] *Istituto Nazionale di Geofisica e Vulcanologia, Osservatorio Etneo - Sezione di Catania, Piazza Roma 2, 95123, Catania, Italy*
e-mail: *salvatore.scudero@gmail.com*
session: *Volcanism and Volcanotectonics*

Introduction

The volcanic areas experience the greatest deformation in term of velocity and spatiotemporal variability. Cyclic episodes of short-term inflation and deflation, registered during eruptions, are related to magma chambers or dykes migration. Long-term deformations are ascribable to intrusion of large subvolcanic bodies into the crust or even to sub-crustal processes like the rise of a mantle plume. Unfortunately, is not always possible to discriminate among all these processes because they superimpose in space and in time.

In this research, bringing the example of Mt. Etna volcano (Italy), we highlight the existence of a source of deformation not directly related to a volcanic process, but that is rather related to the nature of the crust hosting the volcanism.

The occurrence of "anorogenic" volcanism such Mt. Etna in the collisional context of the Central-Mediterranean area can sometimes appear anomalous (Lustrino et al. 2011), and is a part of why the tectonic origin of volcanism of Mt. Etna is still debated. Also debated is the nature of the crust on which Mt. Etna emplaced about 500 ka. Several authors suggest that this crustal block is not continental but it is rather a remnant of an old, weathered oceanic crust (Sapienza and Scribano 2000; Ciliberto et al. 2009; Manuella et al. 2013; Barreca 2014).

In this work we are able to accurately describe and model the altimetric distribution of a stratigraphic marker within the Etnean substratum and, taking into account the geological features of the area, we identify the different individual Quaternary deformation processes that have interacted.

Late quaternary deformation at Mt. Etna

A basin filled with more than 1000 m of pelagic sediments (dated at 1.2-0.6 Ma; Di Stefano and Branca 2002) lie south of Mt. Etna. The marine deposits are widespread below the entire volcanic edifice although they crop out only locally where they have not been covered by younger deposits and lava flows. They comprise 600 m of marly clays with rare, thin, sand levels evolving upwards in tens of meter of thicker yellow sands with intercalations of polygenic conglomerate. The transition between marly clays and sand is easy to detect in boreholes or geophysical surveys and represents a very useful stratigraphic marker. We detected this marker in 3056 borehole logs; the overall altitude range of the data is between -98 m below and 452 m above sea level.

Knowing the deposition depth and the age of the deposit we can estimate the vertical deformation rate for the marker. Moreover, considering the main tectonic features of the study area (Catalano et al. 2011), we are able to detect sources of deformation with different magnitude

(from 0.2 mm/y to 1.3 mm/y) and acting at different scale (local and regional). In detail we recognize:

1. homogeneous, regional uplift (from 0.3 mm/y to 0.5 mm/y) interpreted either as an isostatic response to the passive subduction of the detached Ionian slab (Wortel and Spackman 2000) or as an asthenospheric flow at the lateral edge accompanying the roll-back of the slab (Shellart 2010; Faccenna et al. 2011);

2. localized uplift coherent with the activity of two local thrust ramps;

3. differential uplift component linearly increasing northwards and not ascribable to the known features of the area.

Other morphological markers (Late-Pleistocene marine terraces and a submerged marine platform of 20 ka) are consistent with the last, so far unknown, source of deformation. Our study suggests that it acted in the same area, constantly over time, and with rates ranging from 0.16 mm/y to 0.75 mm/y (De Guidi et al., 2014). Considering its bell-like pattern and its almost axial position with the volcano, we propose a volcano-related origin for this uplift component.

Certainly very short-term deformations affect the volcanic edifice, (e.g. inflation and deflation), but, it is reasonable to suppose that over long periods these localized, cyclic deformations become negligible and, we require a greater, stable source of deformation to explain the pattern of surface doming.

Modelling

To model the doming we performed an analytical inversion of the whole buried sedimentary substrate of Mt. Etna. To minimize effects of erosion before the substrate was covered by lava flows we selected only the ridges of the paleovalleys, therefore avoiding the areas with greatest loss of material.

The estimated vertical component of the domical deformation was used as an input to constrain an isotropic half-space elastic inversion model, as is routinely done with GPS and InSAR ground-deformation data. Values of 30 GPa and 0.25 were assumed for the shear modulus and Poisson's ratio in the half-space, respectively. The value of the shear modulus chosen corresponds to a typical value of crustal rigidity commonly used in modeling which is found to be an average rigidity value for Mt. Etna (Chiarabba et al. 2000). The inversions were performed by using the genetic algorithm approach. Because of the data's distribution and the 1D nature of deformation data, to model the observed vertical ground deformation pattern we adopted the point source model (Mogi 1958), representing the simplest source used in volcano deformation modeling. In order to test biases due to our chosen starting parameters, we performed several inversions with different sets of model parameters. In all inversions, the algorithm converged rapidly to a similar solution. The best result indicates a pressure source located at a depth of 16.4 km b.s.l. beneath the upper western flank of the volcano with a volume change of $3.8 \cdot 10^6$ m^3/yr . This source is able to explain a large amount of the observed uplift and rates, reproducing well the wavelength of the deformation pattern (Fig. 1).

Although a viscoelastic rheology could be more appropriate to describe the medium at the mantle-crust transition, we retain a simple elastic rheology because i) the deformation's vertical component alone is insufficient to constrain the depth of the pressurized magma body using a viscoelastic rheology, because the main effect of viscous deformation is to reduce the contribution of the horizontal component of deformation with respect the vertical component as function of the viscosity, and ii) there is little known about the viscoelastic medium beneath Etna at depths greater than 10 km.

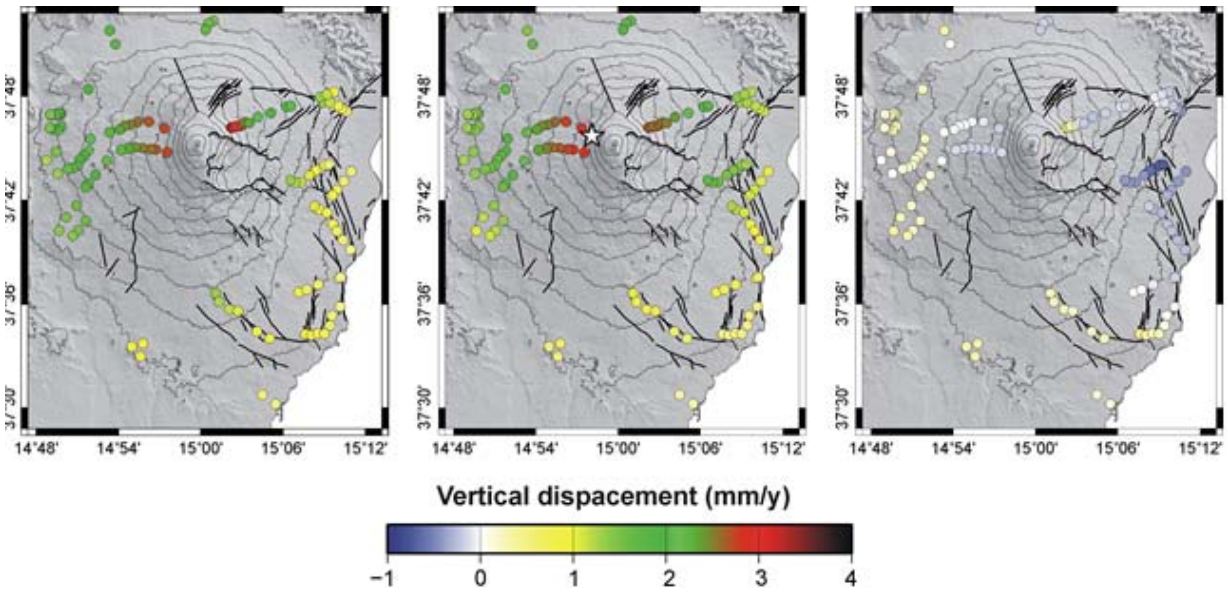

Fig. 1.: Observed deformation pattern of the buried sedimentary substrate (left), calculated deformation (centre) and residual differences between observed and calculated (right); the white star represent the projection of the source of deformation; black lines represent the faults.

Conclusions

Several authors suggest that the Hyblean crust (i.e. the crust under Mt. Etna) is a remnant of an old, weathered oceanic crust. It is also confirmed the existence of a Triassic hydrothermal fossil system which reactivation, connected with magmatic episodes, caused the diapiric emplacement of serpentinized clays at shallow level in the crust (Scribano et al. 2006; Manuella et al. 2012; Barreca 2014).

The process and the mechanism leading to the formation of serpentinites intrusions are consolidated in the literature (Fryer and Fryer 1987; Fryer 2002). The increase of volume that drives the diapiric uprise has been estimated to be ∼40% (Iyer et al. 2010) and the uplift rate ranging from mm to cm per year (Skelton and Jakobsson 2007). Giant diapirs up to 2 km in height have been recognized worldwide showing conical shapes at surface (Fryer et al. 1990; Fryer 2002; Schuiling 2011). Within this frame, the doming of Mt. Etna could result from a volcano-driven diapiric emplacement of a notable amount of hydrothermal material from the lower crust to the shallow levels. In various areas of this crustal block (onshore and offshore) there are geological and geophysical evidences of such intrusions (Catalano et al. 2000; Manuella et al. 2012). Minor evidences of this phenomenon are represented by superficial hydrothermal activity widespread all around the volcanic edifice. Moreover the contemporaneous beginning of the doming and of the volcanic activity at Mt. Etna (∼ 600 ky) strongly support this hypothesis.

Even agreeing with the mantle-plume origin of Mt. Etna as suggested by some authors (Tanguy et al. 1997; Clocchiatti et al. 1998; Montelli et al. 2003) a rising thermal anomaly would melt the lithospheric mantle rather than provoke its volumetric expansion causing, in the long term, the thinning of the overlying crust and not the crustal arching (Burov and Guillou-Frottier 2005; Sleep et al. 2006; Leng and Zhong 2010), therefore a mantle-related process is definitely excluded.

Volcanic doming with similar uplift patterns and magnitude is encountered in other volcanic districts (Acocella and Mulugeta 2001; Zhong and Watt 2002; Pim et al. 2008; Marturano et al. 2011), but the causative mechanism has sometimes been neglected. Therefore considering the nature of the crust is of fundamental import-

ance approaching the long.-term deformation of a volcano.

Acknowledgements

This work was supported by grants from V3 Project (DPC-INGV agreement).

References

Acocella V, Mulugeta G (2001) Surface deformation induced by pluton emplacement: the case of Amiata (Italy). Phys Chem Earth 26:355–362

Barreca G (2014). Geological and geophysical evidences for mud diapirism in south-eastern Sicily (Italy) and geodynamic implications. Journal of Geodynamics.

Burov E, Guillou-Frottier L (2005) The plume head–continental lithosphere interaction using a tectonically realistic formulation for the lithosphere. Geophysical Journal International 161(2): 469-490

Catalano R, Franchino A, Merlini S, Sulli A (2000) A crustal section from the Eastern Algerian basin to the Ionian ocean (Central Mediterranean).Mem Soc Geol It 55: 71-85.

Catalano S, Torrisi S, Tortorici G, Romagnoli G (2011) Active folding along a rift-flank: The Catania region case history (SE Sicily). J Geodyn 51:53-63

Chiarabba C, Amato A, Boschi E, Barberi F (2000) Recent seismicity and tomographic modeling of the Mount Etna plumbing system. J. Geophys. Res. 105: 10923-10938

Ciliberto E, Crisafulli C, Manuella FC, Samperi F, Scirè S, Scribano V, Viccaro M, Viscuso, E (2009) Aliphatic hydrocarbons in metasomatized gabbroic xenoliths from Hyblean diatremes (Sicily): Genesis in a serpentinite hydrothermal system. Chemical Geology 258(3): 258-268

Clocchiatti R, Schiano P, Ottolini l, Bottazzi P (1998) Earlier alkaline and transitional magmatic pulsation of Mt. Etna volcano. Earth Planet Sci Lett 163:399–407

De Guidi G, Imposa S, Scudero S, Palano M (2014). New evidence for Late Quaternary deformation of the substratum of Mt. Etna volcano (Sicily, Italy): clues indicate active crustal doming. Bull Volc 76(5): 816

Di Stefano A, Branca S (2002) Long-term uplift rate of the Etna volcano basement (southern Italy) based on biochronological data from Pleistocene sediments. T Nov 14:61-68

Faccenna C, Molin P, Orecchio B, Olivetti B, Bellier O, Funicello F, Minelli L, Piromallo C, Billi A (2011) Topography of the Calabria subduction zone (southern Italy): Clues for the origin of Mt. Etna. Tect 30:TC1003

Fryer P (2002) Recent studies of serpentinite occurrences in the oceans: Mantle-ocean interactions in the plate tectonic cycle. Chemie Der Erde-Geochemistry 62(4): 257-302.

Fryer P, Fryer GJ (1987) Origins of nonvolcanic seamounts in a forearc environment. Geophysical Monograph Series 43: 61-69

Fryer P, Saboda K L, Johnson LE, Mackay ME, Moore GF, Stoffers P (1990) Conical Seamount: SeaMARC II, Alvin submersible, and seismic reflection studies. In Proc. Ocean Drill. Program Sci. Results 125: 69-80

Iyer K, Rüpke LH, Morgan JP (2010) Feedbacks between mantle hydration and hydrothermal convection at ocean spreading centers. Earth and Planetary Science Letters 296: 34–44

Leng W, Zhong S (2010) Surface subsidence caused by mantle plumes and volcanic loading in large igneous provinces. Earth and Planetary Science Letters 291(1): 207-214

Lustrino M, Duggen S, Rosenberg CL (2011) The Central-Western Mediterranean: Anomalous igneous activity in an anomalous collisional tectonic setting. Earth Sci Rev 104:1–40

Manuella FC, Brancato A, Carbone S, Gresta S (2013) A crustal-upper mantle model for southeastern Sicily (Italy) from the integration of petrologic and geophysical data. Journal of Geodynamics 66: 92-102

Manuella FC, Carbone S, Barreca G (2012) Origin of saponite-rich clays in a fossil serpentinite-hosted hydrothermal system in the crustal basement of the Hyblean Plateau (Sicily, Italy). Clays and Clay Minerals 60(1): 18-31

Marturano A, Aiello G, Barra D (2011) Evidence for Late Pleistocene uplift at the Somma-Vesuvius apron near Pompeii. J Volcanol Geotherm Res 202:211-227

Mogi, K. (1958) Relation between the eruptions of various volcanoes and the deformations of the ground surfaces around them, Bull. Earthquake Res. Inst. Univ. Tokyo, 36, 99-134

Montelli R, Nolet G, Dahlen FA, Masters G, Engdahl ER, Hung SH (2004) Finite-frequency tomography reveals a variety of plumes in the mantle, Science 303:338-343

Pim J, Peirce C, Watts AB, Grevemeyer I, Krabbenhoeft A (2008) Crustal structure and origin of the Cape Verde Rise. Earth Planet Sci Lett 272:422-428

Sapienza G, Scribano V (2000) Distribution and representative whole-rock chemistry of deep-seated xenoliths from the Iblean Plateau, South-Eastern Sicily, Italy. Periodico di Mineralogia 69(2): 185-204

Schellart WP (2010) Mount Etna-Iblean volcanism caused by roll-back induced upper mantle upwelling around the Ionian slab edge: an alternative to the plume model. Geol 38/8:691–694

Scribano V, Sapienza G, Braga R, Morten L (2006) Gabbroic xenoliths in tuff-breccia pipes from the Hyblean Plateau: insights into the nature and composition of the lower crust underneath South-eastern Sicily, Italy.Mineralogy and Petrology 86(1-2): 63-88

Skelton A, Jakobsson M (2007) Could peridolite hydralion reactions have provided a contributory driving force for Cenozoic uplift and accelerated subsidence along the margins of the North Atlantic and Labrador Sea? Norvegian Journal of Geology, 87(1/2): 241 -248

Sleep NH (1990) Hotspots and mantle plumes: Some phenomenology. Journal of Geophysical Research: Solid Earth 95(B5): 6715-6736

Tanguy JC, Condomines M, Kieffer G (1997) Evolution of the Mount Etna magma: constraints on the present feeding system and eruptive mechanism. J Volcanol Geotherm Res. 75:221–250

Wortel MJR, Spakman W (2000) Subduction and slab detachment in the Mediterranean-Carpathian region. Science 290:1910-1917

Zhong S, Watt AB (2002) Constraints on the dynamics of mantle plumes from uplift of the Hawaiian Islands. Earth Planet Sci Lett 203:105-116

Analogue and numerical modeling of rifting events. Complementary tools to understand the rifting process.

Trippanera D.[1], La Marra D.[1], Acocella V.[1], Ruch J.[1], Rivalta E.[2]

[1]*Roma Tre University, Rome, Italy*
[2]*GFZ, Potsdam, Germany*
e-mail: *daniele.trippanera@uniroma3.it*
session: *Volcanism and Volcanotectonics*

Rifts are typical features of divergent plate boundaries that usually composed of normal faults, graben and eruptive fissures. The relative role played by magma and tectonics in controlling the geometry, kinematics and evolution of rifts are still unclear. Recent observations of rifting events clearly associated to dike injections along the divergent plate boundaries have highlighted the importance of magma in shaping rifts. Rifts are studied by means of the InSAR technique, by seismology and structural geology. However, geodetic and seismic data allow us to observe only an instant frame of the entire rifting process, in terms of geological times. Moreover, field observations along the rifts allow us to see only a static photograph taken in a certain time of the rift life, representing only the expression of the cumulative long (or short) time surface deformation.

To better observe and understand the entire rifting process from its beginning to its mature stage, we use analogue and numerical modeling. Since recent observations point out that dike injections are intimately related to the surface deformation during the rifting episodes, we decide to perform analogue and numerical models of multiple dike injections and to observe the surface deformation induced by them. The analogue experiments allow us to reproduce in laboratory the rift formation and evolution through time. The numerical models help us to better understand both the results of the analogue models and the natural process. Moreover, both types of model, allow us to investigate one by one the different parameters acting in the rifting process.

The main aims are to understand: 1) if dikes are able to generate all the long term surface deformation observed on the field along the rifts and 2) how the diking process can eventually affect the rift formation and its evolution. The starting point for the analogue models are the physical models performed by Mastin and Pollard, 1988. They intruded cardboard sheets inside a sleeve - able to dilate - consisting of two sheets of linoleum. We use the same concept of Mastin and Pollard, 1988 aiming to improve their models using new observation techniques and different materials. The setup consists of a rectangular glass box placed on a table and filled with crushed silica sand, the host rock analogue. Using this material, 1 cm on the model corresponds to ≈200m in nature. An intrusion apparatus is located in the box center, in which the dike analogues (0.5 mm thick iron plates) are intruded one by one. In this way, during the evolution of a single model the dike depth remains constant while the intrusion thickness increases progressively (from 0 up to 1 cm at maximum). In order to test the effect of the intrusion depth, different analogue models have been performed varying the sand thickness above the intrusion tip (from 1 cm to 8 cm). Two intrusion geometries have been also tested, in order to investigate the effect of the maximum dilation on the intrusion top: the final shape of the intrusion apparatus tip is flat in one case (rectangular shape) and sharp in the other

case (triangular shape). The surface deformation has been monitored by means of a laser scan with a sub-millimeter resolution (for vertical displacement) and the Particle Image Velocimetry (PIV) technique (for horizontal displacement). The results of the analogue models show that, intruding dikes, a depression with different geometry forms above the dike tip. The depression geometry and the relative fault kinematics vary according to depth and shape of the intrusion. For our numerical models we use the COMSOL Multiphysics software. We reproduce the same geometries of the analogue models (box included). In order to model the flat intrusion tip we use the boundary conditions that allow us to replicate the analytical solutions for constant-opening rectangular dislocations. To avoid artificially induced subsidence we set the top of the intrusion fixed along the vertical axis. Then, to numerically simulate the triangular intrusion shape we use a mathematical function imposing an opening that increases from the top to the bottom of the intrusion. One of the main aims of numerical models is to observe the pattern of the stress induced by the different intrusion geometries and to understand how these can affect the depression geometries (e.g. control on the fault trajectories by the maximum compressive stress change) and the fault kinematics (amount of stress induced at surface).

The results of the numerical models show that the intrusion geometry affects the pattern of the induced stress and the maximum compressive stress change trajectories. We also observe that for the same intrusion depths, the geometry of the intrusion tip affects the amount of surface deformation. These results are consistent with those obtained by means of analogue models.

Finally, in order to simulate the long term rifting cycle – based on the recent rifting events data and the natural basalt properties – we perform numerical models of dikes opening at different depths. We model dikes with an elliptical geometry (more similar to natural cases), applying a progressive dike dilations from 1 to 10 m. By means of these models we also aim to calculate the critical dike depth (D) / thickness (T) ratio beyond which it is possible to have surface fracturing induced by the dike injections.

Analogue and numerical models suggest that the geometry of the faults observed in the analogue models are compatible with some features observed along the eruptive fissure (e.g. Laki, Iceland) and the fissural areas of the magmatic systems and central volcanoes (Krafla, Reykjanes in Iceland; MER in Ethiopia; Hawaii). In addition, the surface displacement observed in the models is also consistent with the deformation pattern observed by means of analytical and geodetic data acquired during the recent rifting events (eg. Krafla, Dabbhau). Moreover, the geometry of the depression is strongly controlled by the D/T ratio parameter because of different stress distribution related to the different intrusion geometry. The D/T ratio together with the least litostatic load and the free surface effect near the surface also controls the possibility to have or not brittle failure at surface during dike injections.

These dataset allow us to suggest that diking is the primary way to form rifts along magmatic divergent plate boundaries and central volcanoes.

Scientific Programme

GeoMod2014 - Conference Outline

Time	31. August	1. September	2. September	3. September
08:45 - 09:00	-	Welcome	-	-
09:00 - 11:00	-	(Seismo-)tectonics (orals)	Volcanism and Volcanotectonics (orals)	Rheology (orals)
11:00 - 13:00	-	(Seismo-)tectonics (posters)	Volcanism and Volcanotectonics (poster)	Rheology (poster)
13:00 - 14:00	-	Lunch break	Lunch break	Lunch break
14:00 - 16:00	-	Tectonics and Surface processes (orals)	Geodynamics (orals)	Fluids and Deformations (orals)
16:00 - 18:00	-	Tectonics and Surface processes (poster)	Geodynamics (posters)	Fluids and Deformations (poster)
18:00 - 21:00	Ice Breaker Party	-	-	-
19:00 - 22:00	-		Joint Conference Dinner	-

GeoMod2014 - Short course on "Constitutive Laws: from Observation to Implementation in Models" by Onno Oncken, Mathias Rosenau, Fabio Corbi, Georg Dresen Erik Rybacki, Stephan Sobolev, and Sascha Brune
Thursday 4 September: 09:00 - 18:00
Friday 5 September: 09:00 - 14:00

GeoMod2014 - Hands-on tutorial on "ASPECT: a next-generation geodynamic modelling software" by Anne Glerum and Juliane Dannberg
Thursday 4 September: 09:00 - 18:00: Tutorial
Friday 5 September: 09:00 - 18:00: ASPECT Strategy Workshop (for Advanced Users) - voluntary

GeoMod2014 Conference Programme (31 August - 3 September)

Sunday 31 August 2014

18:00 - 21:00: Ice Breaker Party at the 'Theaterschiff Potsdam' (Schiffbauergasse 9b, 14467 Potsdam)

Monday 1 September 2014

08:45 - 09:00: Welcome by Prof. Dr. Dr. h.c. Reinhard Hüttl and Prof. Dr. Onno Oncken

09:00 - 11:00: (Seismo-)tectonics Orals (chairs: B. Kaus, O. Oncken)

- 09:00 - 09:30: **Kelin Wang:** *Thermal Expressions of Stick-slip and Creeping Subduction Megathrusts* (keynote)
- 09:30 - 10:00: **Bertrand Maillot:** *The long-term Evolution of Fold-and-Thrust Belts: Consistency of Numerical Approaches and Physical Experiments* (keynote)
- 10:00 - 10:20: **Tasca Santimano** et al.: *Smart or Beautiful? Accretionary wedge evolution seen as a competition between minimum work and critical taper*
- 10:20 - 10:40: **Lorenzo Bonini** et al.: *The role of pre-existing frictional weaknesses on the propagation of extensional faults*
- 10:40 - 11:00: **Ylona van Dinther** et al.: *Seismo-thermo-mechanical modeling of subduction zone seismicity*

11:00 - 13:00: (Seismo-)tectonics Posters (chairs: B. Kaus, O. Oncken)

13:00 - 14:00: Lunch break

14:00 - 16:00: Tectonics and Surface processes Orals (chairs: F. Graveleau, N. Hovius)

- 14:00 - 14:30: **Ritske Huismans:** *Interaction and feedback between surface processes and mountain building* (keynote)
- 14:30 - 15:00: **Stéphane Dominguez:** *Joint analogue modelling of marine and terrestrial geological processes: state of the art and new developments* (keynote)
- 15:00 - 15:15: **Utsav Mannu** et al.: *Dynamic Modelling of Accretionary Prisms and Stratigraphy of Forearc basins*
- 15:15 - 15:30: **Karen Leever:** *3D Analogue Modelling of the Effect of Fan Sedimentation on Accretionary Wedge Dynamics – the Magdalena Fan case, South Caribbean Margin, Colombia*
- 15:30 - 15:45: **Frank Zwaan**, Guido Schreurs: *4D Transfer Zone Modeling in Continental Rift Systems*
- 15:45 - 16:00: **Sergei Medvedev**, Ebbe H. Hartz: *Evolution of topography of post-Devonian Scandinavia: Effects and rates of erosion*

16:00 - 18:00: Tectonics and Surface processes Posters (chairs: F. Graveleau, N. Hovius)

Tuesday 2 September 2014

09:00 - 11:00: Volcanism and Volcanotectonics Orals (chairs: O. Galland, E. Holohan)

- 09:00 - 09:30: **Rikke Pedersen:** *Surface deformation simulations of volcanic and tectonic processes in Iceland* (keynote)
- 09:30 - 10:00: **Olivier Roche**, Yarko Niño: *Mechanisms of entrainment of a granular substrate by pyroclastic density currents: insights from laboratory experiments and models, and implications for flow dynamics* (keynote)
- 10:00 - 10:15: **Rosanne Heistek** et al.: *Temporal changes in mantle wedge geometry and magma generation processes in the Central Andes: towards linking petrological data to thermomechanical models*
- 10:15 - 10:30: **Francesco Maccaferri** et al.: *The gravitational unloading due to rift depression: A mechanism for the formation of off-rift volcanoes in (continental) rift zones*
- 10:30 - 10:45: **Lola Chanceaux**, Thierry Menand: *Solidification effects on sill formation: an experimental approach*
- 10:45 - 11:00: Max Gallagher, **Ben Kennedy** et al.: *Megatsunami generation from caldera subsidence*

11:00 - 13:00: Volcanism and Volcanotectonics Posters (chairs: O. Galland, E. Holohan)

13:00 - 14:00: Lunch break

14:00 - 16:00: Geodynamics Orals (chairs: F. Funiciello, S. Sobolev)

- 14:00 - 14:30: **Anne Davaille:** *Plumes to Plate Tectonics: Insights from Laboratory Experiments* (keynote)
- 14:30 - 15:00: **Bernhard Steinberger** et al.: *On the relation between plate tectonics, large-scale mantle flow and mantle plumes: Some recent results and many open questions* (keynote)
- 15:00 - 15:15: **Paul J. Tackley** et al.: *Influence of Melting on the Long-Term Thermo-Chemical Evolution of Earth's Deep Mantle*
- 15:15 - 15:30: **Maria V. Chertova** et al.: *3-D numerical modeling of subduction evolution of the western Mediterranean region*
- 15:30 - 15:45: Tobias Baumann, **Boris Kaus**, A. Popov: *Constraining the rheology of the lithosphere through geodynamic inverse modelling*
- 15:45 - 16:00: **Elisa Calignano** et al.: *Strain localization during compression of a laterally heterogeneous lithosphere*

16:00 - 18:00: Geodynamics Posters (chairs: F. Funiciello, S. Sobolev), Methods and Materials Posters (chairs: M. Frehner, M. Rosenau)

19:00 - 22:00 Joint conference dinner in Potsdam on the ship 'Belvedere' (Lange Brücke 6, 14467 Potsdam)

Wednesday 3 September 2014

09:00 - 11:00: Rheology Orals (chairs: G. Dresen, H. Sone)

- 09:00 - 09:30: **Yuri Fialko:** *Numerical models of ductile roots of mature strike-slip faults* (keynote)
- 09:30 - 10:00: **Laurent Montési:** *Localization processes on Earth, Mars, and Venus* (keynote)
- 10:00 - 10:20: **Suzon Jammes** et al.: *Localization of deformation in a polymineralic material*
- 10:20 - 10:40: **Sebastian P. Müller** et al.: *Rheology of bubble- and crystal-bearing magma: new analogue experimental data and an effective-medium model*
- 10:40 - 11:00: **Maria A. Nikolinakou** et al.: *Modeling stress evolution around a rising salt diapir*

11:00 - 13:00: Rheology Posters (chairs: G. Dresen, H. Sone)

13:00 - 14:00: Lunch break

14:00 - 16:00: Fluids and Deformations Orals (chairs: S. Miller, M. Moreno)

- 14:00 - 14:30: **Boris Galvan** et al.: *Towards a general simulation tool for complex fluid-rock lithospheric processes: merging pre-processing, processing and post-processing in state-of-the-art computational devices* (keynote)
- 14:30 - 15:00: **Takeshi Tsuji:** *Digital rock physics: Insight into fluid flow and elastic deformation of porous media* (keynote)
- 15:00 - 15:15: **Thomas Heinze** et al.: *Numerical Modelling of earthquake swarms in the Vogtland / West- Bohemia*
- 15:15 - 15:30: **Samuel Angiboust** et al.: *Effect of Fluid Circulation on Intermediate-Depths Subduction Dynamics: From Field Observations to Numerical Modelling*
- 15:30 - 15:45: Magdalena Scheck-Wenderoth, **Judith Sippel** et al.: *Heat transport mechanisms at different scales – a 3D modelling workflow*
- 15:45 - 16:00: **Antoine Jacquey** et al.: *Modelling of fractured reservoirs: Fluid-rock interactions within fault domains*

16:00 - 18:00: Fluids and deformations Posters (chairs: S. Miller, M. Moreno)

The posters will be presented during the entire conference. Each poster session starts with a 1-2 min. short presentation of all participating posters.

GeoMod2014 - Short course on "Constitutive Laws: from Observation to Implementation in Models"

Thursday 4 September 2014

Morning Session: Onno Oncken, Mathias Rosenau, and Fabio Corbi

- 09:00 - 10:00: **Onno Oncken:** Observing deformation kinematics and localization: Observations from the field, geophysical imaging, and geodetic monitoring
- 10:00 - 10:15: Coffee Break
- 10:15 - 11:00: **Mathias Rosenau:** Rheology of rock analogues 1: Elastoplasticity and its application in seismotectonic simulation
- 11:00 - 11:15: Coffee Break
- 11:15 - 12:00: **Fabio Corbi:** Rheology of rock analogues 2: Viscoelasticity and its application in seismotectonic simulation
- 12:00 - 13:00: **Visit to the GFZ Analogue Lab**

13:00 - 14:00: Lunch break

Afternoon Session: Georg Dresen and Erik Rybackii

- 14:00 - 15:15: Rheology of the lower crust : Reconciling laboratory data and field observations
- 15:15 - 15:30: Coffee Break
- 15:30 - 16:45: **Visit to the GFZ rock mechanics lab**
- 16:45 - 17:00: Coffee Break
- 17:00 - 18:00: Rock fracture processes and stick slip sliding –What do we learn from analyzing nanofemto seismicity?

Friday 5 September 2014

Morning Session: Stephan Sobolev and Sascha Brune

- 09:00 - 10:00: **Stephan Sobolev:** Rheology and geodynamic modeling: key controls in plate tectonics and beyond
- 10:00 - 10:15: Coffee Break
- 10:15 - 11:30: **Sascha Brune:** Rock rheology in numerical models: PC exercises and application to rift dynamics
- 11:30 - 11:45 Coffee Break
- 11:45 - 12:30: **Stephan Sobolev:** Rheology and cross-scale modeling: towards understanding of great earthquakes
- 12:30 - 13:00: Discussion

13:00 - 14:00: Lunch and end of the short course

GeoMod2014 – Hands-on tutorial on"ASPECT: a next-generation geodynamic modelling software" by Anne Glerum and Juliane Dannberg

Thursday 4 September 2014

08:30 - 9:00: Registration

- 09:00 - 10:00: **Tutorial 1:** First Steps – Compiling and Running ASPECT, **Lecture:** How to run and visualize simple models
- 10:00 - 11:15: **Lecture** ASPECT – A next-generation geodynamic modelling software, **Tutorial 2:** Convection in a 2D box
- 11:15 - 11:30: Coffee Break
- 11:30 - 13:00: **Tutorial 3:** Using the adaptive mesh refinement and spherical shell geometry **Lecture:** How to run and visualize simple models

13:00 - 14:00: Lunch break

- 14:00 - 15:15: **Tutorial 4:** Using the adaptive mesh refinement and spherical shell geometry and using the function parser
- 15:15 - 15:30: Coffee Break
- 15:30 - 17:00: **Tutorial 5:** Averaging at the example of subduction and using a “sticky air” layer
- 17:00 - 18:00: **Voluntary:** Installing ASPECT on personal computers

18:30: Joint Dinner (to be payed by the participants)

Friday 5 September 2014

09:00 - 18:00: ASPECT Strategy Workshop for Advanced Users: Perspectives for Modelling with ASPECT

Index

Abid, M., 101
Acocella, V., 177, 206, 231
Adamuszek, M., 352
Agard, P., 393
Ahmadzadeh, M. I., 3
Aller, A. L., 275
Almeida, J., 144
Alonso-Henar, J., 62
Alvarez-Gomez, J. A., 62
Alves da Silva, F. C., 67
Amirzada, Z., 424, 457
Angiboust, S., 393
Artemieva, I. M., 235
Averbuch, O., 112

Babeyko, A., 149
Badmus, B. S., 395, 396
Bagge, M., 7
Barantseva, O., 235
Barata, F., 144
Barrientos-García, B., 459
Basili, R., 9
Battaglia, M., 196
Baumann, T., 237
Bedford, J., 26
Blöcher, G., 407
Blanco, A., 67
Bonini, L., 9
Brandes, C., 71
Brandmeier, M, 188
Brizzi, S., 14
Broichhausen, H., 452
Brune, S., 239, 242
Buiter, S., 246, 334
Bull, A. L., 313
Bulois, C., 181
Burchardt, S., 181
Burov, E., 393
Burrato, P., 9
Burtin, A., 424

Cabral, F. R., 285
Cacace, M., 247, 407, 412
Cailleau, B., 211
Calignano, E., 249
Carmona, A., 75
Carvalho, B, 144
Cavozzi, C., 298
Cerca, C., 459
Cerca, M., 108
Chanceaux, L., 172
Chatton, M., 114
Chen, Z., 266
Chertova, M. V., 254
Cherubini, Y., 412
Clavera-Gispert, R., 75, 80
Cloetingh, S., 336, 387
Cnudde, V., 217
Contreras, J., 299
Cook, K., 84
Corbi, F., 14, 37, 177, 430
Corti, G., 108, 428
Cruden, A. R., 17, 266

Dabrowski, M., 294, 352, 355
Dalguer, L. A., 22, 52
Dannberg, J., 259, 320
Davaille, A., 261
Davies, T., 178
De Guidi, G., 226
Di Giuseppe, E., 430
Dominguez, S., 85, 114
Dotare, T., 434
Duarte, J. C., 144, 266
Dumazer, G., 439
Dumke, A., 211
Dutta, U., 269

Egglseder, M., 17

Eken, T., 424
Ellis, J. F., 452
Endo, I., 448

Faleide, J. I., 140, 281
Fialko, Y., 358
Flemings, P. B., 376
Fomin, I., 329
Fraters, M., 272
Frehner, M., 89, 95
Freymuth, H., 188
Fritzell, E. H., 275
Fuente, J. A. M. de la, 75
Funiciello, F., 14, 37, 430

Gärtner-Roer, I., 95
Gabrielsen, R. H., 140
Gaina, C., 313
Gallagher, M., 178
Galland, O., 181, 185, 439
Galvan, B., 397, 401, 404
Gao, X., 56
Garcia-Sancho, C., 363
Gassmoeller, R., 320
Geenen, T., 254
Gerya, T., 22, 37, 52, 121, 131, 285, 289, 336
Ghani, H., 101
Ghazian, R. K., 246
Gisler, G., 185
Glerum, A., 272, 331
Gloaguen, R., 149
Gomes, C. J. S., 448
Gomez, C., 178
Gover, R., 363
Gracia-Marroquín, D., 108
Gratacos, O., 75, 80
Graveleau, F., 84, 112, 114
Großmann, J., 452
Guéguen, Y., 159
Gueydan, F., 368
Guillou-Frottier, L., 289
Görz, I., 443

Hallot, E., 181
Hamidi, S., 397, 401, 404
Hampel, A., 7, 347
Hardy, S., 75
Hartz, E. H., 136
Haug, Ø. T., 185, 424, 457
Hayman, N. W., 324
Heine, C., 239
Heinze, T., 397, 401, 404
Heistek, R, 188
Herceg, M., 235
Herrendörfer, R., 22
Herwegh, M., 381
Hillebrand, B., 331
Hinsbergen, D. J. J. van den, 254
Holohan, E. P., 191, 211, 217, 439
Hori, T., 434
Hovius, N., 84
Hudec, M. R., 376
Huismans, R. S., 116
Hussain, H., 101

Iandelli, I., 428
Imposa, S., 226

Jacquey, A., 407
Jammes, S., 365
Jansen, G., 397
Javed, E., 101
Johansen, E., 117
Jolivet, L., 289

Kaban, M. K., 304, 387
Kagan, A. I., 49
Kaiser, B. O., 412
Karatun, L., 276
Karrech, A., 381
Kastelic, V., 9
Kaus, B., 237, 308
Keir, D., 206
Kelly, B. F. J., 153
Kennedy, B., 178
Kervyn, M., 217
Khan, I., 101
Khatami, M., 397
Klemann, V., 278
Klitzke, P., 281
Kullberg, C., 144

La Marra, D., 196, 231
Lavier, L. L., 324, 365
Leever, K., 117, 310, 457
Lennox, P., 153

Leroy, Y. M, 159
Lewerenz, B., 412
Li, H., 201
Li, S., 26
Liao, J., 121
Ling, A. H. M., 95
Llewellin, E. W., 372
Lopez-Blanco, M., 80
Lourenço, D. L., 284, 329

Maccaferri, F., 177, 206
Mader, H. M., 372
Mai, P. M., 52
Maillot, B., 29, 159
Malavieille, J., 114
Malik, A., 101
Mandal, N., 269
Manighetti, I., 114
Mannu, U., 131
Mares, C., 459
Marques, F. O., 285
Martinec, Z., 278
Martinez-Diaz, J. J., 62
Massmeyer, A., 430
Matenco, L., 336
May, D. A., 285
Maystrenko, Y. P., 412
Medvedev, S., 136
Melnick, D., 26
Menand, T., 172
Menant, A., 289
Miller, S., 397, 401, 404
Miraj, M. A. F., 140
Montesi, L. G. J., 368
Mooney, W. D., 387
Moreno, M., 26
Moroni, M., 14
Mourgues, R., 181
Mueller, S. P., 372
Mukherjee, S., 43
Muldashev, I. A., 33
Mulyukova, E., 294, 320
Musiol, S., 211

Nadimi, A., 318
Nakawaga, T., 329
Naliboff, J., 334
Nestola, Y., 298
Neumann, F., 299
Niño, Y., 221
Nikolinakou, M. A., 376
Noack, V., 412

Offler, R., 153
Oncken, O., 26, 39, 310, 457
Ouzgaït, M., 112

Pérez-gussinyé, M., 239
Palano, M., 226
Parang, S., 300
Pascal, C., 140
Pauwels, E., 217
Pearson, D. G., 342
Pedersen, R, 214
Pellerin, J., 443
Peters, M., 381
Petit, C., 114
Petrunin, A. G., 304
Pinel, V., 177
Popov, A., 237, 308
Poppe, S., 217
Portillo-Pineda, R., 108
Poulet, T., 381
Pranger, C., 36, 37
Pusok, A. E., 308
Pysklywec, R., 276

Quinion, A., 112
Quinteros, J., 340

Rahimi, H., 3
Reber, J. E., 365
Regenauer-Lieb, K., 381
Ritter, M. C., 310
Rivalta, E., 177, 206, 231
Roche, O., 221
Rodrigues, B. A., 448
Rosas, F. M., 144
Rosenau, M., 26, 39, 310, 424, 457
Ruch, J., 231

Sakaguchi, H., 434
Santimano, T., 39
Santimano, T. N., 430
Sarkar, S., 269

Sarocchi, D., 459
Sasgen, I., 278
Schöpfer, M. P. J., 191
Scheck-Wenderoth, M., 247, 281, 407, 412
Schellart, W. P., 266
Schmalholz, S., 331, 464
Schmeling, H., 304
Schmid, D. W., 352
Schreurs, G., 62, 164
Schroeder, S., 149
Scudero, S., 226
Sedano, L. A. R., 459
Seno, S., 9
Shephard, G. E., 275, 313
Singh, P., 43
Sippel, J., 281, 412
Sobolev, S. V., 33, 149, 239, 259, 294, 320, 340
Sobouti, F., 3
Sohrabi, A., 318
Sokoutis, D., 249
Sone, H., 385
Spakman, W., 36, 254, 272, 331, 334
Steinberger, B., 294, 304, 320
Sternai, P., 289
Storti, F., 298
Strak, V., 114
Strasser, M., 131
Sudhaus, H., 191
Suppe, J., 84
Suzuki, N., 46
Svartman Dias, A. E., 324

Tackley, P. J., 284, 329
Tatarinov, V. N., 49
Tatarinova, T. A., 49
Terrinha, .P, 144
Tesauro, M., 278, 363, 387
Tetreault, J., 246
Thieulot, C., 36, 272, 276, 331, 334
Thybo, H., 235
Tolosana-Delgado, R., 80
Tolson, G., 299
Tomás, R., 144
Torsvik, T., 331
Toscani, G., 9
Trippanera, D., 231
Truby, J. M., 372
Träger, F., 443
Tsuji, T., 417
Turowski, J., 84
Tutu, A. O., 332
Tympel, J., 149

Ueda, K., 131

Valensise, G., 9
van den Berg, A., 36
van den Berg, A. P., 254
van Dinther, Y., 22, 37, 52
van Gasselt, S., 211
van Hunen, J., 342
van Zelst, I., 334
Vazquez, A., 299
Vendeville, B., 112
Veveakis, M., 381
Vogt, K., 336
von Tscharner, M., 464

Wörner, G., 188
Walsh, J. J., 191
Walter, M., 340
Walter, T. R., 191, 211
Wang, H., 342
Wang, K., 56
Warners-Ruckstuhl, K. N., 363
Watanabe, K., 201
Willett, S. D., 131
Williams, D. A., 211
Willingshofer, E., 249
Winsemann, J., 71
Wolff, S., 393

Yamada, Y., 434
Yamato, P., 393
Yan, J., 153
Yassaghi, A., 467
Yonezu, K., 201
Yuan, X., 159

Zafar, M., 101
Zehner, B., 443
Zeoli, A., 428
Zeumann, S., 347
Zhu, G., 285
Zwaan, F., 164